**Optimal Model Reduction of Lithium-Ion Battery
Systems Using Particle Swarm Optimization**

by

Isaiah Oyewole

**A thesis submitted in partial fulfillment
of the requirements for the degree of
Master of Science in Engineering
(Energy Systems Engineering)
in the University of Michigan-Dearborn
2019**

Master's Thesis Committee:

    **Assistant Professor Youngki Kim, Chair
Assistant Professor Stanley Baek
Assistant Research Scientist Kyoung Hyun Kwak**

Dedication

This thesis work is dedicated to Almighty God, the creator of the heavens and the earth. This work is also dedicated to my family, who have always been there for me. The love and support you guys have always shown me is a motivation for me. Also, this work is dedicated to my academic mentor and father, Assistant Professor Youngki Kim, who have been a teacher, and a pillar of support to me throughout my degree program at the University of Michigan-Dearborn.

Acknowledgements

I would first like to give praises and thanks to Almighty God, who has giving me the wisdom, strength and sound health to undertake this thesis work and enabled me to its completion. It is with him I can do all things, and without him I can do nothing.

I would like to appreciate my thesis advisor, Assistant Professor Youngki Kim, of the College of Engineering and Computer Science at the University of Michigan-Dearborn for the enormous effort he invested in me while working on this thesis under his advisement. He is more than a thesis advisor to me, but an academic mentor whose display of support and faith in me, ever since the first day I walked into his office to discuss the possibility of doing an independent study under his advisement has being outstanding. While working on this thesis, every now and then I used to knock on his door for clarification on some doubts and he was always there to help and provide guidance for me. I have learnt a lot from him as a researcher and a teacher. He was always there for me doing my learning stage, in the field of Lithium-ion battery systems. Thank you for having faith in me and giving me all those opportunities for my personal and professional development.

I would also like to thank Assistant Professor Stanley Baek, and Assistant Research Scientist Kyoung Hyun Kwak for taking from their precious time to go through this thesis work and for being part of the thesis defense committee.

My appreciation also goes to my parent (Pa. and Mrs. J.A. Oyewole) and my siblings, for their prayers and support among other things they have shown me, these have been my strength and

Table of Contents

List of Figures

List of Tables

Abstract

The efficiency of energy storage systems is pivotal to the sustainability of energy production technologies in ensuring global energy security. Lithium-ion batteries (LIBs) have been widely used as an energy storage mechanism among all the types of rechargeable batteries owing to their high energy and power density. Because of the vast applications of LIBs in several dynamic operations which differs in energy and power requirements, the development of a robust model to simulate the battery's dynamic behavior and performance for control and system design is paramount.

Several modeling efforts have been invested into the development of electrochemical models for simulation of LIB systems ranging from a full-order model, the so-called Doyle-Fuller-Newman (DFN) model to several reduced-order models. Most of these reduced-order models are based on a single particle model with or without the inclusion of electrolyte dynamics. This thesis work involves the development of a reduced-order electrochemical model based on single particle approach with electrolyte dynamics (SPMe). The partial differential equations (PDEs) that capture the dynamic behavior and performance characteristics of the LIB systems were solved numerically through a finite difference method in MATLAB environment. For model reduction purpose, a constrained optimization problem was formulated to determine the optimal uneven discretization node points needed to numerically solve the battery PDEs for both solid and electrolyte phase concentration predictions. The optimization problem was solved using a particle swarm optimization (PSO) by minimizing the errors between the reference model, a SPMe with even discretization using a fine step size and the reduced model, a SPMe with uneven discretization.

The proposed approach is similar to that in [22], but different because of the inclusion of electrolyte dynamics. The battery voltage was computed based on the optimal uneven discretization nodes under three different charging/discharging conditions. The proposed model demonstrates that as the number of optimal uneven discretization nodes applied to the model increases, the fidelity of the model increase. However, no significant improvement of prediction accuracy is observed after a certain level of uneven discretization. The proposed model demonstrates that in comparison to the evenly discretized model, the complexity in terms of the number of states can be reduced by 7 times without loss of physical interpretation of the diffusion and migration dynamics in the solid particles and electrolyte across the entire cell. This reduction in the number of discretization allows for faster computation for the purpose of control and system design.

Chapter 1: Introduction

Energy investment, according to International Energy Agency (IEA), is the exploration, production, distribution, transportation and storage of all forms of energy. Energy storage is as important as energy production in ensuring global energy security. Improvement of energy exploitation and production technologies without corresponding improvement in energy storage technologies will leads to poor energy management. Since energy productions are mostly at the excess of what is needed momentarily, this demonstrate the importance of energy storage systems. Energy storage system is a depository medium for energy which is not needed at the time of production to serve future purposes, this involves converting energy from the source forms to forms more amenable to storage. There are several energy storage mechanisms, the most common and portable one being the electric battery. Battery stores chemical energy and delivers electrical energy to electrical appliances under usage. It produces direct current by converting chemical energy into electrical energy through certain electrochemical reactions.

1.1 Electrochemical Battery

The first electrochemical battery was built in 1800 by Alessandro Volta [1], this battery consists of copper and zinc plates, separated by a salt bridge called brine-soaked paper disks, to ensure electroneutrality of the system.
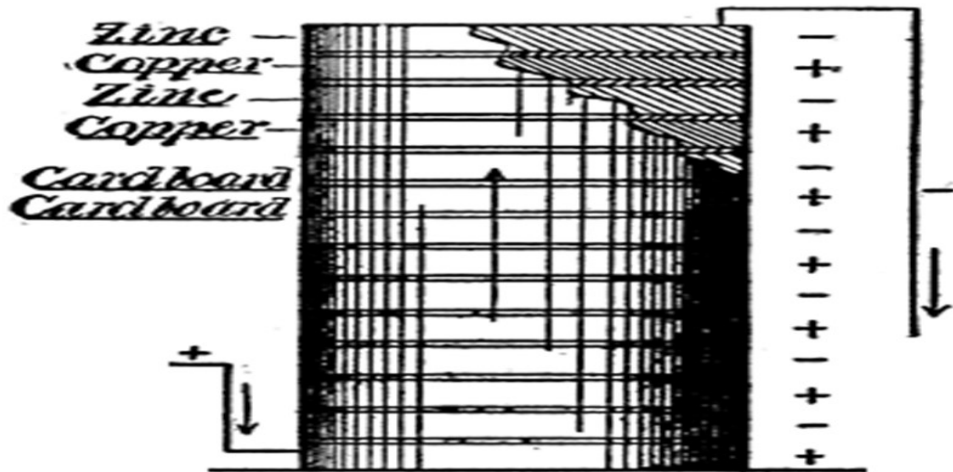
Figure 1: Voltaic cell [2]

Breathtaking developments in battery technology has occurred from the first electrochemical battery built to the latest battery technology available now, ranging from the battery size, material composition and the price. Fundamentally, a battery comprises of a positive electrode (cathode), a negative electrode (anode), a separator, and a flux of electrolyte as shown in Figure 2.
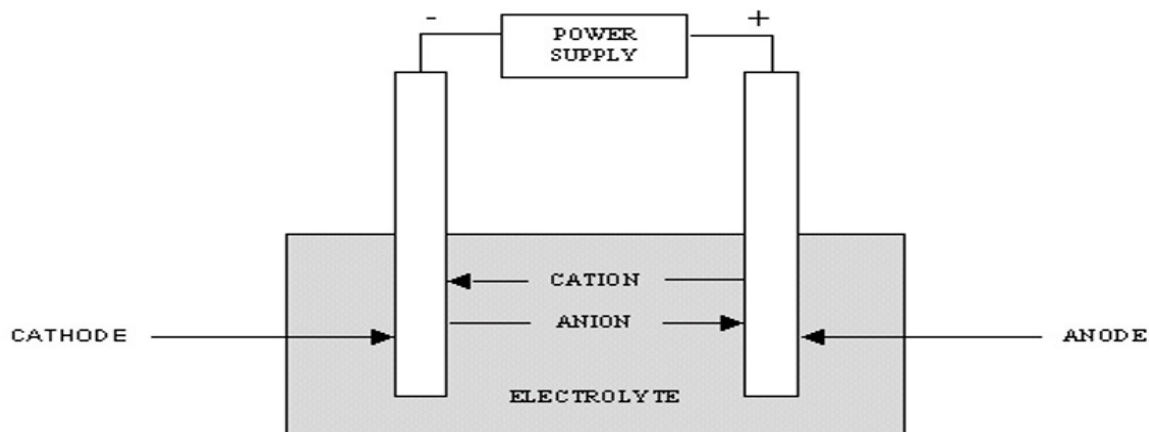
Figure 2: Typical Electrochemical Battery

The electrochemical battery can either be a rechargeable or non-rechargeable battery. The non-rechargeable (primary) batteries undergo an irreversible chemical reaction, which makes them non-reusable once the stored chemical energy has been depleted. On the other hand, the

rechargeable (secondary) batteries undergo a reversible chemical reaction making them re-usable upon initial total depletion (discharge) of their stored energy. The advantage of non-rechargeable batteries over rechargeable batteries, lies in their high energy density and high initial voltage, but they are only useful for application with low power demand and requires continuous replacement for operation once the stored energy is depleted. On the contrary, rechargeable batteries, are more economical, eco-friendly and help improve appliances performance. Therefore, they are widely used in several high-power demanding operations, due to their tendency to be quickly recharged. There are several types of rechargeable batteries and these include,

- Lead-Acid Battery

- Nickle Cadmium Battery

- Nickel-Metal Hydride Battery

- Lithium-Ion Battery (LIB)

1.1.1 Lead-Acid Battery

The first practical lead acid battery was developed by Raymond Plante in 1860 [3]. Lead-acid (Pb-acid) batteries are manufactured in a variety of sizes and designs, from less than 1 to over 10,000 Ah battery capacity. The average operating range of a Pb-acid battery is about 2.0 V [3]. In this form of rechargeable battery, lead oxide (PbO_2) is used as the active material for the positive electrode, metallic lead (Pb) as the active material for negative electrode, while the electrolyte is made of sulphuric acid (H_2SO_4) as shown in Figure 2.
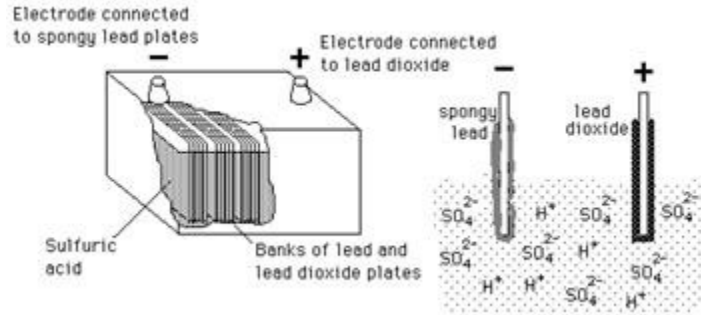
Figure 3: Schematic Diagram of Lead-Acid Battery [4]

The main challenge confronting the usage of lead-acid batteries compared to other types of batteries is their limited energy density and relatively low life-cycle.

1.1.2 Nickel Cadmium Battery

Nickel cadmium battery was invented by Waldemar Jungner in 1899. The positive electrode of a nickel cadmium battery consists of nickel hydroxide (NiOOH) as the active material, cadmium as the negative active materials and potassium hydroxide as the electrolyte. This battery in comparison with other types of rechargeable batteries can deliver their rated energy and power capacity even at high discharge rate, with an optimal life-cycle and capable of operating in extreme temperatures. The main challenge with this battery is their high self-discharge rate, the environmental concern posed by cadmium disposal, and the high cost of production.
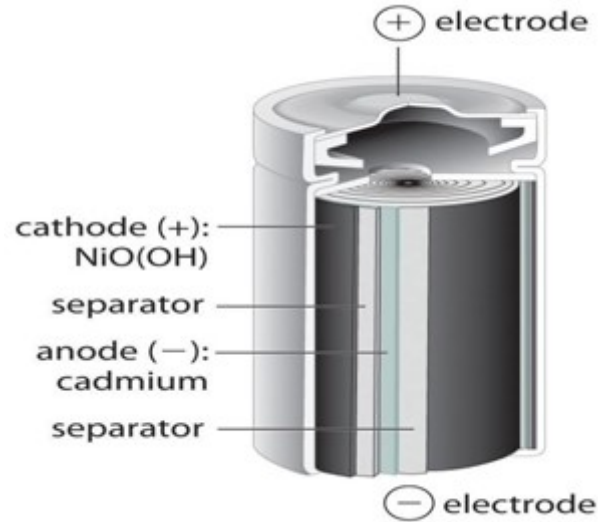
Figure 4: Schematic Diagram of Nickel-Cadmium Battery [4]

1.1.3 Nickel-Metal Hydride Battery

Nickel-Metal Hydride (Nickel-MH) battery is an extension of nickel-cadmium battery. The main difference between them is their respective negative electrode's active material. During the charging process, the Nickel-MH battery has metal hydride (MH) as the active material for the negative electrode, which undergoes a reduction process into a metal alloy. The positive electrode has nickel oxide hydroxide (NiOOH) as the active material and it is reduced to nickel hydroxide ($Ni(OH)_2$). The electrolyte contains a higher percentage of potassium hydroxide (KOH) and it has a 'starved electrolyte' designed to enhance the diffusion of oxygen in the negative electrode at the end of the charging cycle.
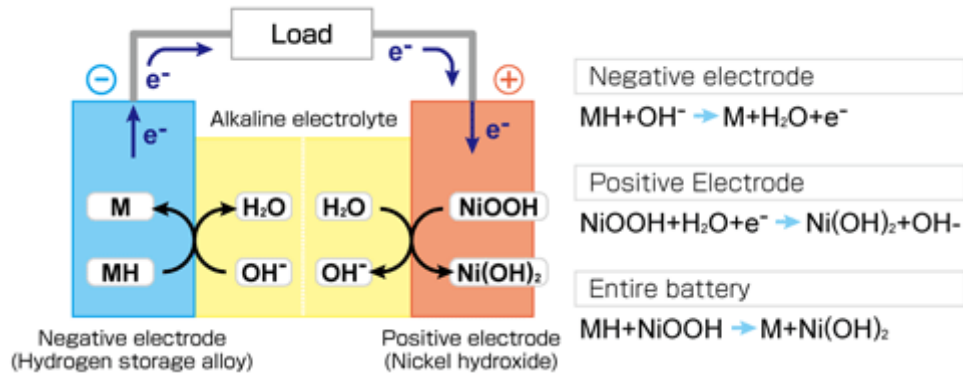
Figure 5: Schematic Diagram of Nickel-Metal Hydride Battery [5]

Although Nickel-MH battery has better energy and power density compared to Nickel Cadmium battery, but its low energy and power density in comparison to lithium-ion battery (LIB) gives the later higher preference. Nickel-MH battery suffers from memory effect and its average operating voltage is around 1.35 V [6].

1.1.4 Lithium-Ion Battery

Lithium-ion batteries (LIB) are the most widely used energy storage mechanism of all types of rechargeable batteries due to their high energy and power density, coupled with no memory effect capability and their high average operating cell voltage.
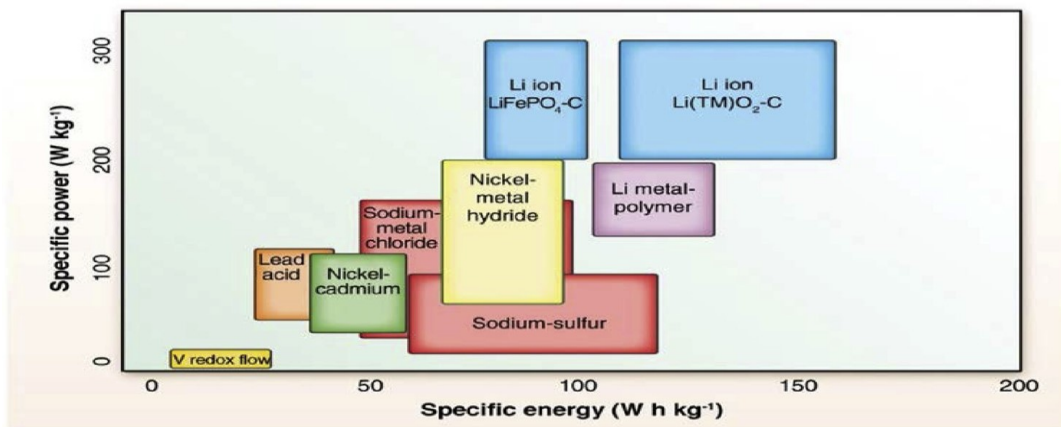
Figure 6: Comparison of different batteries specific power and specific energy [33]

Lithium-ion battery consists of a negative electrode (anode) made of carbon, a positive electrode (cathode) composed of metal oxide such as $LiCoO_2$, $LiMn_2O_4$, $LiFePO_4$ and a lithium salt electrolyte. LIB being a porous electrode battery, enables the lithium salt electrolyte to diffuse and migrate from one electrode through the separator, to the other electrode while transporting lithium ion during this mass transport. The separator region consists of lithium-salt electrolyte, which is held basically in an organic solvent such as $LiPF_6$, $LiBF_4$ or $LiClO_4$ or in some solid polymer composite [7].

Lithium-ion batteries technology have gained astounding advancement over the last two decades. Its importance has grown in the past and demands keep increasing on an exponential rate because of their applications in electric vehicles (EVs), plug-in hybrid electric vehicles (PHEVs), hybrid electric vehicles (HEV), portable electronic devices and in most renewable energy generation stations. In the automotive industry, due to the high instantaneous electric power demand of electric propulsion systems, a reliable energy source like the lithium-ion battery is needed. As lithium-ion battery can be applied in several areas differing in power and energy requirements, modeling of this battery dynamics is expedient to enable accurate prediction of the battery performance and life-cycle.

1.2 LIB Operational Principle

Lithium ion cell consist of a negative electrode (anode during discharging), the separator which contains lithium-salt electrolyte solution and a positive electrode (cathode during discharging) as shown in Figure 7. The two electrodes are made of porous active materials. During discharging operation at the negative electrode, lithium ion de-intercalate from graphite solid particles (Li_xC_6) at the solid-electrolyte interface (SEI) into the lithium-salt electrolyte, that is held either in the

solvent or polymer. An ionic Li-ion (Li^+) is formed which travels across the separator (which separates the anode and cathode spatially and electrically) to the positive electrode, where the ionic lithium ion (Li^+) intercalates into metal oxide particles (Lithium Cobalt Oxide, $LiCoO_2$).
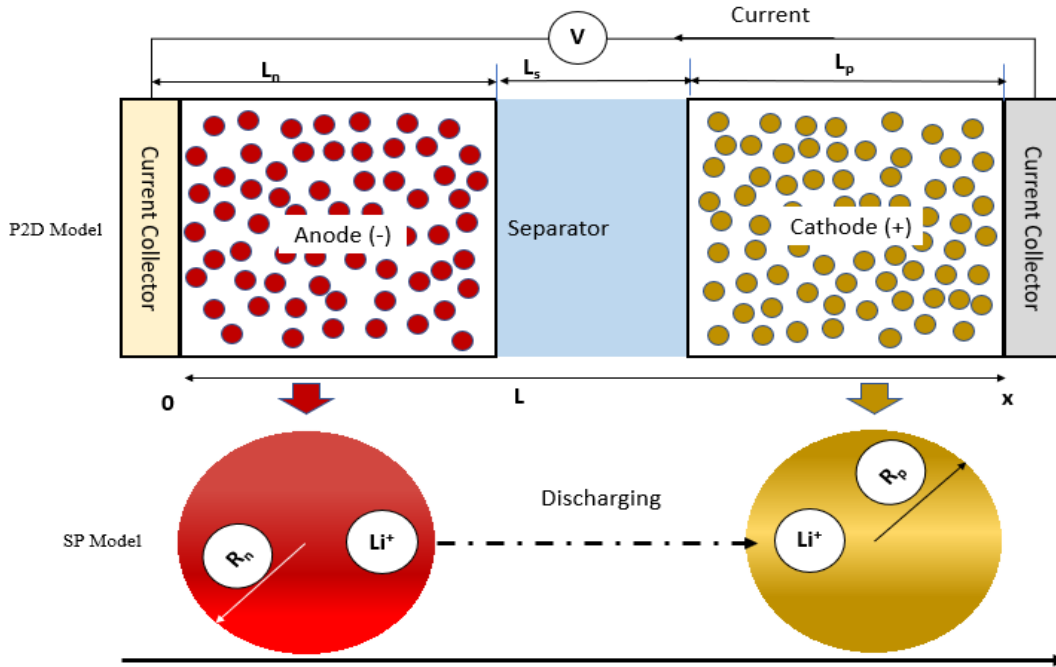
Figure 7: Schematic representation of lithium-ion battery during discharging

The driving force for the electrochemical reaction at the SEI is the transfer current density (J_{Li}). As ionic lithium ion diffuses into the electrolyte salt solution, since the separator is impermeable to electrons, the electrons from the chemical reaction are transferred to the current collectors and then onwards transferred as an electronic current through an externally connected load to the positive electrode. Hence, an electric current flow in the opposite direction to the electrons flow. The reverse reaction occurs during the charging operation. The mathematical representation of the chemical reaction taking place at the SEI layer in both electrodes are as below. It should be noted that the forward reaction represents the discharging operation and backward reaction is the charging operation:

Negative Electrode:

$$Li_x C_6 \rightleftharpoons 6C + xLi^+ + xe^-$$

Positive Electrode:

$$Li_{y-x}CoO_2 + xLi^+ + xe^- \rightleftharpoons Li_y CoO_2$$

Overall Reaction:

$$Li_{y-x}CoO_2 + Li_x C_6 \rightleftharpoons Li_y CoO_2 + 6C$$
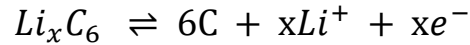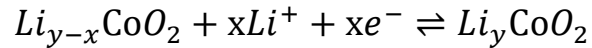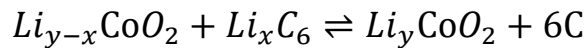
The chemical reactions are modeled with mathematical expressions, employed to represent the working principles and behaviors of the battery during both the charging and discharging operations. The fidelity of the battery models is paramount for accurate prediction and investigation of the battery dynamic performance.

1.3 Battery Modeling Approach

The importance of battery modeling cannot be overstated during the design and run time stage of Li-ion battery systems. Accurate LIBs modeling is strategic for a better battery packs design and for embedded Battery Management Systems. During the design stage, modeling helps battery technology specialists in the development of a better and more reliable battery systems with minimal production costs. Likewise, during the run time stage of LIB systems, modeling helps in the investigation and study of important information, about the battery's parameters of interest under any given operating condition. LIB modeling approach varies widely in terms of their complexity, and computational requirements. The models are evaluated according to their accuracy, complexity and physical interpretability.

The two major modeling approaches are:

- Equivalent Circuit Model (ECM)

- Physic-based model (Electrochemical Model)

1.3.1 Equivalent Circuit Model

The equivalent circuit model (ECM) simply models the battery as a simple electrical circuit, comprising of a voltage source in series connection with resistors and capacitors, coupled with a component to model the output voltage from the battery. Diffusion processes inside both electrodes are modeled by using capacitors and resistors.

ECMs are mostly preferred than other models, because of their simplicity and low computational requirements but they have low prediction fidelity compare to electrochemical models.

1.3.2 Electrochemical Model

Electrochemical models (EMs) are developed based on the physical laws governing the operation of the battery. The battery models based on electrochemical laws [8,9] are generally preferred to the equivalent circuit, or to other kinds of simplified models especially for automotive applications. This is because they capture all the dynamic operations taking place in the battery and predict the physical cells' limitations, which are relevant in automotive application where the battery suffers charge stress of very high transient loads [10]. The magnitude of the instantaneous battery power available for usage depends on the electrochemical diffusion dynamic, the battery state of charge (SoC) and as well as the applied current [11]. Most of these important battery parameters can only be determined through an electrochemical model.

The electrochemical models involve diffusion, intercalation and electrochemical kinetics in the formulation of the mathematical model consequently, providing insight into the internal state of

the battery, by capturing all the dynamic operations. These contribute to the complexity of the model. Micro-macroscopic electrochemical modeling relates to the hybrid electric vehicle design, scale-up, optimization, and control issues of HEV where the battery plays an important role in this area, as a high-rate transient power source [7].

However, because of the high complexity and computational requirements of the electrochemical model, most automotive applications of lithium-ion battery models prefer the equivalent circuit model, because of their fast computation capability and simplicity of their control design [12-15]. Although diffusion dynamics are not observable in the equivalent circuit models and this results in their low fidelity. Also, ECM has limited prediction capability, as it does not consider the fundamental electrochemical phenomena behind the battery's operation. Consequently, continuous effort is being made toward reduction of electrochemical model complexity, to ensure high fidelity and fast computation for real-time online estimation technique which is the motivation for this work.

1.4   Literature Review

An equivalent circuit model (ECM) was developed by Shamsi *et al*. [49] in their work, in which their proposed model was designed based on an inclusion of dynamic characteristics for the battery systems, which include non-linear open circuit voltage, discharge current, and capacity. Their model was developed in MATLAB environment such that it is applicable to all lithium-ion chemistries and their model has a cooling system. The components of their ECM are a voltage source representing, the open circuit voltage of the battery, one internal resistance, two parallel circuits with one resistor and capacitor each. They conducted parameter estimations of the circuit through a pulse discharge test (PDT), by varying the pulse current levels to investigate its effect on the battery parameters. Likewise, a continuous discharge test (CDT) was carried out by

continuously discharging the battery to investigate its effect on the battery capacity. Their proposed model was simulation results agree well with the experimental results especially at low C-rate.

Electrochemical modeling of lithium-ion batteries includes a range of models from the full-order model developed by Doyle *et al.* [8] to several reduced-order models which are the simplified forms of the full-order model developed to reduce the electrochemical model complexity and computational requirements. The Doyle-Fuller-Newman (DFN) model is a popular electrochemical-based lithium-ion battery model, expressing solid-phase and electrolyte-phase lithium-ion diffusion dynamics. It accurately predicts the cell performance (cell current/voltage), using the battery governing nonlinear partial differential equations (PDEs). Doyle *et al.* developed a galvanostatic charge and discharge of a lithium anode/solid polymer separator/insertion cathode cell model in 1993 [8] using the porous electrode theory. The developed model in their studies was generalized for a wide range of applications with different polymeric separator materials, lithium salts, and composite insertion cathodes. Simplification of numerical calculations for the cathode was implemented using the superposition principle. The battery governing PDEs were solved simultaneously using the subroutine BAND, while the time derivative parameters were evaluated using the Crank-Nicolson method. The designed model includes variable physical properties, and at the end, their presented results showed the charge and discharge behavior of the lithium/polymer/insertion cell.

DFN model captures the battery performance dynamics with high fidelity, however, the implementation of this complex model involves a significantly high computation cost [16]. Another form of full-order model was developed referred to as Pseudo-2D (P2D) models. The P2D

model was developed based on porous electrode theory. This model describes lithium ion transport across the cell thickness, through a one-dimensional charge and mass conservation laws along the cell thickness (macroscopic level), and lithium-ion mass transfer across the radial direction of each active particle (microscopic level). The kinetic reaction at the solid-electrolyte interface is described by Butler-Volmer equation. The P2D model comprises of ten coupled nonlinear partial differential equations (PDEs), expressing mass and charge balance in both solid and electrolyte phases [27, 28].

Although P2D is a high-fidelity model for capturing the dynamics behavior of LIBs, the complexity and high computational cost of solving the ten coupled nonlinear PDEs is its major challenge. The challenges posed by the full-order model necessitated the development of the reduced order model. The reduced order models are developed based on several approximations and assumptions to simplify the full-order model, ensuring its applicability for the real-time online estimation techniques. Several research efforts had been directed to the development of the reduced order models. This includes assuming a uniform lithium-ion concentration at the macroscopic level (electrolyte-phase) and considering only the microscopic level (solid phase) lithium-ion concentration dynamics in the so-called Single Particle (SP) Model. The basic assumptions of SP model are that both electrodes are composed of spherical particles of the same shape, with a uniform current distribution over the single spherical particle. This simplified model strikes the needed balance between the electrochemical model (EM) and equivalent circuit model (ECM) by its simplification of the full order electrochemical model. This consequently reduces the computational cost of electrochemical models, while maintaining to a certain degree its fidelity the prime advantage of ECM over EM. The SP model comprises of a set of PDEs derived directly from the full-order electrochemical models, maintaining most of the battery characteristics

13

explicitly [10] and can describe the internal electrochemical states of the battery. However, this model become inadequate to capture accurately the battery dynamics at high current rates, due to the assumption of uniform electrolyte concentration and potential distribution across the cell length.

Significant developments in SP model includes several model reduction approaches. Smith *et al.* [21] presented a generalized method, to numerically generate a fully observable/controllable 1D electrochemical model of a lithium ion battery. Their model was derived from the electrochemical kinetics, conservation of species and conservation of charge governing PDEs in the solid and liquid phases of the battery. Model order reduction method was applied to reduce the computational complexity of their model, by breaking the complex model into electrode sub model, electrolyte sub model and current/voltage sub model. The solid electrodes were modeled based on porous electrode theory as introduced by Doyle *et al.* [8], and electrode-averaging technique was applied to approximate the electrode surface concentration/reaction distribution coupling. The one-dimensional domain was discretized into approximately 70 control volumes and each of the four governing PDEs were simultaneously solved in the x-direction. Their reduced order model was validated against a higher order nonlinear CFD model of a 6 Ah HEV cell, with a constant current profile varying up to 50C-rate between the discharge, charge, and rest cycles as shown in Figure 8.
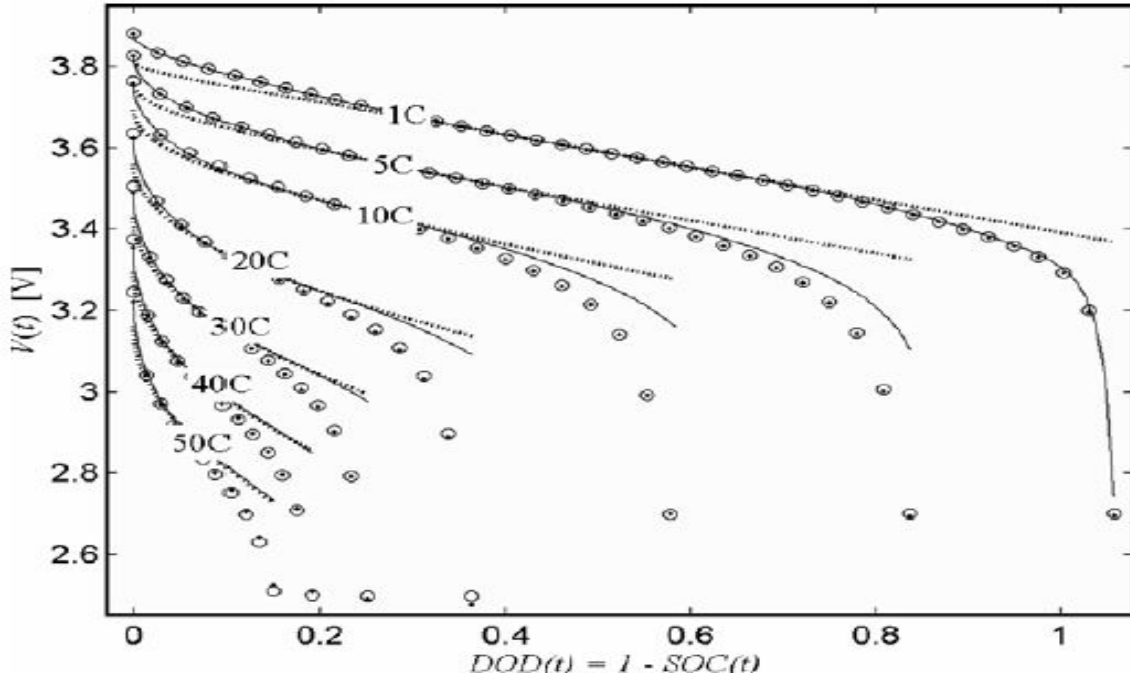
Figure 8: Voltage responses of various state variable models versus CFD model for constant current discharge for 1C- 50C rates initiated from 100% SOC [21].

Domenico *et al.* [7], developed an electrode-averaged model similar to the single particle assumptions. The solid concentration dynamics at the macroscopic level were neglected for simplification purpose in their model. Their assumption results to an average value for the solid concentration that can be related with the battery state of charge and critical surface concentration [21]. The battery PDEs capturing the battery electrochemical kinetics, conservation of species and charge, were solved numerically using a finite difference method in MATLAB. They presented a low order extended Kalman filter for the estimation of the average-electrode state of charge. Their model was validated against the simplified model results as in [22] shown in Figure 9. The assumptions behinds their simplified electrode-average model does not hold under high current charging/discharging operations which makes their simplified model inappropriate for high C-rate operation predictions.
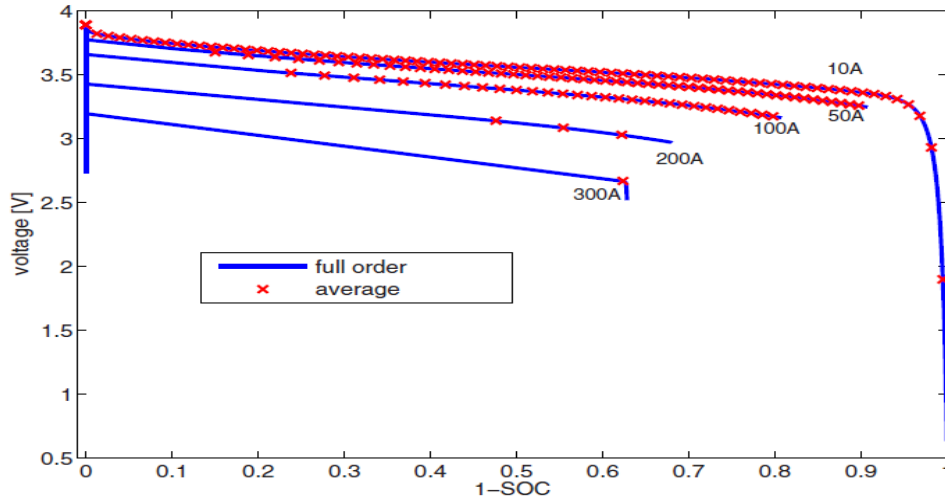
Figure 9: Voltage response of average versus full order model for different constant current from 10 A to 300 A [7]

Lee and Filipi [22] proposed a reduced order model which is based on the electrode-averaged model developed in Domenico *et al.* [7]. They developed a reduced order model, and solved the resulting ODEs numerically using a finite difference method. The FDM numerical solutions involves evenly discretized nodes and unevenly discretized nodes. The evenly discretized FDM model was used as a reference model to develop the reduced order model with uneven discretization. The reduced model allows for fast computation and accurate prediction of the lithium intercalation dynamics. An optimization problem was formulated based on the predictions error between the reference model and the reduced mode. The constructed constrained nonlinear optimization problem was solved with sequential quadratic programming (SQP). Based on their optimization solution analysis, the accuracy of the unevenly discretized model for voltage prediction increases as the number of unevenly discretized nodes increases as shown in Figure 10. Although their proposed reduced order model with unevenly discretized FDM approach proves efficient in reducing the required computational efforts while maintaining the prediction accuracy

16

and depth of the physical interpretations. The assumption of uniform electrolyte concentration might not hold at discharging/charging c-rates and this will impact the model prediction accuracy. The impact of electrolyte dynamics inclusion to their proposed model for LIBs behavior prediction is the main motivation for this work. The influence of the electrolyte dynamics inclusion in the reduced order model is demonstrated in Figure 11. The assumption of a uniform electrolyte concentration distribution is shown by the red line while the blue line profile shows the actual behavior of the electrolyte dynamics during a 2C-rate discharging operation. This demonstrate why the fidelity of SP model reduces at high C-rate due to the uniform concentration assumption.
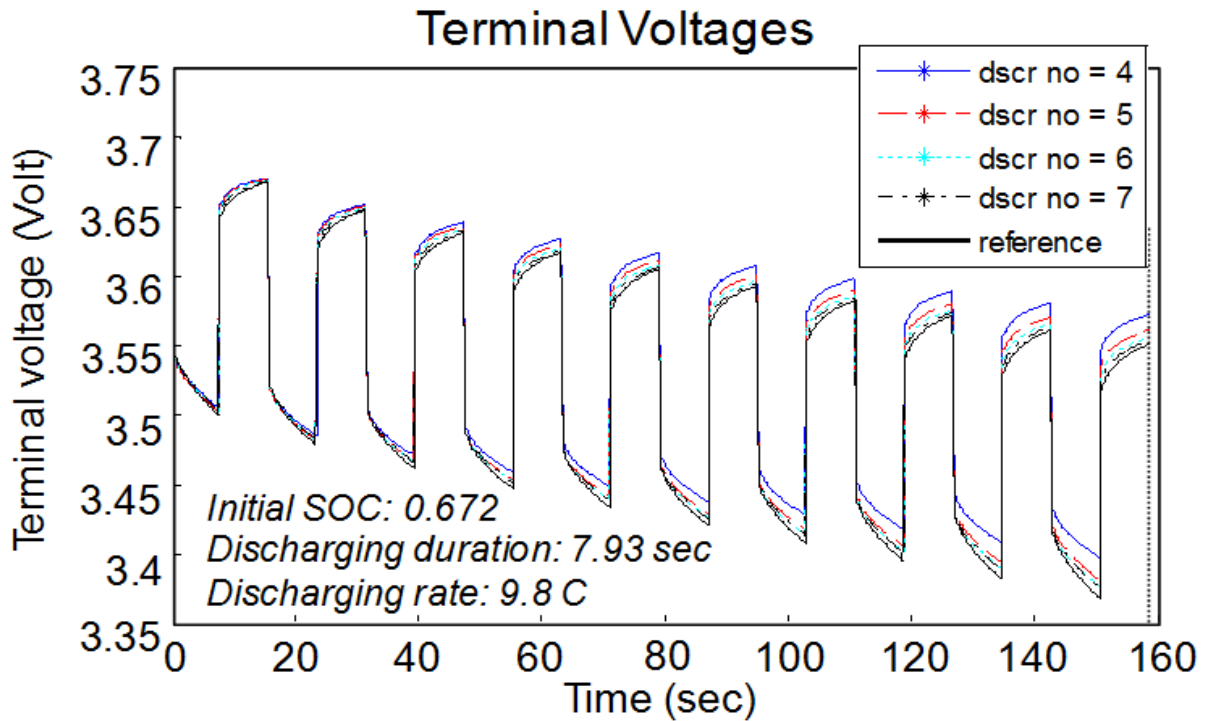
Figure 10: Comparison of the terminal voltage profiles depending on the number of uneven discretization steps [22]
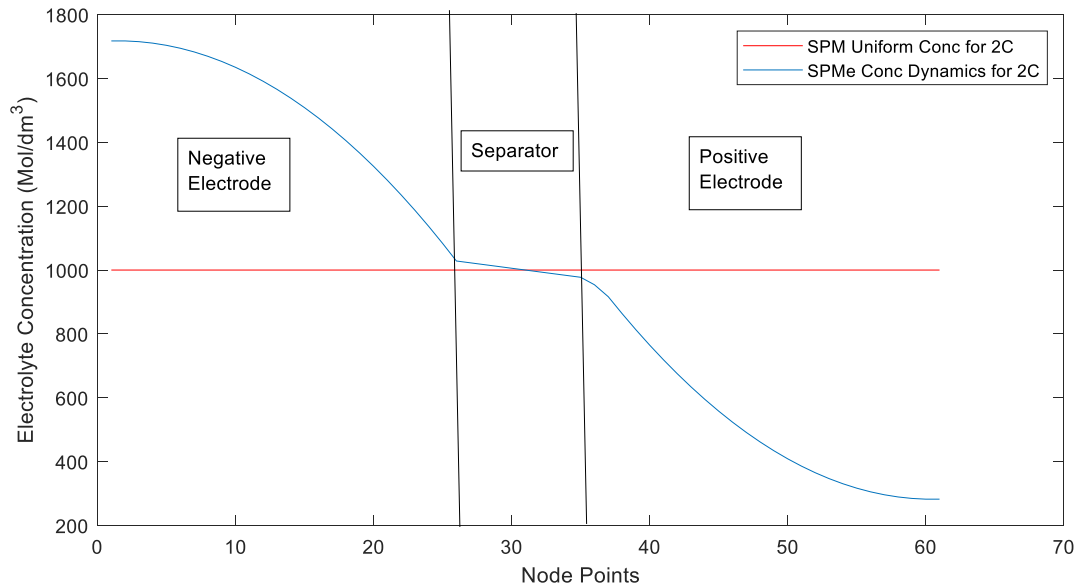
Figure 11: Electrolyte-phase concentration distribution with/without electrolyte

Furthermore, several efforts have been made to resolve the main drawback of SP model, researchers in the past have proposed different techniques to couple electrolyte dynamics with the conventional SP model. Single particle model with electrolyte dynamics (SPMe) describes accurately the internal electrochemical states of the battery. The SPMe model allows for better model-based control design with less complexity and computational cost as compare to full-order model [17-18, 31-33]. Different simplification approaches have been developed for inclusion of electrolyte dynamics to the SP model. The methodology employed in solving the battery PDEs differs for most reduced order models.

The battery PDEs can be solve analytically and numerically. Several analytical approaches have been used in previous studies to simplify the PDEs into more solvable ordinary differential equations (ODEs) which can then be easily solved numerically, some of these analytical simplification approaches include:

- polynomial approximation
- Padé approximation

18

- finite element method

- finite difference method

Polynomial approximation has been widely used to represent the solid and electrolyte-phases concentration profiles. This involve the introduction of several approximations using different polynomial equations with various order [18-20] including parabola and higher-order approximations. Higher-order polynomials gives a higher accuracy; but the computational cost of the coefficient identification for the model will increase accordingly [17].

Zhang *et al.* [18] proposed a single particle model with electrolyte dynamics. They modeled electrolyte concentration distribution with an approximate solution (AP-solution) to improve the model computational efficiency. The electrolyte concentration distributions were modeled as a parabolic polynomial function across the cell length. Their proposed model was developed based on the steady state solution obtained which depict that the concentration distribution at steady state at the two electrodes follows a parabolic profile and at the separator the dynamics can be modeled with a linear profile. Although the capability of their approximate solution model in accurately predicting the electrolyte concentration distribution was validated by comparing their model simulation result against that of an FDM based model at low discharge rate (up to 3C) as shown in Figure 12a. The author stated that at low discharge rate the AP-solution has some local error at both positive and negative electrode as shown in Figure 12b. Although their proposed approximate solution-based model has a higher computational efficiency, but its prediction accuracy at high charging/discharging rate is not guarantee due to the approximation technique used for the electrolyte dynamics representation.
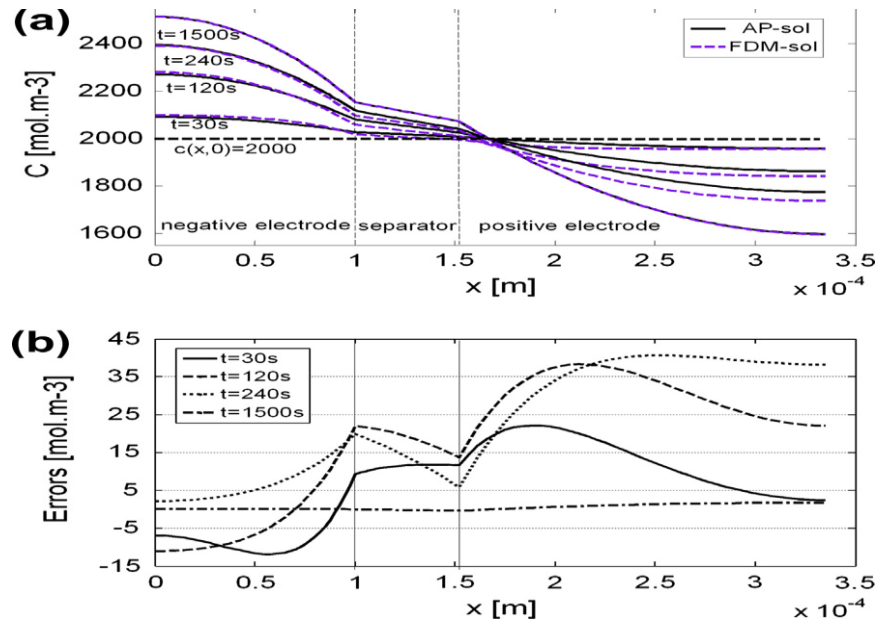
Figure 12: Comparison of the electrolyte concentration distributions at different time under 1C rate discharge calculated from our approximate solution (AP-sol) and the numerical finite difference method (FDM-sol). (b) The errors between the two solutions. [11]

Park *et al*. [17] in their work proposed a reduced order model based on SP model coupled with an electrolyte dynamic and stress induced diffusion. An approximated solution was derived for the electrolyte concentration distribution by solving the mass transport equation in the electrolyte of the cell. The electrolyte concentration profile was modeled as a quadratic function (second-order polynomial) in the two electrode and the separator. They developed the three quadratic equations to depict the concentration distribution across the cell which was solved analytically along the length of the cell under both steady and unsteady state condition. The contribution of electrolyte dynamics inclusion in the terminal voltage computation was investigated and the effect of stress induced diffusion which is due to developed mechanical expansion and contraction was also analysis and these increase the fidelity of their proposed model. The predicted concentration profile from their proposed model was solved analytically and compared against a numerical solution of the governing PDEs of the battery itself as shown in Figure 13.

20

Their model was able to predict the cell terminate voltage with high accuracy as compare to the prediction of convectional SP model. The prediction capacity of their model was validated against a full-order model result. The accuracy of their model at any C-rates above 3C becomes reduces because of the approximated solution for the electrolyte dynamics.
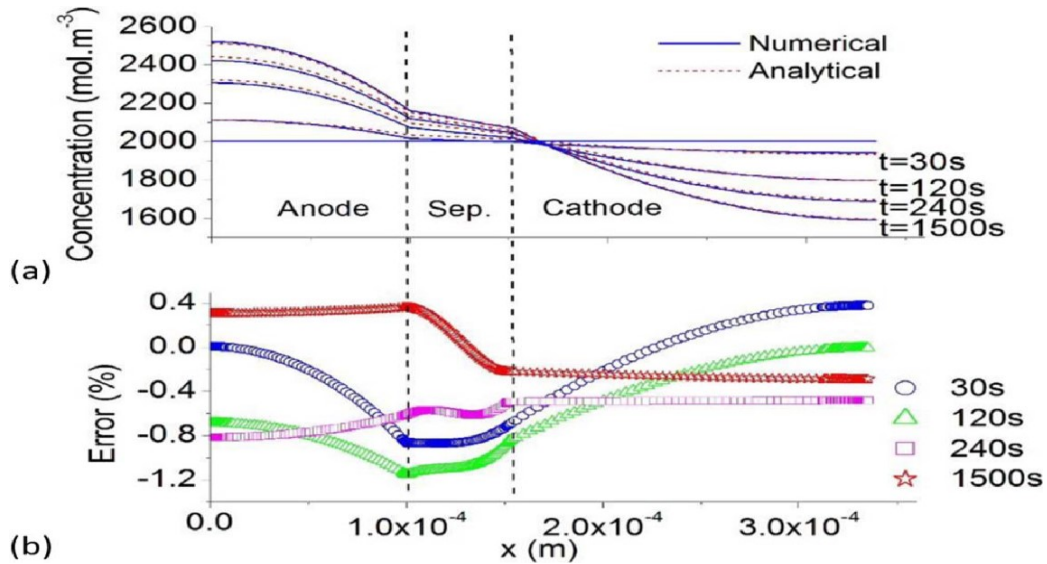
Figure 13: Comparison of the electrolyte concentration distribution at different times for a 1 C discharge rate [17]

A computational efficient implementation of full-order electrochemical model was carried out by Donkers *et al.* [16]. They developed a model order reduction approach using orthogonal decomposition and discrete empirical interpolation for spatial and temporal discretization of the full-order model. The developed reduced order nonlinear algebraic equations were solved using damped Newton's method. The simulation result of the implementation of their reduced order model shows the computation time is 3-5 times faster and model order reduced significantly by 18 times as compared to full order model. The only concern is if the implementation of this model for real time online estimation will perform accordingly [16]. Their studies propose a numerical solution for the full-order model with higher accuracy and computational efficiency, this enhance

21

the application of full-order electrochemical model for battery control design and design optimization.

Gu *et al*. [27] developed a two-dimensional model to simulate the discharging of a lithium/thionyl chloride primary battery. Their 2D model incorporates the conservation and transport of species and charge, and electrode porosity variations as well as electrolyte transport. In their proposed model, they determine the electrolyte flow occurring in the battery numerically. Numerical simulations of the PDEs solution were performed using a finite volume method. Their model was validated by comparing predicted discharge curves from their model for various temperatures against published experimental data which show good agreement and are essentially identical to the published results for a one-dimensional model as shown in Figure 14.
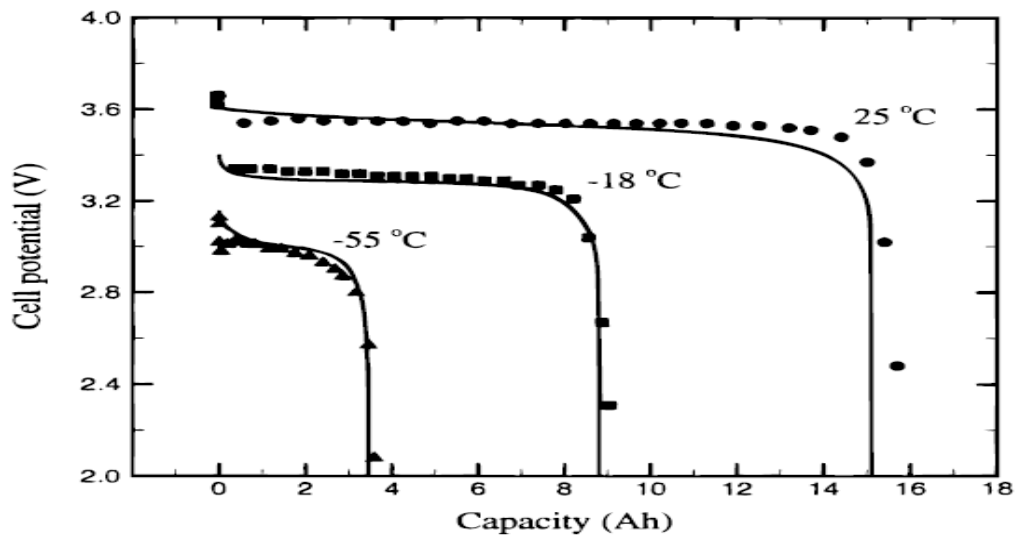
Figure 14: Comparison of experimental and predicted discharge curves for a 50 V load at 255, 218, and 258C. The symbols represent the experimental data from Jain et al., while the solid lines are the predicted results [27]

Ye et al. [28] developed their simplified model by coupling electronic conduction, mass transfer, energy balance, and electrochemical mechanisms for LIB. Lithium ion diffusivity and chemical reaction rate in the cathode material are computed for different current charge and discharge rates

22

for different operating temperature conditions. Their model computations were performed using the finite element based commercial software COMSOL MULTIPHYSICS. As lithium-ion diffusivity increases with operating temperature, the lithium-ion concentration gradient decreases which can be seen in Figure 15.
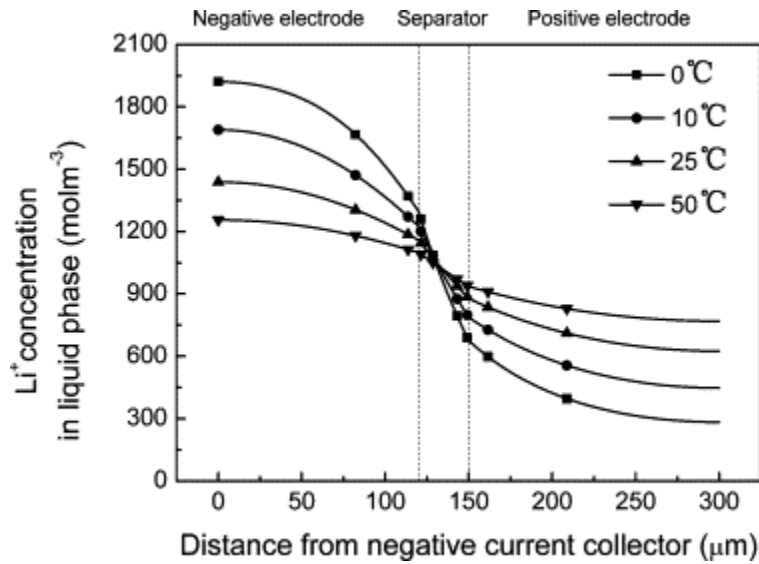
Figure 15: Lithium ion concentration distribution within liquid phase across the cell at different operation temperatures.

The simulated results showed that the lithium ion concentration gradient in both liquid and solid phase are significantly affected by temperature variation; which according to the authors, lead to capacity losses and power losses under low temperatures application. Furthermore, they studied reversible and irreversible heat generation during charging and discharging processes and suggested that a proper cooling system should be added to keep the battery temperature within the safety range.

Fathy *et al.* [51] improved the DFN model by making it more conducive and enabling for control design. They adaptively solved the DFN model's algebraic equations through quasi-linearization and they reduced the model order through Padé approximation of Fick's law of spherical diffusion.

They applied Padé approximation for model reduction purpose and the reduced model was solved numerically upon transforming the systems transfer function to state space form. According to the author, the analytic Padé approximation of spherical diffusion greatly decreases the number of diffusion states in the model while remaining very accurate which eventually reduced the model computational cost.

4.3   Motivation and Contribution

The limitations of ECM and SP model for accurate battery dynamics prediction motivates the inclusion of electrolyte dynamics to the conventional SP model, but the fidelity of this modified model depends on the methodology used in solving the PDEs capturing the battery behavior. Many different analytical approaches have been proposed for simplification of this single particle model with electrolyte dynamics. Approximation techniques and polynomial function representations have been applied in modeling the concentration profile both in solid and electrolyte phases. These approximations are done to reduce the computational cost of solving the battery PDEs. Although these analytical approximation techniques allow for a reduced computational effort for modeling and simulation purpose, but this simplification reduce the model's accuracy.

The motivation for this work is the application of a finite difference scheme to solve the battery PDEs based on a single particle model with electrolyte dynamics. This will enable the development of a robust model, capable of accurately capturing the battery dynamics under any given charging/discharging operations without any assumptions or approximations for modeling the concentration profile. This work proposed an optimal model-reduction for lithium-ion battery systems based on single particle model with electrolyte dynamics for fast computation and accurate prediction of the lithium intercalation dynamics.

The proposed optimal model-reduction is similar to the one presented in [22] which was based on SP model without the inclusion of electrolyte dynamics. The optimal model reduction will be achieved using evenly discretization nodes based SPMe as a reference for developing uneven discretization nodes based SPMe. The model reduction will allow for faster computation and reduce model complexity without any loss of physical interpretation of the diffusion and migration dynamics in solid particles and electrolyte.

4.3   Objectives

The objective of this thesis work is as follows;

- Modeling of lithium-ion single particle model with electrolyte dynamics (SPMe), using finite difference method with uneven discretization nodes to solve the battery governing PDEs for model reduction purpose.

- Optimal selection of node points using particle swarm optimization for achieving model reduction.

- Investigating the effect of increase number of node points on the performance of reduced-order model.

- Simulation of the SPMe model with three different discharging and charging operation conditions:

  - Constant Current Operation

  - Pulse Charge/Discharge Operation

  - Hybrid Pulse Power Characterization (HPPC) Operation

Chapter 2: LIB Governing Equations

Lithium-ion battery operations are captured through the governing equations which can be derived from the conservation laws for species and charge ratio, and electrochemical kinetic principle. The governing equations are expressed as a partial differential equations (PDEs) representing the conservation of mass in the solid and electrolyte phases, conservation of charge in the solid and electrolyte phases and Butler-Volmer kinetic equation describing the electro-kinetic reaction taking place at solid-electrolyte interface (SEI).

2.1 Mass Conservation in Solid Phase

From SP model assumptions, the electrodes are assumed to be composed of spherical particles and their behavior are modeled based on porous electrode theory. This theory stipulates that the solid particles are assumed to be uniformly distributed throughout the electrode and that the empty spaces between these particles are filled by electrolyte which are in liquid form. This help provides the needed environment for lithium ion intercalation and de-intercalation to take place at the interfacial surface of solid and electrolyte particles for electrochemistry process to occur. Electrochemical reaction being an interfacial phenomenon, occurs where at the surface where the liquid meets with solid because of the porous nature of the electrodes. Porous electrodes offer a high surface area, allowing a lot of reaction to be packed into a small space within both the positive and negative electrodes.

The solid phase lithium ion concentration in the solid particle is model by the diffusion equation according to Fick's second law. Only one spherical particle is used to model negative and positive electrode respectively based on the single particle model assumptions which is used to simplify each electrode modelling procedure since all particles in the electrodes are uniform in size, and the current distribution is assumed to be uniform along the thickness of the porous electrode. The mathematical model capturing the concentration dynamics in the spherical coordinate system is given as,

$$\frac{\partial C_{s,i}}{\partial t} = \frac{D_s}{r^2} \frac{\partial}{\partial r}\left(r^2 \frac{\partial C_{s,i}}{\partial r}\right), \tag{1}$$

where C_s denote solid phase lithium ion concentration in the electrode, D_s is the solid phase diffusivity coefficient which is a constant value, r is the particle radius under consideration and the subscript I denotes either positive or negative electrode. The two-boundary conditions for solid phase concentration dynamics exist at the particle core and surface. The mass flux of lithium ions at the center of the spherical particle at $r = 0$ is zero due to the symmetry and the zero gradient boundary condition is expressed as;

$$\frac{\partial C_s}{\partial r}\Big|_{r=0} = 0, \tag{2}$$

while the mass flux of lithium ions at the surface of the spherical particle at r =R$_s$ is expressed as;

$$-D_s \frac{\partial C_s}{\partial r}\Big|_{r=R_s} = \frac{J_{Li}}{a_s F}, \tag{3}$$

where F is the faradays constant, a_s is the interfacial surface area of the particles which is given as;

$$a_s = \frac{3\epsilon_s}{R_s}. \tag{4}$$

The active interfacial surface area (a_s) is the area to volume ratio of the active spherical particles. The lithium ion molar flux density J_{Li} is the ratio of input current to volume, measured in Ampere per unit volume as given by,

$$J_{Li} = \frac{I(t)}{AL_i} \tag{5}$$

where I is the applied current which is a function of time, A is the area of the particle itself and L_i is the length of the electrode with $i=p/n$, representing positive and negative electrode. It is noted that input current is negative for positive electrode and positive for negative electrode during discharging process.

2.2 Mass Conservation in Electrolyte Phase

Transportation of lithium-ion in the electrolyte occurs through molecular diffusion and electric migration. The electrolyte phase concentration distribution can be derived from the conservation of mass principle. The mass conservation principle is applied to the three regions through which the electrolyte flows; a negative electrode, a separator and a positive electrode. Transfer of electrolyte-phase lithium ion is governed by a porous electrode theory. At the separator, the transfer of lithium-ion in the electrolyte is governed by Fick's first law since there is no intercalation/de-intercalation of lithium-ion in this region. The lithium-ions transfer in the two electrodes are governed by Fick's second law [17]. The mathematical model of this transfer process is expressed as;

Negative Electrode Region:

$$\epsilon_n \frac{\partial C_{e,n}}{\partial t} = \frac{\partial}{\partial x}\left(D_{e,n}^{eff} \frac{\partial C_{e,n}}{\partial x}\right) + \frac{\left(1-t_f^+\right)}{F} J_{Li} \tag{6}$$

Separator Region:

$$\epsilon_s \frac{\partial C_{e,s}}{\partial t} = \frac{\partial}{\partial x}\left(D_{e,s}^{eff} \frac{\partial C_{e,s}}{\partial x}\right) \tag{7}$$

Positive Electrode Region:

$$\epsilon_p \frac{\partial C_{e,p}}{\partial t} = \frac{\partial}{\partial x}\left(D_{e,p}^{eff} \frac{\partial C_{e,p}}{\partial x}\right) + \frac{\left(1-t_f^+\right)}{F} J_{Li} \tag{8}$$

where $C_{e,n/s/p}$ is the electrolyte phase concentration across each of the regions, $\epsilon_{n/s/p}$ is the electrolyte phase volume fraction in the three regions, $D_{e,n/s/p}^{eff}$ is the effective diffusivity coefficient which is a function of electrolyte phase volume fraction and Bruggeman's constant in each of the three region and it is expressed as $D_{e,i}^{eff} = D_{e,i}\,\epsilon_i^{brug}$. The variable $D_{e,i}$ is the electrolyte diffusion coefficient, J_{Li} is the transfer current density, i denoting each of the three regions, and t_f^+ is the transference number which is assumed to be constant. This concentration distribution across the entire length of the cell is subject to the following boundary conditions;

at the two-current collectors' side,

$$\frac{\partial C_{e,n}}{\partial x}\Big|_{x=0} = 0, \tag{9}$$

$$\frac{\partial C_{e,p}}{\partial x}\Big|_{x=L} = 0. \tag{10}$$

Likewise, at the boundary of negative electrode-separator and separator-positive electrode there is a continuity boundary condition for both;

$$D_{e,n}^{eff} \frac{\partial C_{e,n}}{\partial x}\big|_{x=Ln} = D_{e,s}^{eff} \frac{\partial C_{e,s}}{\partial x}\big|_{x=Ln} \, , \quad D_{e,s}^{eff} \frac{\partial C_{e,s}}{\partial x}\big|_{x=Ln+Ls} = D_{e,p}^{eff} \frac{\partial C_{e,p}}{\partial x}\big|_{x=Ln+Ls} \quad (11)$$

$$C_{e,n(x=L_n)} = C_{e,s(x=L_n)} \, , \quad C_{e,s(x=L_n+L_s)} = C_{e,p(x=L_n+L_s)} \tag{12}$$

2.3 Conservation of Charge in Solid Phase

The charge conservation for solid phase is governed by the current conservation principle. The current conservation equation states that the partial derivative of electric potential divergent due to the electrons transfer with respect to spherical space is equal to the lithium-ion molar flux density J_{Li} as given by,

$$\frac{\partial}{\partial x}\left(\sigma^{eff} \nabla \varphi_s\right) = J_{Li} \, , \tag{13}$$

where σ^{eff} is the electrical conductivity of the two electrodes which is dependent on Bruggeman's constant and solid volume fraction value, φ_s is the solid electric potentials for each of the electrodes and J_{Li} is the molar flux which is dependent on the current density. The charge conservation equation above is solved for each electrode and subject to the boundary conditions that at the two current collectors' side, the gradient of the solid electric potential (φ_s) are both equal but opposite in sign and equals to the current density measure in Ampere per square meter;

$$-\sigma^{eff} \frac{\partial \varphi_{s,n}}{\partial x}\big|_{x=0} = \sigma^{eff} \frac{\partial \varphi_{s,p}}{\partial x}\big|_{x=Ln} = \frac{I}{A} \tag{14}$$

where I is input current, A is the area of each electrode which mostly are assumed to be the same for the two electrodes. Furthermore, there is a no-current flow boundary conditions at the interface of both negative electrode-separator and separator-positive electrode this is because no electronic lithium can follow across the electrode boundary into the separator;

$$\frac{\partial \varphi_s}{\partial x}\Big|_{x=Ln} = \frac{\partial \varphi_s}{\partial x}\Big|_{x=Ln+Ls+Lp} = 0 \tag{15}$$

2.4 Conservation of Charge in Electrolyte Phase

The governing equation ensuring conservation of charge in the electrolyte phase is expressed as;

$$\frac{\partial}{\partial x}\left(\kappa^{eff}\frac{\partial}{\partial x}\varphi_e\right) + \frac{\partial}{\partial x}\left(\kappa_d^{eff}\frac{\partial}{\partial x}(In\ Ce)\right) = -J_{Li}, \tag{16}$$

the variable C_e is the electrolyte phase lithium ion concentration, φ_e is the electrolyte phase electric potential and $\kappa^{eff} = \kappa\epsilon_e^{brug}$ is the effective ionic conductivity which is concentration dependent. The first term in the equation above is the contribution of lithium ion transport due to electrical conductivity while the second term represent the contribution of diffusion of lithium ion in the electrolyte due to concentration gradient. The variable k_d^{eff} is the effective diffusional coefficient and is expressed as;

$$\kappa_d^{eff} = \frac{2RT\kappa^{eff}}{F}(t_+ - 1)(1 + \frac{\partial ln f_{c/a}}{\partial ln\ Ce}). \tag{17}$$

The parameter $f_{c/a}$ is the mean molar activity coefficient in electrolyte. The diffusional conductivity is dependent on the ionic conductivity κ and can be calculated by virtue of concentrated solution theory. The first term in equation (16) above is the contribution of lithium ion flux due to electrical conductivity and the second term is the contribution of lithium ion diffusion due to concentration gradient. The combined effect of these two processes results in the movement of solid phase lithium ion into electrolyte phase lithium ion and the migration of the electrolyte phase lithium ions. The only boundary condition for conservation of charge in the

electrolyte is due to the inability of electrolyte to flow pass the two current collectors at the extreme of the two electrodes,

$$\frac{\partial \varphi_e}{\partial x}\Big|_{x=0} = \frac{\partial \varphi_e}{\partial x}\Big|_{x=L} = 0. \tag{18}$$

The current density per unit volume for both negative and positive electrode satisfies the conditions;

$$\int_0^{Ln} J_{Li,n}\, dx = \frac{I}{A\delta x} = J_{Li,n}, \qquad \int_0^{Ln} J_{Li,n}\, dx = \frac{I}{A\delta x} = J_{Li,n}. \tag{19}$$

Equation (16) can be simplified analytically with Equations (17), (18) and (19) as;

$$\varphi_e(L,t) - \varphi_e(0,t) = \left(1 - t_f^+\right)\frac{2RT}{F} \ln\left(\frac{C_{e,p}\,(L,t)}{C_{e,n}\,(0,t)}\right) - \frac{I}{2}\left(\frac{L_n}{\kappa_n^{eff}} + \frac{2L_s}{\kappa_s^{eff}} + \frac{L_p}{\kappa_p^{eff}}\right) \tag{20}$$

The electrical potential difference between the two electrode sides account for the overpotential due to electrolyte mass transfer (diffusion and migration) across the entire cell. The first term is the overpotential due to diffusion of lithium ion caused by concentration gradient in the electrolyte while the second term is known as Ohmic resistance and can be determined experimentally with the help of an electrochemical impedance spectroscopy.

2.5 Butler-Volmer Kinetic Equation

Intercalation/de-intercalation reaction occurs at the solid-electrolyte interface and is governed by the Butler-Volmer kinetic equation which interconnects the solid-phase concentration dynamics to the electrolyte-phase concentration dynamics. The lithium-ion molar flux occurs at the interface of solid active particle and electrolyte and serve as the driving force responsible for the movement of lithium ion into and out of both particles. The movement of ion within the solid-electrolyte

interface (SEI) is modeled by the diffusion equation which is controlled by the Butler-Volmer current density at the surface of the spherical particle;

$$J_{Li,p} = a_{s,p} i_{o,p} \left(exp(\frac{F}{2RT}\eta_p) - exp(-\frac{F}{2RT}\eta_p) \right)$$ (21)

$$J_{Li,n} = a_{s,n} i_{o,n} \left(exp(\frac{F}{2RT}\eta_n) - exp(-\frac{F}{2RT}\eta_n) \right)$$ (22)

where $i_{o,n/p}$ is the exchange current density in the electrodes. For most battery models, the exchange current is assumed to be constant for model simplification but in this work, the exchange current density is computed for each time step as;

$$i_{o,p}(t) = \kappa_p^0 c_{e,p}^{\alpha_c} (c_{s,p,max} - c_{s,surf,p})^{\alpha_c} c_{s,surf,p}^{\alpha_c},$$

$$i_{o,n}(t) = \kappa_n^0 c_{e,n}^{\alpha_a} (c_{s,n,max} - c_{s,surf,n})^{\alpha_a} c_{s,surf,n}^{\alpha_a},$$ (23)

where α_a and α_c are the anodic and cathodic charge transfer coefficients respectively and they are assumed to be 0.5, the exchange current density is dependent on the difference between the maximum possible concentration of the electrode and its surface concentration and the average electrolyte phase lithium-ion concentration across each of the electrodes. The variables κ_p^0 and κ_n^0 are the kinetic reaction rate for both negative and positive electrode respectively.

Furthermore, η_p^k and η_n^k are positive and negative kinetic overpotentials respectively, and are the difference between the solid and electrolyte phase electrical potentials expressed as,

$$\eta_p = \frac{2RT}{F} \ln \left(\xi_p^2 + \sqrt{1 + \xi_p^2} \right)$$ (24)

$$\eta_n = \frac{2RT}{F} \ln \left(\xi_n^2 + \sqrt{1 + \xi_n^2} \right)$$ (25)

where; $\quad \xi_p = \frac{J_{Li,p}}{2a_{s,p} i_{o,p}} \quad$ and $\quad \xi_n = \frac{J_{Li,n}}{2a_{s,n} i_{o,n}}$

33

The voltage drop due to difference in kinetic overpotential for the two electrodes can be expressed as;

$$\eta_p - \eta_n = \frac{2RT}{F} \ln \left(\frac{\xi_p^2 + \sqrt{1+\xi_p^2}}{\xi_n^2 + \sqrt{1+\xi_n^2}} \right) \tag{26}$$

2.6 Cell Terminal Voltage

The cell terminal voltage is expressed as the difference between the solid phase potential difference of the two electrodes. The potential difference result into a flow of current to an external connected load and it is the addition of open circuit potential ($U_{p/n}$), electrolyte phase potential difference ($\varphi_{e,p/n}$) and kinetic overpotential ($\eta_{p/n}$) for each of the electrode. The open circuit potential is expressed as a function of normalized surface concentration for each of the two electrodes. The terminal voltage is determined by;

$$V(t) = \varphi_{s,p}|_{x=L} - \varphi_{s,n}|_{x=0} \tag{27}$$

where for positive electrode;

$$\varphi_{s,p}|_{x=L} = U_p + \eta_p + \varphi_{e,p} \tag{28}$$

And for negative electrode;

$$\varphi_{s,n}|_{x=0} = U_n + \eta_n + \varphi_{e,n} \tag{29}$$

Therefore, the cell voltage can be expressed as follows;

$$V(t) = (U_p + \eta_p + \varphi_{e,p}) - (U_n + \eta_n + \varphi_{e,n}) \tag{30}$$

$$= (U_p - U_n) + (\eta_p - \eta_n) + (\varphi_{e,p} - \varphi_{e,n}) - \frac{R_f}{A} I(t)$$

34

where R_f is the resistance developed at the electrode-current collector interface. The cell open circuit voltage, $(U_p - U_n)$ is dependent on the battery chemistry. The LIB systems considered in this work has a LiCoO$_2$ positive electrode active material and graphite as its negative electrode active material.

The equilibrium potentials for negative and positive electrodes are from [30] and are expressed as below;

U_n = 0.194+1.5*exp(-120.0* θ_x) + 0.0351*tanh((θ_x-0.286)/0.083) − 0.0045*tanh((θ_x -

0.849)/0.119) ‐ 0.035*tanh((θ_x -0.9233)/0.05) ‐ 0.0147*tanh((θ_x – 0.5)/0.034) –

0.102*tanh((θ_x -0.194)/0.142) ‐ 0.022*tanh((θ_x -0.9)/0.0164) − 0.011*tanh((θ_x -

0.124)/0.0226) + 0.0155*tanh((θ_x -0.105)/0.029). (31)

U_p = 2.16216+0.07645*tanh(30.834-54.4806* θ_y) + 2.1581*tanh(52.294−50.294* θ_y) −

0.14169*tanh(11.0923-19.8543* θ_y) + 0.2051*tanh(1.4684−5.4888* θ_y) +

0.2531*tanh((−θ_y +0.56478)/0.1316) − 0.02167*tanh((θ_y −0.525)/0.006). (32)

The variable $\theta_x = \dfrac{C_{se,n}}{C_{s,n,max}}$ and $\theta_y = \dfrac{C_{se,p}}{C_{s,p,max}}$ where $C_{se,p/n}$ is the solid-phase surface concentration for positive and negative electrodes respectively.

Conclusively, the battery terminal voltage can be expressed in the simplified form as;

$$V(t) = \left(U_p(\theta_y) - U_n(\theta_x)\right) + \frac{2RT}{F} ln\left(\frac{\xi_p^2 + \sqrt{1+\xi_p^2}}{\xi_n^2 + \sqrt{1+\xi_n^2}}\right) - \frac{R_f}{A}I$$

$$+ \left(1 - t_f^+\right)\frac{2RT}{F} ln\left(\frac{C_{e,p}(L,t)}{C_{e,n}(0,t)}\right) - \frac{I}{2}\left(\frac{L_n}{\kappa_n^{eff}} + \frac{2L_s}{\kappa_s^{eff}} + \frac{L_p}{\kappa_p^{eff}}\right) \tag{33}$$

Chapter 3: Discretization Techniques

Lithium-ion battery operations are governed by the partial differential equations as stated in Chapter two. The PDEs are further simplified for modeling and simulation purpose by applying Finite Difference Method (FDM) schemes to discretize the PDEs into a corresponding set of ordinary differential equations (ODEs) as applied [14]. The set of ordinary differential equations are thereafter solved numerically in MATLAB. In applying FDM a second order of approximation was employed for time and spatial domain quantity approximation. Second order forward difference approach was applied for time-variance quantity while second order central difference approach was applied for spatial-variance quantity. The numerical solutions to the ODEs are then used in computing the terminal voltage of the battery system under analysis. This chapter is structure such that the FDM applied to the governing equations is first described, followed by the description of numerical solution methodology employed in solving the ODEs, and the battery parameters used for this work is presented.

3.1 Finite Difference Method (FDM)

Finite difference method is used in converting the complex PDEs into a more numerical solution friendly ODEs. The FDM gives an approximated form of the differential equations as a difference equation. Hence, FDM is used in this modeling procedure to discretize the lithium-ion battery governing equations [1,6,7,8,12,20].

There are two approaches to FDM solutions, based on the grid size across the entire domain of interest. It can either be a uniform grid or non-uniform grid size FDM. For a uniform grid scheme, grid size is the same across the entire domain of interest while a non-uniform scheme has a varying grid size across the domain of interest as shown in Figure 16. Both uniform and non-uniform grid schemes are applied in this work to discretize the battery PDEs. From Taylor series expansion, we can write the expression for a dependent quantity as a function of an independent quantity, thus, for this work solid-phase and electrolyte-phase concentration are the dependent quantity changing with time, t, and position, r and x, being the independent quantities.
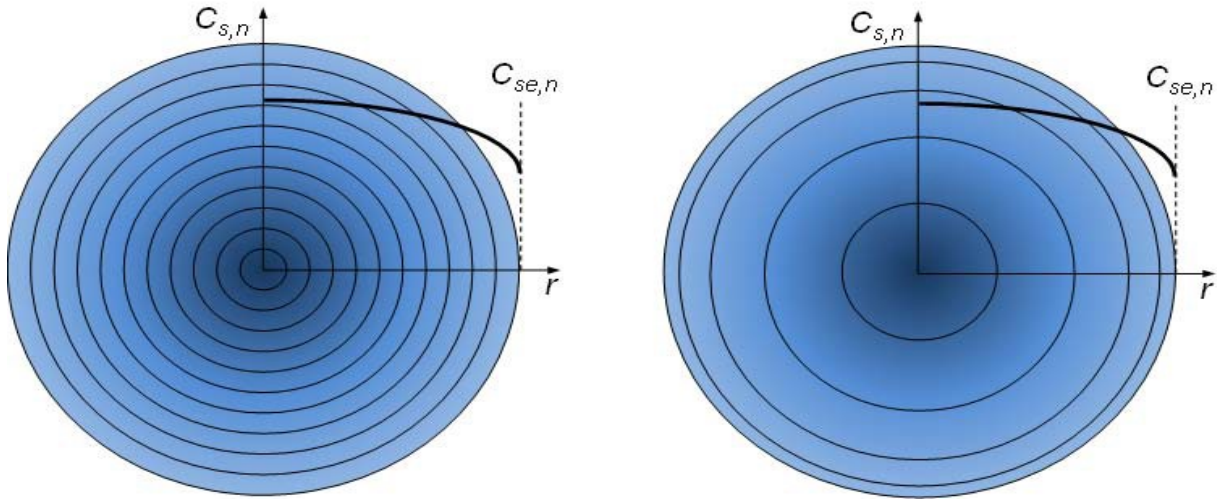
Figure 16: Illustration of different discretization approaches: (a) even discretization; (b) uneven discretization [22]

3.2 FDM Uniform Grid Size Scheme

Uniform grid size FDM scheme entails the uniformity of the dimension of the grid into which the entirety of domain of interest is divided. The spherical particle radius representing each electrode are discretized evenly (uniform) from the core to the particle surface to compute solid-phase concentration distribution across each electrode. The same evenly discretized methodology will

be applied across the length of both electrode and separator in computing the electrolyte phase concentration distribution.

The general Taylor series expansions with uniform grid size are given as;

$$f(x_{i+1}) = f(x_i) + \Delta x f'(x_i) + \frac{(\Delta x)^2}{2!} f''(x_i) + \frac{(\Delta x)^3}{3!} f'''(x_i) + HOT$$

$$f(x_{i-1}) = f(x_i) - \Delta x f'(x_i) + \frac{(\Delta x)^2}{2!} f''(x_i) - \frac{(\Delta x)^3}{3!} f'''(x_i) + HOT \tag{34}$$

From these equations, f' and f'' can be obtained as follows,

$$f'(x_i) \approx \frac{f(x_{i+1}) - f(x_{i-1})}{2\Delta x}$$

$$f''(x_i) \approx \frac{f(x_{i+1}) - 2f(x_i) + f(x_{i-1})}{(\Delta x)^2} \tag{35}$$

Equation (35) will be employed in solving the battery PDEs, the solid-phase or electrolyte phase concentration $(C_s$ or $C_e)$ can be substituted in place of function (f) in the simplified Taylor series expansion expression.

3.2.1 Solid-Phase Concentration Solution

The PDEs governing the concentration distribution in the solid-phase across the particle radius is solved through the FDM with even discretization by diving the particle radius into N-1 numbers of grids as shown in Figure 17, where each grid is of the size;
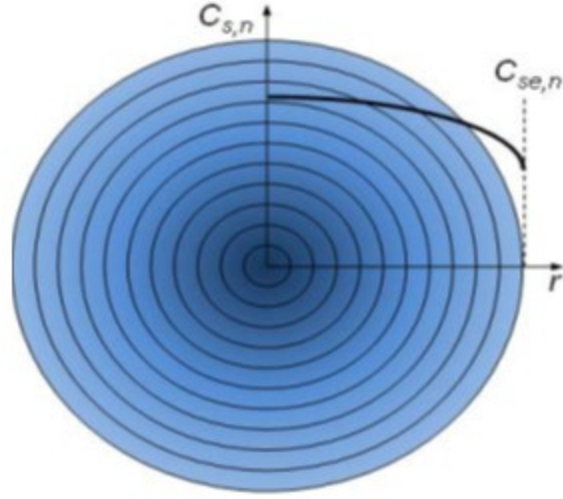
Figure 17 Evenly Discretized Particle Radius [22]

$$\Delta r = \frac{R_s}{N} \qquad (36)$$

the parameter R_s is the particle radius, N is the total number of node points across the particle

radius including the boundary. The particle radius is evenly discretized into

$$\mathrm{r} = \begin{bmatrix} r_1 \; r_2 \; r_3 \; \dots \; r_{N-2} \; r_{N-1} \; r_N \end{bmatrix}^{\mathrm{T}}$$

$$\Delta r_i = r_{i+1} - r_i = \frac{R_s}{N} \qquad (37)$$

by applying the state-space representation approach, Equation (1) can be represented as;

$$\dot{C}_s = A_{cs} C_s + B_{cs} J_{Li} \qquad (38)$$

Where A_{cs} is a constant tri-diagonal matrix which is computed from Equation (1) and (36) and it

is solid-phase diffusion coefficient dependent. The matrix B_{cs} corresponds to the contribution of

the boundary condition being the driving force for lithium ion flux across the particle. The state C_s

is expressed as,

$$C_S = [C_{S,1}\ C_{S,2}\ C_{S,3}\ ...\ C_{S,N-2}\ C_{S,N-1}]^T \tag{39}$$

Equation (32) can be simplify as;

$$\frac{\partial C_{S,i}}{\partial t} = \frac{D_s}{r_i(\Delta r_i)^2}\left[(r_i - \Delta r_i)C_{S,i-1} - 2r_iC_{S,i} + (r_i + \Delta r_i)C_{S,i+1}\right] \tag{40}$$

Applying the boundary conditions at r=0 and r=R_s to Equation (41) gives the boundary point concentration distribution a simplified expression.

At the electrode core, $\quad \frac{\partial C_s}{\partial r}\big|_{r=0} = \frac{C_{S,1} - C_{S,0}}{\Delta r_1} = 0;\quad$ therefore substituting $C_{S,0} = C_{S,1}$ into

equation above gives;

$$\frac{\partial C_{S,1}}{\partial t} = \frac{D_s(r_1 + \Delta r_1)}{r_1(\Delta r_1)^2}\left[-C_{S,1} + C_{S,2}\right] \tag{41}$$

Also, at r=R_s the BC is $-D_s\frac{\partial C_s}{\partial r}\big|_{r=R_s} = \frac{J_{Li}}{a_sF}$ where J_{Li} is as expressed in Equation (19a) and

(19b) for the two electrodes. Hence,

$$-\frac{\partial C_s}{\partial r}\big|_{r=R_s} = \frac{C_{S,N} - C_{S,N-1}}{\Delta r_{N-1}} = -\frac{I}{D_s a_s FAL_n} \tag{42}$$

Equation (40) can be expressed in term of $C_{S,N-1}$ and substituting this into Equation (38) gives;

$$\frac{\partial C_{S,N-1}}{\partial t} = \frac{D_s(r_{N-1} - \Delta r_{N-1})}{r_{N-1}(\Delta r_{N-1})^2}\left[C_{S,N-2} - C_{S,N-1}\right] - \frac{(r_{N-1} + \Delta r_{N-1})}{r_{N-1}\Delta r_{N-1}}\frac{I(t)}{a_sFAL_n} \tag{43}$$

Therefore, the constant A_{cs} tri-diagonal matrix and input B_{cs} matrix are formulated as;

$$A_{cs} = \begin{bmatrix} -\dfrac{D_s(r_1 + \Delta r_1)}{r_1(\Delta r_1)^2} & \dfrac{D_s(r_1 + \Delta r_1)}{r_1(\Delta r_1)^2} & 0 & \cdots & 0 & 0 \\ \dfrac{D_s(r_i - \Delta r_i)}{r_i(\Delta r_i)^2} & \dfrac{-2D_s r_i}{r_i(\Delta r_i)^2} & \dfrac{D_s(r_i + \Delta r_i)}{r_i(\Delta r_i)^2} & 0 & \cdots & 0 \\ 0 & \ddots & \ddots & \ddots & 0 & \vdots \\ \vdots & 0 & \ddots & \ddots & \ddots & 0 \\ 0 & 0 & \cdots & 0 & \dfrac{D_s(r_{N-1} - \Delta r_{N-1})}{r_{N-1}(\Delta r_{N-1})^2} & -\dfrac{D_s(r_{N-1} - \Delta r_{N-1})}{r_{N-1}(\Delta r_{N-1})^2} \end{bmatrix}$$

$$B_{cs,n} = \begin{bmatrix} 0 & \cdots & 0 & -\frac{(r_{N-1}+\Delta r_{N-1})}{r_{N-1}\Delta r_{N-1}a_s FAL_n} \end{bmatrix}^T$$

$$B_{cs,p} = \begin{bmatrix} 0 & \cdots & 0 & \frac{(r_{N-1}+\Delta r_{N-1})}{r_{N-1}\Delta r_{N-1}a_s FAL_p} \end{bmatrix}^T \tag{44}$$

The matrix A_{cs} has the same structure for both electrodes except their D_s which differs.
Simplification of Equation (38) gives;

$$\frac{C_{s,i+1}-C_{s,i}}{\Delta t} = A_{cs}C_{s,i} + B_{cs}I(t)$$

$$C_{s,i+1} = (1 + A_{cs}\Delta t)\,C_{s,i} + \Delta t B_{cs}I(t) \tag{45}$$

The solid-phase concentration distribution is computed from Equation (45) as a function of time
and position. The concentration at any time step ($i+1$) is computed based on the concentration
value of the present time step, I, the boundary condition, and the constant A_{cs} and B_{cs} matrix.

3.2.2 Electrolyte-Phase Concentration Solution

The PDEs representing the conservation of species for electrolyte-phase is used to model the
electrolyte-phase concentration distribution across the entire length of the cell. These PDEs are
evenly discretized for the two electrodes and the separator, since the concentration dynamics in
negative electrode is monotonic to that of positive electrode, therefore the same analysis structure
is applied to both electrodes and at such the ODEs that will be developed for the negative electrode
will be similar to positive electrode ODEs with appropriate parameters substitution. Although
some researchers have investigated the effect of electrolyte phase diffusion coefficient dependency
(D_e) on concentration and their results show the sensitivity of diffusion coefficient to the
concentration dynamics. But for simplification purpose a constant diffusion coefficient (D_e)
computed based on the electrolyte average concentration is assumed in this work. Based on this

assumption of constant diffusion coefficient, the governing PDE in Equations (6), (7), and (8) can be simplified as follows;

Negative Electrode Region: $0 \leq x_n \leq L_n$

$$\epsilon_n \frac{\partial C_{e,n}}{\partial t} = D_{e,n}^{eff} \frac{\partial^2 C_{e,n}}{\partial x^2} + \frac{\left(1-t_f^+\right)}{F} J_{Li} \tag{46}$$

Separator Region: $L_n \leq x_s \leq L_n + L_s$

$$\epsilon_s \frac{\partial C_{e,s}}{\partial t} = D_{e,s}^{eff} \frac{\partial^2 C_{e,s}}{\partial x^2} \tag{47}$$

Positive Electrode Region: $L_n + L_s \leq x_p \leq L_n + L_s + L_p$

$$\epsilon_p \frac{\partial C_{e,p}}{\partial t} = D_{e,p}^{eff} \frac{\partial^2 C_{e,p}}{\partial x^2} + \frac{\left(1-t_f^+\right)}{F} J_{Li} \tag{48}$$

The length of each of the electrodes and separator were divided into *N and N$_s$* equal grid size respectively as expressed in Equation (49). The chosen number of nodes for each region is as presented in Table 1.

$$\Delta x_n = \Delta x_p = \frac{L_{n/p}}{N}$$

$$\Delta x_s = \frac{L_s}{N_s} \tag{49}$$

From the state-space representation approach, Equation (6) can be represented as;

$$\dot{C}_e = A_{ce} C_e + B_{ce} I \tag{50}$$

The parameter A_{ce} is a constant tri-diagonal matrix which is computed based on Equation (6), (7), (8) and (35) and it is dependent on electrolyte-phase diffusion coefficient (D_e). The column

matrix B_{ce} corresponds to the contribution of the boundary condition in each of the three regions.

The state variable C_e is expressed as;

$$C_e = [C_{e,1}^n \ C_{e,2}^n \ldots C_{e,N-1}^n C_{e,2}^s \ C_{e,3}^s \ldots C_{e,N-1}^s \ C_{e,2}^p \ C_{e,3}^p \ldots C_{e,N-1}^p]^T \qquad (51)$$

Applying Taylor series expansion to Equations (46), (47) and (48) above to simplify the PDEs yields;

Negative Electrode Region: $0 \leq x_n \leq L_n$

$$\frac{\partial C_{e,i}^n}{\partial t} = \frac{D_{e,n,i}^{eff}}{\xi_n (\Delta x_{e,i}^n)^2} [C_{e,i-1}^n - 2C_{e,i}^n + C_{e,i+1}^n] + \frac{(1-t_f^+)}{\xi_n F L_n A} I(t) \qquad (52)$$

From the boundary condition, $C_{e,1}^n = C_{e,2}^n$, and hence

$$\frac{\partial C_{e,1}^n}{\partial t} = \frac{D_{e,n,1}^{eff}}{\xi_n (\Delta x_{e,1}^n)^2} [-C_{e,1}^n + C_{e,2}^n] + \frac{(1-t_f^+)}{\xi_n F L_n A} I(t) \qquad (53)$$

From the boundary condition, the Nth-Node dynamics can be expressed as,

$$\frac{\partial C_{e,N-1}^n}{\partial t} = \frac{D_{e,n,N-1}^{eff}}{\xi_n (\Delta x_{e,N-1}^n)^2} [C_{e,N-2}^n - 2C_{e,N-1}^n + C_{e,N}^n] + \frac{(1-t_f^+)}{\xi_n F L_n A} I(t) \qquad (54)$$

Since $D_{e,n}^{eff} \frac{\partial C_{e,n}}{\partial x} |_{x=Ln} = D_{e,s}^{eff} \frac{\partial C_{e,s}}{\partial x} |_{x=Ls}$, $C_{e,N}^n$ can be expressed in terms of

$C_{e,N-2}^n, C_{e,N-1}^n, C_{e,2}^s$ and substituted into Equation (54).

Separator Region: $L_n \leq x_s \leq L_n + L_s$

$$\frac{\partial C_{e,i}^s}{\partial t} = \frac{D_{e,s,i}^{eff}}{\xi_s (\Delta x_{e,i}^s)^2} [C_{e,i-1}^s - 2C_{e,i}^s + C_{e,i+1}^s] + \frac{(1-t_f^+)}{\xi_s F L_s A} I(t) \qquad (55)$$

44

Since at the first node, $C_{e,N}^n = C_{e,1}^s$ and $C_{e,1}^s$ can be derived from the given boundary condition at L_n. Thus,

$$\frac{\partial C_{e,2}^s}{\partial t} = \frac{D_{e,s,1}^{eff}}{\xi_s (\Delta x_{e,1}^s)^2} [C_{e,N}^n - 2C_{e,2}^s + C_{e,3}^s] \tag{56}$$

The Nth-Node dynamics is expressed as,

$$\frac{\partial C_{e,N-1}^s}{\partial t} = \frac{D_{e,s,N-1}^{eff}}{\xi_s (\Delta x_{e,N-1}^s)^2} [C_{e,N-2}^s - 2C_{e,N-1}^s + C_{e,N}^s] \tag{57}$$

since $D_{e,n}^{eff} \frac{\partial C_{e,n}}{\partial x}|_{x=Ln} = D_{e,s}^{eff} \frac{\partial C_{e,s}}{\partial x}|_{x=Ls}$, this implies that $C_{e,N}^s$ can be expressed in terms

$C_{e,N-2}^s$, $C_{e,N-1}^s$, $C_{e,2}^p$ and substituted into Equation (57).

Positive Electrode Region: $L_n + L_s \leq x_p \leq L_n + L_s + L_p$

$$\frac{\partial C_{e,i}^p}{\partial t} = \frac{D_{e,p,i}^{eff}}{\xi_p (\Delta x_{e,i}^p)^2} [C_{e,i-1}^p - 2C_{e,i}^p + C_{e,i+1}^p] + \frac{(1-t_f^+)}{\xi_p F L_p A} I(t) \tag{58}$$

Since at the first node, $C_{e,N}^s = C_{e,1}^p$ and $C_{e,1}^p$ can be derived from the given boundary condition at $L_n + L_s$. Thus,

$$\frac{\partial C_{e,1}^p}{\partial t} = \frac{D_{e,p,1}^{eff}}{\xi_p (\Delta x_{e,1}^p)^2} [C_{e,N}^s - 2C_{e,2}^p + C_{e,3}^p] + \frac{(1-t_f^+)}{\xi_p F L_p A} I(t) \tag{59}$$

At the Nth-Node point, there is a zero gradient boundary condition, Equation (55) can be expressed as,

$$\frac{\partial C^p_{e,N-1}}{\partial t} = \frac{D^{eff}_{e,p,N-1}}{\xi_p(\Delta x^p_{e,N-1})^2} \left[C^p_{e,N-2} - C^p_{e,N-1} \right] + \frac{\left(1-t^+_f\right)}{\xi_p F L_p A} I(t) \tag{60}$$

Hence, the constant tri-diagonal matrix A_{ce} and input matrix B_{ce} are formulated as below;

$$A_{ce} = \begin{bmatrix} A_{neg} & 0 & 0 \\ 0 & A_{sep} & 0 \\ 0 & 0 & A_{pos} \end{bmatrix}$$

where matrix A_{neg} , A_{sep} and A_{pos} corresponds to the coefficient matrix for the negative electrode, separator, and positive electrode as expressed below;

$$A_{neg} = \begin{bmatrix} -\dfrac{D^{eff}_{e,n,1}}{\xi_n(\Delta x^n_{e,1})^2} & \dfrac{D^{eff}_{e,n,1}}{\xi_n(\Delta x^n_{e,1})^2} & 0 & \cdots & 0 & 0 \\ \dfrac{D^{eff}_{e,n,1}}{\xi_n(\Delta x^n_{e,i})^2} & \dfrac{-2D^{eff}_{e,n,2}}{\xi_n(\Delta x^n_{e,i})^2} & \dfrac{D^{eff}_{e,n,3}}{\xi_n(\Delta x^n_{e,i})^2} & 0 & \cdots & 0 \\ 0 & \ddots & \ddots & \ddots & 0 & \vdots \\ \vdots & 0 & \ddots & \ddots & \ddots & 0 \\ 0 & 0 & \cdots & \dfrac{D^{eff}_{e,n,N-1}}{\xi_n(\Delta x^n_{e,N-1})^2} & \dfrac{-2D^{eff}_{e,n,N-1}}{\xi_n(\Delta x^n_{e,N-1})^2} & \dfrac{D^{eff}_{e,n,N-1}}{\xi_n(\Delta x^n_{e,N-1})^2} \end{bmatrix}$$

$$A_{sep} = \begin{bmatrix} \dfrac{D^{eff}_{e,s,1}}{\xi_s(\Delta x^s_{e,1})^2} & \dfrac{-2D^{eff}_{e,s,1}}{\xi_s(\Delta x^s_{e,1})^2} & \dfrac{D^{eff}_{e,s,1}}{\xi_s(\Delta x^s_{e,1})^2} & 0 & \vdots & \cdots & 0 \\ 0 & \dfrac{D^{eff}_{e,s,1}}{\xi_s(\Delta x^s_{e,i})^2} & \dfrac{-2D^{eff}_{e,s,2}}{\xi_s(\Delta x^s_{e,i})^2} & \dfrac{D^{eff}_{e,s,3}}{\xi_s(\Delta x^s_{e,i})^2} & 0 & \cdots & \vdots \\ \vdots & 0 & \ddots & \ddots & \ddots & 0 & \vdots \\ 0 & 0 & \ddots & \ddots & \ddots & 0 & 0 \\ 0 & \cdots & \cdots & 0 & \dfrac{D^{eff}_{e,s,N-1}}{\xi_s(\Delta x^s_{e,N-1})^2} & \dfrac{-2D^{eff}_{e,s,N-1}}{\xi_s(\Delta x^s_{e,N-1})^2} & \dfrac{D^{eff}_{e,s,N-1}}{\xi_s(\Delta x^s_{e,N-1})^2} \end{bmatrix}$$

$$A_{pos} = \begin{bmatrix} \dfrac{D^{eff}_{e,p,1}}{\xi_p(\Delta x^p_{e,1})^2} & \dfrac{-2D^{eff}_{e,p,1}}{\xi_p(\Delta x^p_{e,2})^2} & \dfrac{D^{eff}_{e,p,1}}{\xi_p(\Delta x^p_{e,3})^2} & \vdots & \vdots \\ 0 & \dfrac{D^{eff}_{e,p,i}}{\xi_p(\Delta x^p_{e,i})^2} & \dfrac{-2D^{eff}_{e,p,i}}{\xi_p(\Delta x^p_{e,i})^2} & \dfrac{D^{eff}_{e,p,i}}{\xi_p(\Delta x^p_{e,i})^2} & \vdots \\ \ddots & 0 & \ddots & \ddots & \ddots \\ 0 & 0 & \ddots & \dfrac{D^{eff}_{e,p,N-1}}{\xi_p(\Delta x^p_{e,N-1})^2} & \dfrac{-D^{eff}_{e,p,N-1}}{\xi_p(\Delta x^p_{e,N-1})^2} \end{bmatrix}$$

$$B = \left[\frac{\left(1-t_f^+\right)}{\xi_n FL_n A} \quad \cdots \quad \frac{\left(1-t_f^+\right)}{\xi_n FL_n A} \quad 0 \quad \cdots \quad 0 \quad \frac{\left(1-t_f^+\right)}{\xi_p FL_p A} \quad \cdots \quad \frac{\left(1-t_f^+\right)}{\xi_p FL_p A}\right]^{\mathrm{T}} \qquad (61)$$

Consequently, electrolyte-phase concentration distribution is computed by solving these ODEs. The boundary concentrations were computed based on boundary condition given in Equation (3), (7), and (8).

3.3 FDM Non-Uniform Grid Size Scheme

FDM non-uniform (uneven) grid size scheme was developed to achieve the model reduction objective of this work. The concentration gradient within each of the region in the battery varies across the region. The gradient is usually steeper at the boundary point due to the applied transfer current through the boundary conditions and smoother for point further away from the boundary. Hence, more discretization points are required at the boundaries to capture the dynamics accurately, and less discretization points are required to capture the dynamics for points further away from the boundary for both solid and electrolyte phase concentration distribution. The unevenly discretized nodes will be determined optimally using a particle swarm optimization which will be discuss in chapter 4. Numerical approximation to the derivatives for this uneven discretized FDM is presented below.

$$f(x_{i+1}) = f(x_i) + \Delta x_i f'(x_i) + \frac{(\Delta x_i)^2}{2!} f''(x_i) + \frac{(\Delta x_i)^3}{3!} f'''(x_i) + HOT \qquad (62)$$

$$f(x_{i-1}) = f(x_i) - \Delta x_{i-1} f'(x_i) + \frac{(\Delta x_{i-1})^2}{2!} f''(x_i) - \frac{(\Delta x_{i-1})^3}{3!} f'''(x_i) + HOT \qquad (63)$$

Simplification of Equation (62) and (63) gives the expression for f'' as,

$$f''(x_i) = \frac{2}{\Delta x_{i-1}(\Delta x_{i-1}+\Delta x_i)\Delta x_i}\left[\Delta x_i f(x_{i-1}) - (\Delta x_{i-1} + \Delta x_i)f(x_i) + \Delta x_{i-1} f(x_{i+1})\right] \qquad (64)$$

3.3.1 Solid-Phase Concentration Solution

The PDEs governing the concentration distribution in the solid-phase across the particle radius is solved through the FDM with uneven discretization scheme by diving the particle radius into N-1 numbers of grids based on the optimal node points generated by the optimization scheme as shown in Figure 18.

$$\Delta r = \frac{R_S}{N} \tag{65}$$

where R_S is the particle radius, N is the total number of evenly discretized nodes which is used as a reference for the uneven discretized scheme. N_{un} is the number of uneven discretized nodes. The particle unevenly discretized radius, r_i is computed based on the current node location to the particle core.
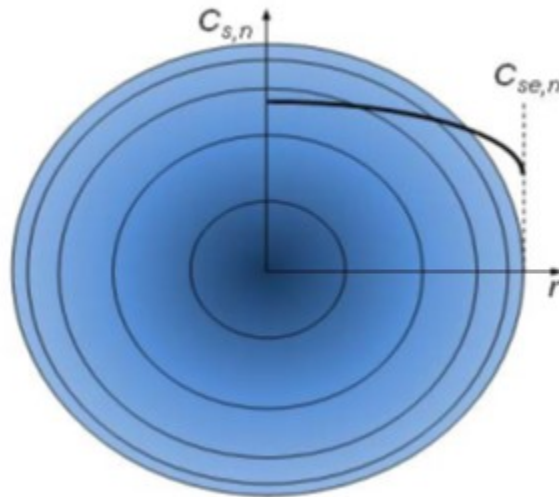
Figure 18: Unevenly Discretized Particle Radius [22]

$$\mathbf{r} = [r_1 \ r_2 \ r_3 \ \dots \ r_{N-2} \ r_{N-1} \ r_N]^{\mathrm{T}}$$

$$\Delta r_{un} = \Delta r(r_{i+1} - r_i) \tag{66}$$

From the state-space representation approach, Equation (1) can be represented as;

$$\dot{C}_s = A_{us}C_s + B_{us}I$$

$$C_s = [C_{s,1}\ C_{s,2}\ C_{s,3}\ldots C_{s,N-2}\ C_{s,N-1}]^T \tag{67}$$

where A_{us} is a constant tri-diagonal matrix computed from Equation (60) and B_{us} is the

column matrix corresponding to the boundary conditions.

$$\frac{\partial C_{s,i}}{\partial t} = \frac{2D_{s,n}}{r_i \Delta r_{i-1}(\Delta r_i + \Delta r_{i-1})\Delta r_i} [(r_i \Delta r_i - \Delta r_i^2)C_{s,i-1} - (r_i(\Delta r_{i-1} + \Delta r_i) + \Delta r_{i-1}^2 - \Delta r_i^2)C_{s,i} + (r_i \Delta r_{i-1} - \Delta r_{i-1}^2)C_{s,i+1}] \tag{68}$$

Applying the boundary conditions at r=0 and r=R_s to Equation (68) gives the boundary point

concentration distribution expressed as,

From the boundary conditions, $\frac{\partial C_s}{\partial r}\big|_{r=0} = \frac{C_{s,1}-C_{s,0}}{\Delta r_1} = 0$; hence $C_{s,0} = C_{s,1}$, Equation (68)

is simplified as expressed below,

$$\frac{\partial C_{s,1}}{\partial t} = \frac{2D_{s,n}}{r_2 \Delta r_1(\Delta r_2 + \Delta r_1)\Delta r_2} [-(r_2 \Delta r_1 - \Delta r_1^2)C_{s,1} + (r_2 \Delta r_1 - \Delta r_1^2)C_{s,2}]. \tag{69}$$

At r=R_s, $-D_s \frac{\partial C_s}{\partial r}\big|_{r=R_s} = \frac{J_{Li}}{a_s F}$ where J_{Li} is as expressed in Equation (15a) and (15b).

$$-\frac{\partial C_s}{\partial r}\big|_{r=R_s} = \frac{C_{S,N}-C_{S,N-1}}{\Delta r_{N-1}} = -\frac{I}{D_s a_s F A L_n} \tag{70}$$

Expressing the Equation (70) in term of $C_{S,N-1}$ and plugging this into Equation (68) gives;

$$\frac{\partial C_{S,N-1}}{\partial t} = \frac{2D_{s,n}}{r_{N-1}\Delta r_{N-2}(\Delta r_{N-1}+\Delta r_{N-2})\Delta r_{N-1}}\left[(r_{N-1}\Delta r_{N-1} - \Delta r_{N-1}{}^2)\,C_{S,N-2} - (r_{N-1}\Delta r_{N-1} - \right.$$

$$\left.\Delta r_{N-1}{}^2)C_{S,N-1}\right] - \frac{2(r_{N-1}+\Delta r_{N-1})}{r_{N-1}\Delta r_{N-2}(\Delta r_{N-1}+\Delta r_{N-2})\Delta r_{N-1}}\frac{I(t)}{a_s F A L_n} \tag{71}$$

The constant tri-diagonal matrix A_{us} and input matrix B_{us} are expressed as,

$$A_{us} =$$

$$\begin{bmatrix}
-\frac{2D_{s,n}(r_2\Delta r_1-\Delta r_1{}^2)}{r_2\Delta r_1(\Delta r_2+\Delta r_1)\Delta r_2} & \frac{2D_{s,n}(r_2\Delta r_1-\Delta r_1{}^2)}{r_2\Delta r_1(\Delta r_2+\Delta r_1)\Delta r_2} & 0 & \cdots & 0 & 0 \\
\frac{2D_{s,n}(r_i\Delta r_i-\Delta r_i{}^2)}{r_i\Delta r_{i-1}(\Delta r_i+\Delta r_{i-1})\Delta r_i} & \frac{-2D_{s,n}(r_i(\Delta r_{i-1}+\Delta r_i)+\Delta r_{i-1}{}^2-\Delta r_i{}^2)}{r_i\Delta r_{i-1}(\Delta r_i+\Delta r_{i-1})\Delta r_i} & \frac{2D_{s,n}(r_i\Delta r_{i-1}-\Delta r_{i-1}{}^2)}{r_i\Delta r_{i-1}(\Delta r_i+\Delta r_{i-1})\Delta r_i} & 0 & \cdots & 0 \\
0 & \ddots & \ddots & \ddots & 0 & \vdots \\
\vdots & 0 & \ddots & \ddots & \ddots & 0 \\
0 & 0 & \cdots & 0 & \frac{2D_{s,n}(r_{N-1}\Delta r_{N-1}-\Delta r_{N-1}{}^2)}{r_{N-1}\Delta r_{N-2}(\Delta r_{N-1}+\Delta r_{N-2})\Delta r_{N-1}} & -\frac{2D_{s,n}(r_{N-1}\Delta r_{N-1}-\Delta r_{N-1}{}^2)}{r_{N-1}\Delta r_{N-2}(\Delta r_{N-1}+\Delta r_{N-2})\Delta r_{N-1}}
\end{bmatrix}$$

$$B_{us}{}^n = \begin{bmatrix} 0 & \cdots & 0 & -\dfrac{2(r_{N-1}+\Delta r_{N-1})}{r_{N-1}\Delta r_{N-2}(\Delta r_{N-1}+\Delta r_{N-2})\Delta r_{N-1}Fa_s AL_n} \end{bmatrix}^{\mathrm{T}}$$

$$B_{us}{}^p = \begin{bmatrix} 0 & \cdots & 0 & -\dfrac{2(r_{N-1}+\Delta r_{N-1})}{r_{N-1}\Delta r_{N-2}(\Delta r_{N-1}+\Delta r_{N-2})\Delta r_{N-1}Fa_s AL_p} \end{bmatrix}^{\mathrm{T}} \tag{72}$$

the matrix A_{us} has the same structure for both electrodes but different D_s. Simplifying Equation (67) gives

$$\frac{C_{s,i+1}-C_{s,i}}{\Delta t} = A_{us}C_{s,i} + B_{us}I$$

$$C_{s,i+1} = (1 + \Delta t A_{us})\,C_{s,i} + \Delta t B_{us}I \tag{73}$$

The solid-phase concentration distribution is computed using Equation (73), as a function of time and position in a similar manner to FDM evenly discretized solution approach.

3.3.2 Electrolyte-Phase Concentration Solution

For electrolyte-phase concentration dynamics, the uneven discretized FDM scheme is expressed as,

Negative Electrode Region: $0 \le x_n \le L_n$

$$\frac{\partial C_{e,i}^n}{\partial t} = \frac{2D_{e,n,i}^{eff}}{\xi_n \Delta x_{i-1}(\Delta x_i + \Delta x_{i-1})\Delta x_i} \left[\Delta x_i C_{e,i-1}^n - (\Delta x_i + \Delta x_{i-1})C_{e,i}^n + \Delta x_{i-1}C_{e,i+1}^n \right] + \frac{\left(1-t_f^+\right)}{\xi_n F L_n A} I(t) \tag{74}$$

Applying a no zero gradient boundary condition at $i{=}1$, $C_{e,1}^n = C_{e,2}^n$, hence,

$$\frac{\partial C_{e,1}^n}{\partial t} = \frac{2D_{e,n,1}^{eff}}{\xi_n \Delta x_1(\Delta x_2 + \Delta x_1)\Delta x_2} \left[-\Delta x_1 C_{e,1}^n + \Delta x_1 C_{e,2}^n \right] + \frac{\left(1-t_f^+\right)}{\xi_n F L_n A} I(t) \tag{75}$$

For the Nth-Node point from the boundary relation,

$$\frac{\partial C_{e,N-1}^n}{\partial t} = \frac{2D_{e,n,N-1}^{eff}}{\xi_n \Delta x_{N-1}(\Delta x_{N-1} + \Delta x_{N-2})\Delta x_{N-2}} \left[\Delta x_{N-1} C_{e,N-2}^n - (\Delta x_{N-1} + \Delta x_{N-2})C_{e,N-1}^n + \Delta x_{N-2}C_{e,N}^n \right] + \frac{\left(1-t_f^+\right)}{\xi_n F L_n A} I(t) \tag{76}$$

Since $D_{e,n}^{eff} \frac{\partial C_{e,n}}{\partial x}|_{x=Ln} = D_{e,s}^{eff} \frac{\partial C_{e,s}}{\partial x}|_{x=Ls}$, $C_{e,N}^n$ can be expressed in terms of $C_{e,N-2}^n, C_{e,N-1}^n, C_{e,2}^s$ and substituted into Equation (76).

Separator Region: $L_n \le x_s \le L_n + L_s$

$$\frac{\partial C_{e,i}^s}{\partial t} = \frac{2D_{e,s,i}^{eff}}{\xi_s \Delta x_{i-1}(\Delta x_i + \Delta x_{i-1})\Delta x_i} \left[\Delta x_i C_{e,i-1}^s - (\Delta x_i + \Delta x_{i-1})C_{e,i}^s + \Delta x_{i-1}C_{e,i+1}^s \right] + \frac{\left(1-t_f^+\right)}{\xi_s F L_s A} I(t) \tag{77}$$

Since at the first node, $C_{e,N}^n = C_{e,1}^s$ and $C_{e,1}^s$ can be derived from the given boundary condition at L_n. Thus,

$$\frac{\partial C_{e,2}^s}{\partial t} = \frac{2D_{e,s,1}^{eff}}{\xi_s \Delta x_1 (\Delta x_2 + \Delta x_1) \Delta x_2} [\Delta x_2 C_{e,N}^n - (\Delta x_2 + \Delta x_1) C_{e,2}^s + \Delta x_2 C_{e,3}^s] \tag{78}$$

For the Nth-Node point from the boundary relation,

$$\frac{\partial C_{e,N-1}^s}{\partial t} = \frac{2D_{e,s,N-1}^{eff}}{\xi_s \Delta x_{N-1} (\Delta x_{N-1} + \Delta x_{N-2}) \Delta x_{N-2}} [\Delta x_{N-1} C_{e,N-2}^s - (\Delta x_{N-1} + \Delta x_{N-2}) C_{e,N-1}^s + \Delta x_{N-2} C_{e,N}^s] \tag{79}$$

From $D_{e,n}^{eff} \frac{\partial C_{e,n}}{\partial x}|_{x=Ln} = D_{e,s}^{eff} \frac{\partial C_{e,s}}{\partial x}|_{x=Ls}$, $C_{e,N}^s$ can be expressed in terms of $C_{e,N-2}^s, C_{e,N-1}^s, C_{e,2}^p$ and substituted into Equation (79).

Positive Electrode Region: $L_n + L_s \le x_p \le L_n + L_s + L_p$

$$\frac{\partial C_{e,i}^p}{\partial t} = \frac{2D_{e,p,i}^{eff}}{\xi_p \Delta x_{i-1} (\Delta x_i + \Delta x_{i-1}) \Delta x_i} [\Delta x_i C_{e,i-1}^p - (\Delta x_i + \Delta x_{i-1}) C_{e,i}^p + \Delta x_{i-1} C_{e,i+1}^p] + \frac{(1-t_f^+)}{\xi_p F L_p A} I(t) \tag{80}$$

Since at the first node, $C_{e,N}^s = C_{e,1}^p$ and $C_{e,1}^p$ can be derived from the given boundary condition at $L_n + L_s$ thus,

$$\frac{\partial C_{e,1}^p}{\partial t} = \frac{2D_{e,p,1}^{eff}}{\xi_p \Delta x_1 (\Delta x_2 + \Delta x_1) \Delta x_2} [\Delta x_2 C_{e,N}^s - (\Delta x_2 + \Delta x_1) C_{e,2}^p + \Delta x_1 C_{e,3}^p] + \frac{(1-t_f^+)}{\xi_p F L_p A} I(t) \tag{81}$$

The last node dynamics can be formulated using the boundary relation, and subsisting the zero gradient boundary condition and expressed as,

$$\frac{\partial C_{e,N-1}^p}{\partial t} = \frac{2D_{e,p,N-1}^{eff}}{\xi_p \Delta x_{N-1}(\Delta x_{N-1}+\Delta x_{N-2})\Delta x_{N-2}} \left[\Delta x_{N-1} C_{e,N-2}^p - \Delta x_{N-1} C_{e,N-1}^p \right] + \frac{(1-t_f^+)}{\xi_p FL_p A} I(t) \quad (82)$$

Therefore, the constant tri-diagonal matrix A_{ue} and input matrix B_{ue} are formulated as below;

$$A_{ue} = \begin{bmatrix} A_n & 0 & 0 \\ 0 & A_s & 0 \\ 0 & 0 & A_p \end{bmatrix}$$

where matrix A_n, A_s and A_p corresponds to the coefficient matrix for the negative electrode,

separator, and positive electrode as expressed below;

$$A_n =$$

$$\begin{bmatrix}
-\frac{2D_{e,n,1}^{eff}\Delta x_1}{\xi_n \Delta x_1(\Delta x_2+\Delta x_1)\Delta x_2} & \frac{2D_{e,n,1}^{eff}\Delta x_1}{\xi_n \Delta x_1(\Delta x_2+\Delta x_1)\Delta x_2} & 0 & \cdots & 0 & 0 \\
\frac{2D_{e,n,i}^{eff}\Delta x_i}{\xi_n \Delta x_{i-1}(\Delta x_i+\Delta x_{i-1})\Delta x_i} & \frac{-2D_{e,n,i}^{eff}(\Delta x_i+\Delta x_{i-1})}{\xi_n \Delta x_{i-1}(\Delta x_i+\Delta x_{i-1})\Delta x_i} & \frac{2D_{e,n,i}^{eff}\Delta x_{i-1}}{\xi_n \Delta x_{i-1}(\Delta x_i+\Delta x_{i-1})\Delta x_i} & 0 & \cdots & 0 \\
0 & \ddots & \ddots & \ddots & 0 & \vdots \\
\vdots & 0 & \ddots & \ddots & \ddots & 0 \\
0 & 0 & \cdots & \frac{2D_{e,n,N-1}^{eff}\Delta x_{N-1}}{\xi_n \Delta x_{N-1}(\Delta x_{N-1}+\Delta x_{N-2})\Delta x_{N-2}} & \frac{-2D_{e,n,N-1}^{eff}(\Delta x_{N-1}+\Delta x_{N-2})}{\xi_n \Delta x_{N-1}(\Delta x_{N-1}+\Delta x_{N-2})\Delta x_{N-2}} & \frac{2D_{e,n,N-1}^{eff}\Delta x_{N-2}}{\xi_n \Delta x_{N-1}(\Delta x_{N-1}+\Delta x_{N-2})\Delta x_{N-2}}
\end{bmatrix}$$

$$A_s =$$

$$\begin{bmatrix}
0 & 0 & \cdots & \cdots & \cdots & \cdots \\
\frac{2D_{e,s,1}^{eff}\Delta x_2}{\xi_s \Delta x_1(\Delta x_2+\Delta x_1)\Delta x_2} & \frac{-2D_{e,s,1}^{eff}(\Delta x_2+\Delta x_1)}{\xi_s \Delta x_1(\Delta x_2+\Delta x_1)\Delta x_2} & \frac{2D_{e,s,1}^{eff}\Delta x_1}{\xi_s \Delta x_1(\Delta x_2+\Delta x_1)\Delta x_2} & 0 & 0 & 0 \\
\cdots & \frac{2D_{e,s,i}^{eff}\Delta x_i}{\xi_s \Delta x_{i-1}(\Delta x_i+\Delta x_{i-1})\Delta x_i} & \frac{-2D_{e,s,i}^{eff}(\Delta x_i+\Delta x_{i-1})}{\xi_s \Delta x_{i-1}(\Delta x_i+\Delta x_{i-1})\Delta x_i} & \frac{2D_{e,s,i}^{eff}\Delta x_{i-1}}{\xi_s \Delta x_{i-1}(\Delta x_i+\Delta x_{i-1})\Delta x_i} & 0 & 0 \\
\cdots & \cdots & 0 & \ddots & \ddots & 0 \\
\ddots & \ddots & 0 & \frac{2D_{e,s,N-1}^{eff}\Delta x_{N-1}}{\xi_s \Delta x_{N-1}(\Delta x_{N-1}+\Delta x_{N-2})\Delta x_{N-2}} & \frac{-2D_{e,s,N-1}^{eff}(\Delta x_{N-1}+\Delta x_{N-2})}{\xi_s \Delta x_{N-1}(\Delta x_{N-1}+\Delta x_{N-2})\Delta x_{N-2}} & \frac{2D_{e,s,N-1}^{eff}\Delta x_{N-2}}{\xi_s \Delta x_{N-1}(\Delta x_{N-1}+\Delta x_{N-2})\Delta x_{N-2}}
\end{bmatrix}$$

$$A_p = \begin{bmatrix}
0 & 0 & 0 & 0 & 0 \\
\frac{2D_{e,p,1}^{eff}\Delta x_2}{\xi_p \Delta x_1(\Delta x_2+\Delta x_1)\Delta x_2} & \frac{-2D_{e,p,1}^{eff}(\Delta x_2+\Delta x_1)}{\xi_p \Delta x_1(\Delta x_2+\Delta x_1)\Delta x_2} & \frac{2D_{e,p,1}^{eff}\Delta x_1}{\xi_p \Delta x_1(\Delta x_2+\Delta x_1)\Delta x_2} & 0 & 0 \\
\cdots & \frac{2D_{e,p,i}^{eff}\Delta x_i}{\xi_p \Delta x_{i-1}(\Delta x_i+\Delta x_{i-1})\Delta x_i} & \frac{-2D_{e,p,i}^{eff}(\Delta x_i+\Delta x_{i-1})}{\xi_p \Delta x_{i-1}(\Delta x_i+\Delta x_{i-1})\Delta x_i} & \frac{2D_{e,p,i}^{eff}\Delta x_{i-1}}{\xi_p \Delta x_{i-1}(\Delta x_i+\Delta x_{i-1})\Delta x_i} & 0 \\
\cdots & 0 & \ddots & \ddots & \ddots \\
\ddots & \ddots & 0 & \frac{2D_{e,p,N-1}^{eff}\Delta x_{N-1}}{\xi_p \Delta x_{N-1}(\Delta x_{N-1}+\Delta x_{N-2})\Delta x_{N-2}} & \frac{-2D_{e,p,N-1}^{eff}\Delta x_{N-1}}{\xi_p \Delta x_{N-1}(\Delta x_{N-1}+\Delta x_{N-2})\Delta x_{N-2}}
\end{bmatrix}$$

$$B_{ue} = \left[\frac{(1-t_f^+)}{\xi_n FL_n A} \quad \cdots \quad \frac{(1-t_f^+)}{\xi_n FL_n A} \quad 0 \quad \cdots \quad 0 \quad \frac{(1-t_f^+)}{\xi_p FL_p A} \quad \cdots \quad \frac{(1-t_f^+)}{\xi_p FL_p A} \right]^T$$

The electrolyte-phase concentration distribution is computed by solving these ODEs and the boundary concentrations were computed based on boundary condition given in Equation (9), (10) and (11). The solid-phase and electrolyte-phase concentration distribution are computed as a function of locations and time. Based on the concentrations' computation, the kinetic overpotential, equilibrium potential and overpotential due to both diffusion and migration can be computed. The battery terminal voltage as expressed in Equation (33) is computed based on the solution of these ODEs derived. The battery model parameters used for this work is given in Table 1.

Table 1: Model parameters for a 52.9Ah lithium-ion battery simulated in this work [30].

Parameters	Negative electrode	Separator	Positive electrode
Thickness (L) in μm	100	25	100
Particle Radius (Rs) in μm	10	-	10
Number of even discretization	50	10	50
Active particle volume fraction	0.6	-	0.5
Electrolyte phase volume fraction	0.3	1	0.3
Max solid phase conc. In (mol/m^3)	24984	-	51219
Average electrolyte concentration (Ce) in (mol/m^3)	1000	1000	1000
Bruggeman Constant	1.5	1.5	1.5
Reaction Rate (k)	1e-5	-	3e-7
Li-ion diffusion coefficient in solid phase (Ds) in (m^2/s)	3.9e-14	-	1e-13
Li-ion diffusion coefficient in electrolyte phase (De) in (m^2/s)	2.79e-10	2.79e-10	2.79e-10
Resistance I at electrode-current collector surface	1e-3		0
Transference number ($t+$)	0.5		0.5
Electrode plate area (A) in (m^2)	1		1
Universal gas constant I in ($J/mol/K$)	8.3145		
Faraday's constant (F) in (C/mol)	96485.33		
Ambient Temperature (T) in K	298.15		

Chapter 4: Optimal Node Selection

4.1   Particle Swarm Optimization

Particle swarm optimization (PSO) is a population based stochastic search technique developed by Kennedy and Eberhartin in 1995 [39]. The concept of PSO was inspired by social behavior of bird flocking or fish schooling. This stochastic optimization search technique was developed based on two important concepts:

- Understanding of animals (birds and fish) tendency to swarm towards a particular direction in search for food and comfort

- The knowledge of evolutionary computation field such as genetic algorithms.

PSO is an effective optimization technique to search for global optimization solution within the search space. According to [40], a simple illustration for understanding the operation of PSO is that of a group of birds randomly searching food in an area. If there is only one piece of food in the area being searched. Assuming all the birds do not know where the food is, but they know how far the food is in each iteration. The effective strategy to search for the food is to follow the bird nearest to the food and update other birds position accordingly. Each bird referred to a particle, here a particle refers to a point in the design space that changes its position from one iteration to another based on velocity updates and the best solution. Each particle is a possible solution to the optimization problem.

Hence, Particle Swarm Optimization is a numerical search algorithm which is used to find global parameters that minimize a given objective, or fitness function. The objective function can be non-linear and can be subject to any number of linear and non-linear constraints [40]. The objective function is evaluated in each iteration based on the present position of each particles (solutions) and the particle which gives the minimal cost become the global best. Each particles position is updated based on a pre-determined velocity which draws the particle towards the global particle. Over the years, PSO has gained significant popularity because of its simple structure and high performance. Many publications, such as [41-43], demonstrate the merit of PSO in a diverse range of applications [40].
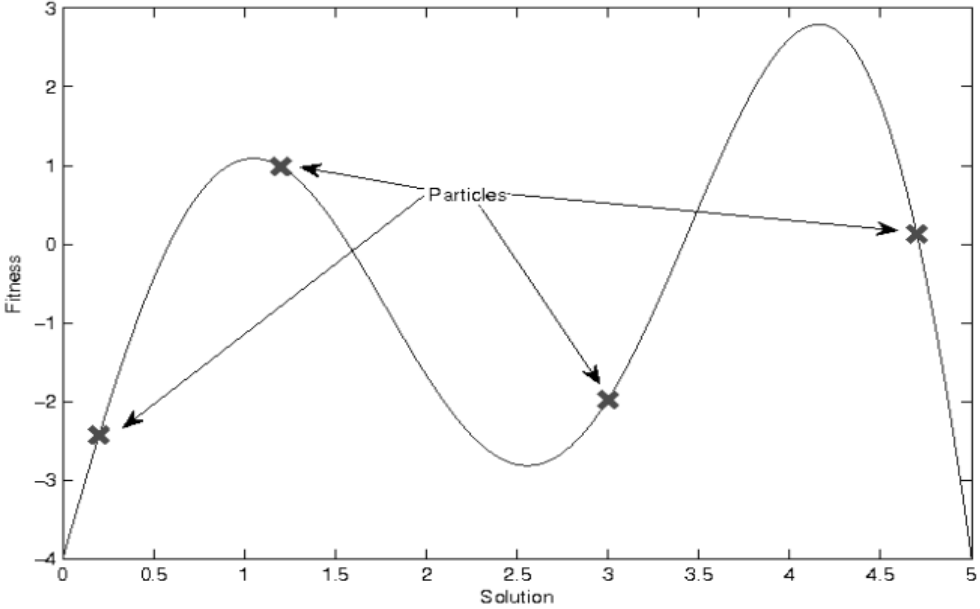
Figure 19: Fitness function showing different particles [46]

PSO is similar to other evolutionary computation techniques like Genetic Algorithm (GA) in the sense that they are both population-based search approaches. They both depend on information sharing among their population members to enhance their search processes using a combination

of deterministic and probabilistic rules [40]. Although PSO have some similarities with evolutionary computation techniques like generic algorithm, the advantages of PSO as a global optimizer over other evolutionary-based optimization techniques include;

- Easy implementation because it does not have genetic operators such as crossover and mutation

- Less turning parameters

- Low computational cost and better computational efficiency compared to other EC techniques specifically GA [45].

4.2 PSO Internal Structure

PSO is structured in such a way that the entire optimization technique can be summarized into three main steps:

- Evaluating objective function based on each particle

- Updating personal best (pbest) and global best (gbest) based on the objective function evaluation.

- Updating velocity and position of each particle based on pbest and gbest.

PSO involves the determination of the best particle which minimizes the objective function among all possible particles. The search techniques start with an initialization procedure for N-possible solution (particles) set with which the objective function is evaluated and the particle that gives the minimal cost is taken as the global best (gbest) solution and each particle still retains their position stored as individual personal best (pbest). The initialization of particle is done in such a way that, the particles are randomly distributed through the entire design space for PSO to explore the entire design space in finding the best particle. Based on the stored pbest and gbest, the required

velocity for individual particle to converge towards the gbest with reference to pbest is computed and this is used in updating the position of each particle. The objective function is re-evaluated based on the new position of the particles, to ensure the new solution minimizes the objective function otherwise the new position is ignored and the previous pbest is still retain in the memory of the optimizer. These optimization procedures are repeated until a set criterion is satisfied. The change in direction and velocity of each individual particle is the effect of cognitive, social and stochastic influences. The common goal of all group members is to find the most favorable location within a specified search space [40] as shown in Figure 20. The particle swarm optimization procedure for solving any minimization problems is formulated as:

$$v_i^{k+1} = w^k v_i^k + r_1[\Upsilon_1(P_i - x_i^k)] + r_2[\Upsilon_2(G_i - x_i^k)] \tag{83}$$

$$x_i^{k+1} = x_i^k + v_i^{k+1} \tag{84}$$
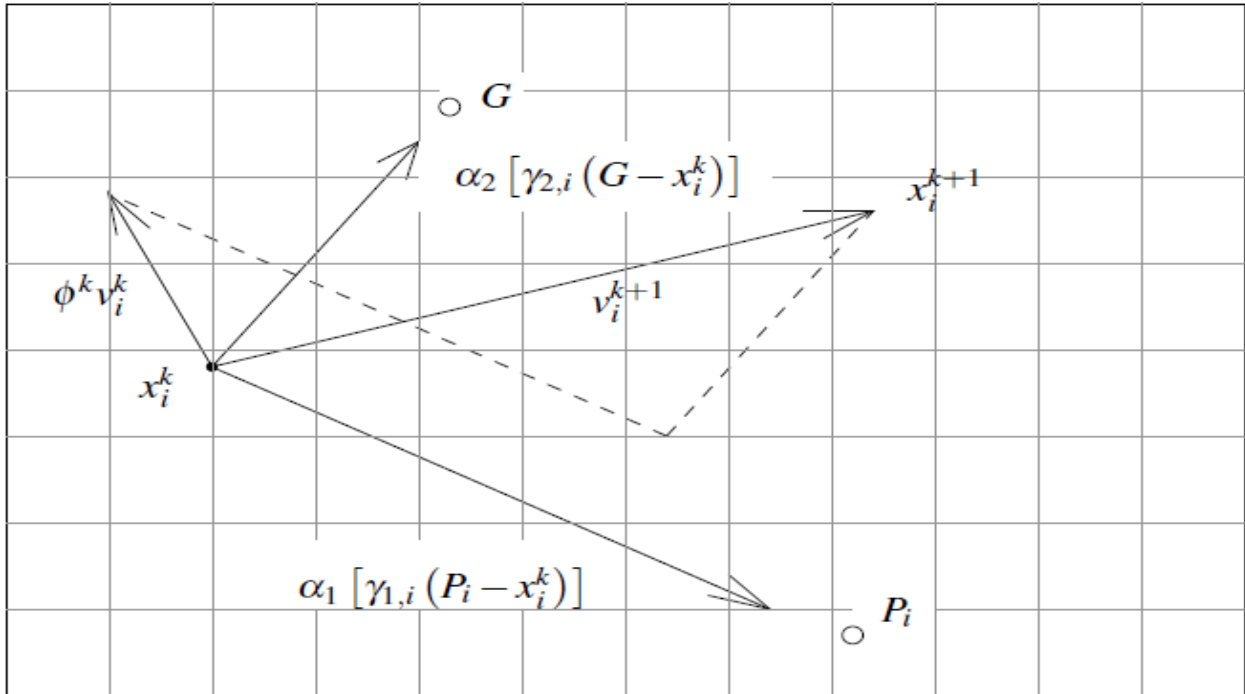
Figure 20: Graphical interpretation of the PSO algorithm [46]

where subscript $i=[1,2,3...N]$ is the number of possible solutions in the swarm, and $k=[1,2,3...N_{it}]$ where k is the number of iterations. Thus, v_i^k and x_i^k are the present velocity and position of the *i-th* particle during *k-th* iteration count, v_i^{k+1} and x_i^{k+1} are the new velocity and position of the *i-th* particle during k+1-th iteration count respectively. Likewise, r_1 and r_2 are randomly generated numbers between 0 and 1, $Υ_1$, $and$$Υ_2$ are acceleration factor which are typically assumed to be 2 respectively. P_i and G_i are the present pbest and gbest respectively. The entire second term of Equation (83) is defined as the cognitive term which ensure the particles explore the entire design space while the third term of Equation (83) is the social term which ensure that the particles exploit the entire design space.

The parameter w^k is the inertia weight which is imposed on the velocity to ensure certain momentum of the particles, and it is a function of iteration counts expressed as [42]:

$$w^k = w_{min} + \frac{(w_{max} - w_{min})(N_{it} - k)}{N_{it}} \tag{85}$$

w_{min}= constant minimum inertia weight

w_{max}= constant maximum inertia weight

N_{it}= maximum total number of iterations and k= present iteration count

Lower value of inertia weight increases the convergent rate of the PSO algorithm while higher inertia weight encourages exploring the design space in finding the optimal solution [46].

4.3 PSO Algorithm Formulation for Optimal Node Selections

The PSO is employed for determining the global optimal nodes that serve as an input parameter to the constructed FDM uneven discretized model. Based on the structure of the general PSO, the algorithm will search for optimal nodes for both electrolyte-phase and solid-phase concentration prediction and the PSO parameters applied are also declared.

4.3.1 Solid-Phase Minimization Problem Formulation

The objective function for solid-phase concentration minimization problem is constructed to include the standard deviation of the error between surface and bulk concentrations predicted by the unevenly discretized model (proposed model) and the evenly discretized model (reference model). The objective function is formulated in this manner because of the significance of solid-phase surface concentrations in the cell terminal voltage computation. The surface concentration directly influences the cell terminal voltage, thus determination of the optimal unevenly nodes which will ensure close predictions between the reference model and the proposed model is paramount. Likewise, the contribution of standard deviation of solid-phase bulk concentration error is included in the objective function to ensure high fidelity of the proposed model. The battery state of charge is bulk concentration dependent.

Hence, the objective function is constructed based on these two important battery parameters (cell voltage and SoC) and the PSO is applied to minimize the formulated objective function with a non-negative constraint.

The optimization formulation is;

$$\min_{r} F(r) = \alpha_1 J_1 + \alpha_2 J_2 \tag{86}$$

Subject to $$0 < r_k < R_s$$

where α_1 and α_2 are the weighting factor used in tuning the contribution of both standard error due to solid-phase surface concentration (J_1), and solid-phase bulk concentration (J_2) respectively. This is done to minimize the offset and magnitude of error between the unevenly discretized model prediction and evenly discretized model prediction. The standard error J_1 and J_2 are expressed as,

$$J_1 = \sqrt{\frac{\sum_{k=1}^{N}(C_{s,k}^{surf,ref} - C_{s,k}^{surf,red})^2}{N}} \tag{87}$$

$$J_2 = \sqrt{\frac{\sum_{k=1}^{N}(C_{s,k}^{bulk,ref} - C_{s,k}^{bulk,red})^2}{N}} \tag{88}$$

where N is the total number of solution set which is a function of discharge/charge operation duration, t, $C_{s,k}^{surf,ref}$ and $C_{s,k}^{surf,red}$ are the solid-phase surface concentration predicted by the reference model and reduced model respectively. The variables $C_{s,k}^{bulk,ref}$ and $C_{s,k}^{bulk,ref}$ are the solid-phase bulk concentration predicted by the reference model and proposed model respectively which are both computed based on the average bulk concentration expression given in [21].

$$C_s^{bulk} = \frac{3}{R^3} \int_0^{R_s} R^2 C_s(r,t) dr \tag{89}$$

A sub-optimization problem is formulated to determine the optimal α_1 and α_2 , where $\alpha_1 + \alpha_2 = 1$. Thus, both weighting factors range from 0 to 1, with an indirect proportional relationship between them. The optimal weighting factor was determined to be $\alpha_1 = 0.8$ and $\alpha_2 = 0.2$ and this will be discussed further in Chapter 5. Because of the slow dynamic nature at the negative electrode, in comparison to that in the positive electrode, the optimal nodal solution for the negative electrode is sufficient to capture the concentration distribution in the positive electrode. Hence, the optimization operations were only performed for the negative electrode and the optimal solutions applied for the positive electrode concentration distribution predictions.

4.3.2 Electrolyte-Phase Minimization Problem Formulation

The importance of electrolyte-phase concentration distribution in computing the overpotential due to electrolyte-transport across the cell length which causes cell voltage drop, demonstrate the impact of any possible error between the predictions of the reference model and the proposed model on the cell voltage prediction accuracy for our optimal model reduction purpose. Consequently, the optimization objective function is formulated to minimize the magnitude of the concentration error, between the reference model and proposed model, by determining the global optimal nodes using the PSO for the proposed model prediction.

Although the electrolyte-phase Li-ion concertation distribution occurred across the three regions of the negative electrode, separator and positive electrode, only the extreme concentration of both electrodes is needed in the diffusion overpotential computations. Hence, the objective function was formulated to minimize the concentration predictions error of these two important nodes as they both impact the performance of the proposed model for voltage prediction. The optimization problem is formulated is expressed as,

$$\min_{x} F(x) = J_e \tag{90}$$

Subject to $\qquad\qquad\qquad\qquad 0 < x_k < \mathrm{L}$

where $\qquad\qquad J_e = \sqrt{\dfrac{\sum_{k=1}^{N}(C_{e,k}^{x_0,ref}-C_{e,k}^{x_0,red})^2}{N} + \dfrac{\sum_{k=1}^{N}(C_{e,k}^{x_L,ref}-C_{e,k}^{x_L,red})^2}{N}} \tag{91}$

The parameter L is the length of the cell, the first term of the objective function is the standard deviation of the error between the electrolyte-phase concentration of the reference $\left(C_{e,k}^{x_0,ref}\right)$ and proposed model at the extreme node of negative electrode $\left(C_{e,k}^{x_0,red}\right)$ and the second term of the

objective function is the standard deviation of the error between the electrolyte-phase concentration of the reference $(C_{e,k}^{x_L,ref})$ and proposed model at the extreme node of positive electrode $(C_{e,k}^{x_L,red})$ over the entire discharge/charge duration.

4.3.3 PSO Parameters Setting

The following parameters are applied for the PSO algorithm simulation both for solid-phase and electrolyte-phase optimization problem.

N=100   Number of particles/solutions

M=Varies   Number of variables in each particle

N_{it} =1000   Number of Iteration

W_{min} = 0.4   Minimum Inertia Weight

W_{max} = 0.9   Minimum Inertia Weight

$\Upsilon_1 = \Upsilon_2 = 2$ Acceleration Coefficients

PSO algorithm was set up in a way for optimal nodes determination with certain constrains on the velocity update, to ensure that the position update does not violate the nodal boundary conditions, by setting a velocity range between maximum velocity and minimum velocity. With respect to the boundary conditions for each of the three regions, at least two node points are needed excluding the boundaries to successfully predict the electrolyte-phase concentration distribution, therefore a constraint was set based on the structural requirement for the minimum number of variables for the minimum number of variable choices. The minimum number of variables is 6variable comprising of 2 variables from each of the three regions and the optimization operation was run

for different number of variables to determine the optimal number of discretization nodes and

investigate the influence of increase in number of variables on the proposed model performance.

Chapter 5: Simulation Results and Discussion

This chapter presents the results from the optimal nodes selection problem and the performance of the reduced-order model in term of voltage prediction for each of the three operations:

- Constant Current Discharge Operation

- Pulse Charge/Discharge Operation

- Hybrid Pulse Power Characterization (HPPC) Operation

Furthermore, the comparison of reference model results with the reduced-order model results to validate the capabilities of the proposed model were presented and discussed.

5.1 Constant Current Discharge Operation

A constant current profile is applied to discharge the battery based on its capacity of 1C=52.89A based on the LCO battery parameters presented in [26]. As stated in Chapter four, the optimization problem was formulated both for solid and electrolyte phases to minimize the error between the concentration predictions of the reduced order model and the reference model. The evenly discretized FDM model is employed as a reference to develop a reduced order model based on the unevenly discretized FDM scheme developed in Chapter 3. As stated in Chapter four, the optimization problem was formulated for solid and electrolyte phase, to minimize the error between the concentration predictions from the reduced order model and the reference model.

5.1.1 Solid Phase Optimization Results

The PSO algorithm was run for 1000 iteration counts for solid and electrolyte-phase optimal nodes selection, based on the minimization of the objective functions as stated in Equations (86) and (90). The optimization algorithm was run with initial 100 solutions, with each solution corresponding to a set of possible unevenly discretized nodes which serve as an input to the proposed reduced-order model. Based on the objective function evaluations during each iteration, the optimal solution is determined, stored, and used in updating other solutions set until the global minimizer for the objective function is achieved.

As mentioned in Chapter 4, two objective functions, J_1 and J_2, were considered for the solid particle optimal nodes selection. To determine the optimal weighting factor (α_1 and α_2) used in Equation (86), Pareto's curve was constructed by simply finding the optimal solutions with different values of α_1 and α_2, where $\alpha_1 + \alpha_2 = 1$. The set of weighting factors used are α_1=[1, 0.8, 0.6 0.5, 0.4, 0.2, 0] and α_2=[0,0.2,0.4,0.5,0.6,0.8,1] respectively. The optimal nodes selected by the PSO based on each set of the weighting factors were used in evaluating the objective functions J_1 and J_2 separately and these values were plotted on a Pareto's curve as shown in Figure 21. From the curve, the closest weighting factor set to the asymptote point, which is the point where the line of α_1=1 and α_2=0 solution meet with the line of α_1=0 and α_2=1 solution is the optimal weighting factor according to pareto principle. The optimal weighting factor was found to be $\alpha_1 = 0.8$ and $\alpha_2 = 0.2$.
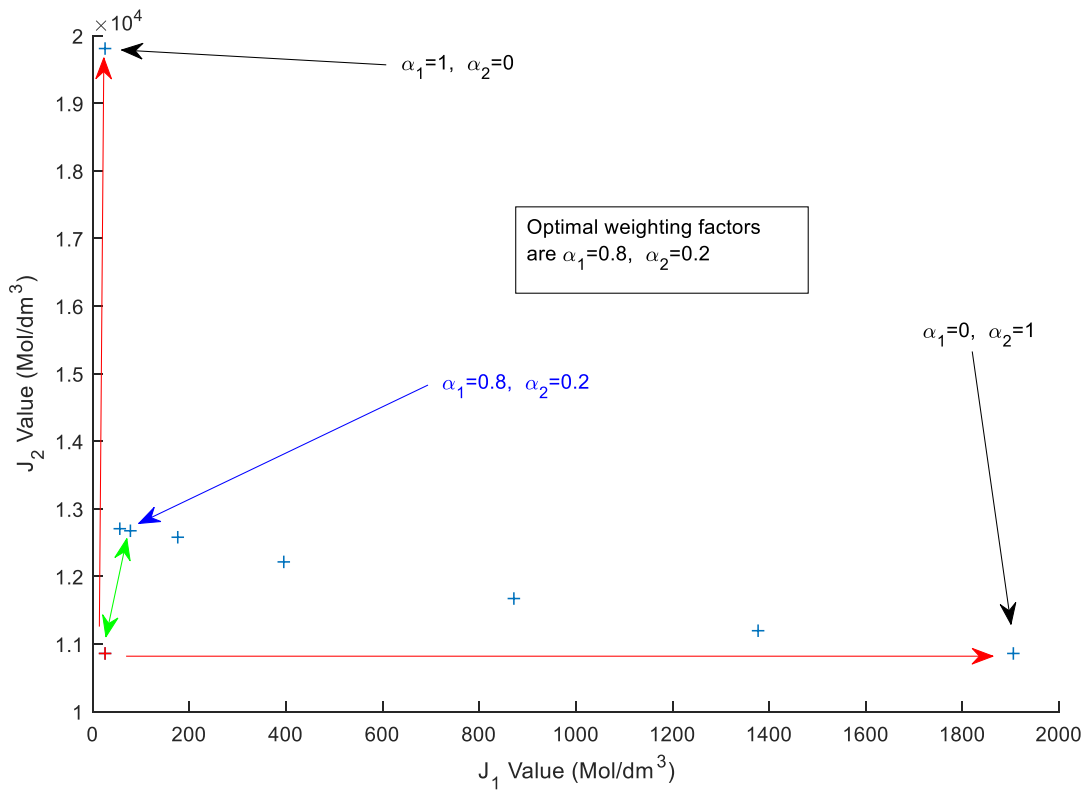
Figure 21: Pareto Curve for Optimal Weighting Factor Determination

Two minimization problems were considered for the solid-phase optimization scheme: the first problem is formulated to minimize J_1 only and the other is based on the contribution of both J_1 and J_2 using the optimal weighting factors.

For the constant current operation, as show in Figure 22(a) and 22(b), the solutions converged after 400 iteration counts, and this demonstrates the capability of the developed PSO to determine the optimal solution for the optimization problem in Equation (86) for both objective functions.

Figure 22: PSO Convergence Profile for Solid-phase Optimization for CC Operation based on (a) J_1 only (b) J_1 and J_2.
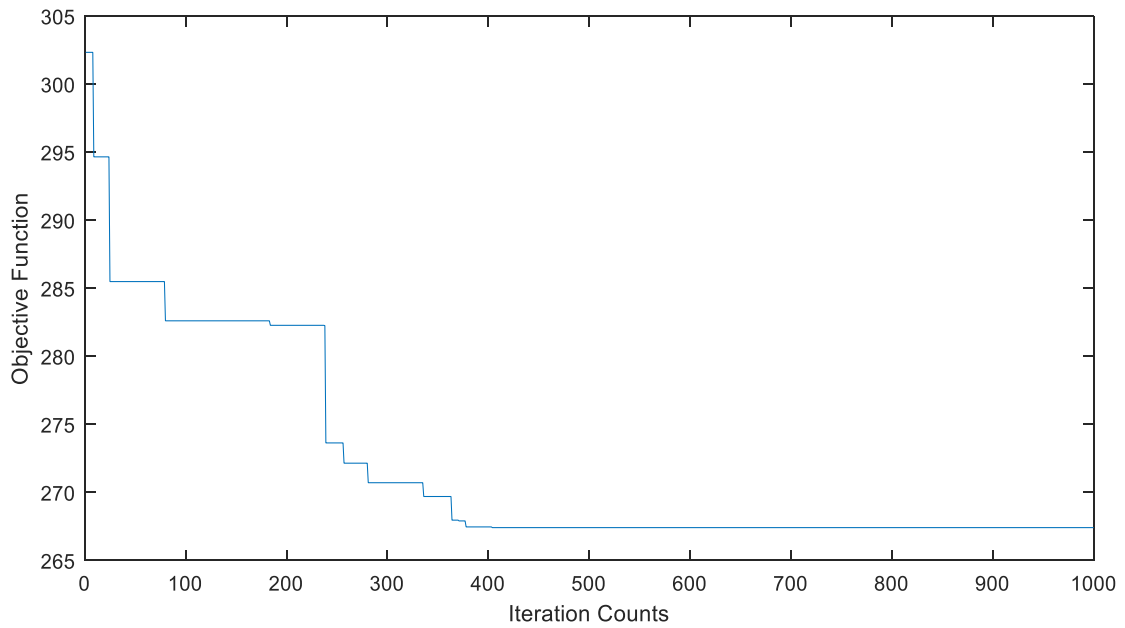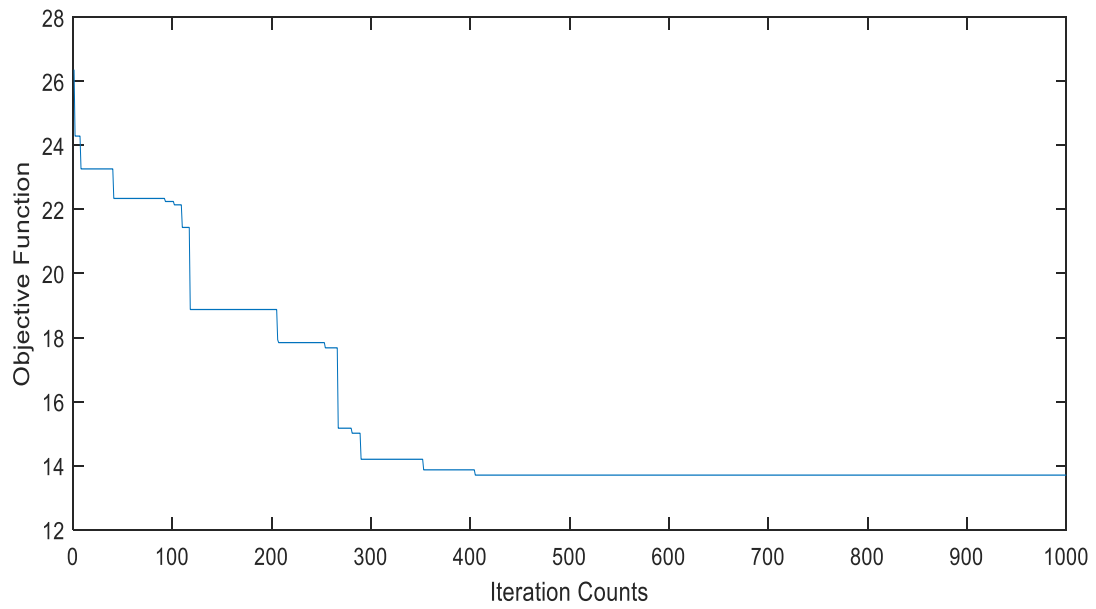
Different number of nodes were considered to investigate the accuracy of the proposed model. As shown in Figure 23a, for the optimization based only on J_1 error minimization, the selected optimal nodes are more closely packed toward the surface of the particle. As the number of discretization

69

nodes increase, the selected nodes spread toward the core of the particle. Although some nodes in the four and five variables scheme does not follow the trend of other optimal solutions, this might be due to the number of selected nodes being not sufficient to capture the concentration dynamics for a constant current operation. In Figure 23b, for the optimization problem with the inclusion of bulk concentration error contribution in the minimization problem, the optimal nodes are spread across the radius of the particle and become more closely packed towards the surface of the particle as the number of selected nodes increases. From Table 2, it can be observed that the magnitude of the objective function reduces as the number of variable increases, this implies an improvement in the accuracy of the proposed model in predicting the solid-phase concentration as the order of the proposed model increases.
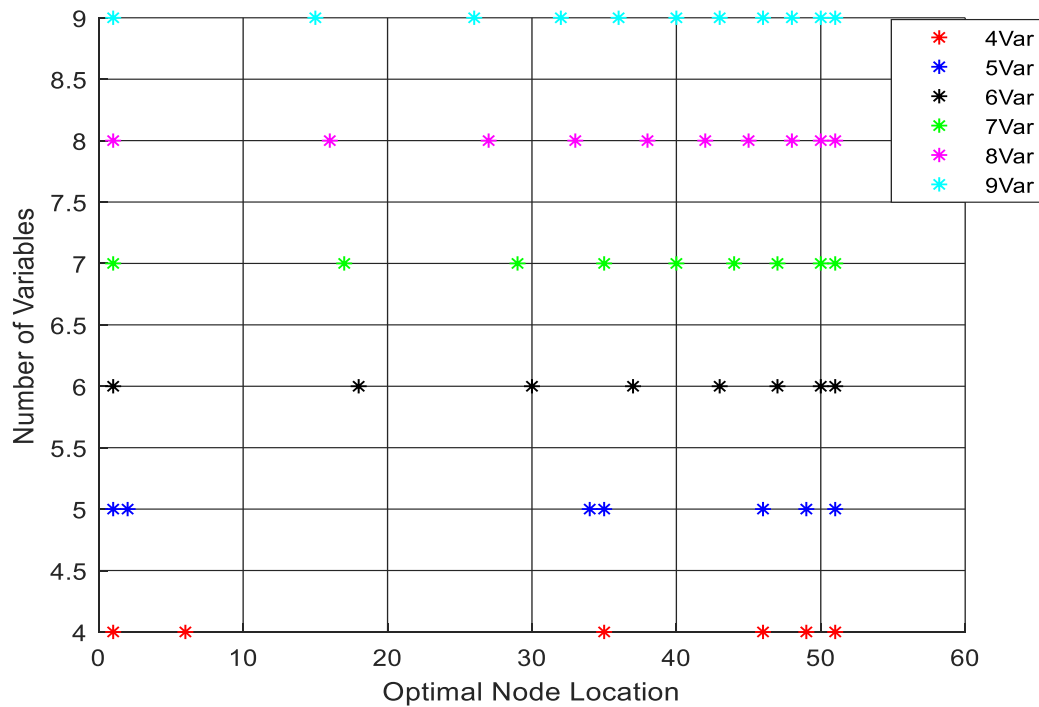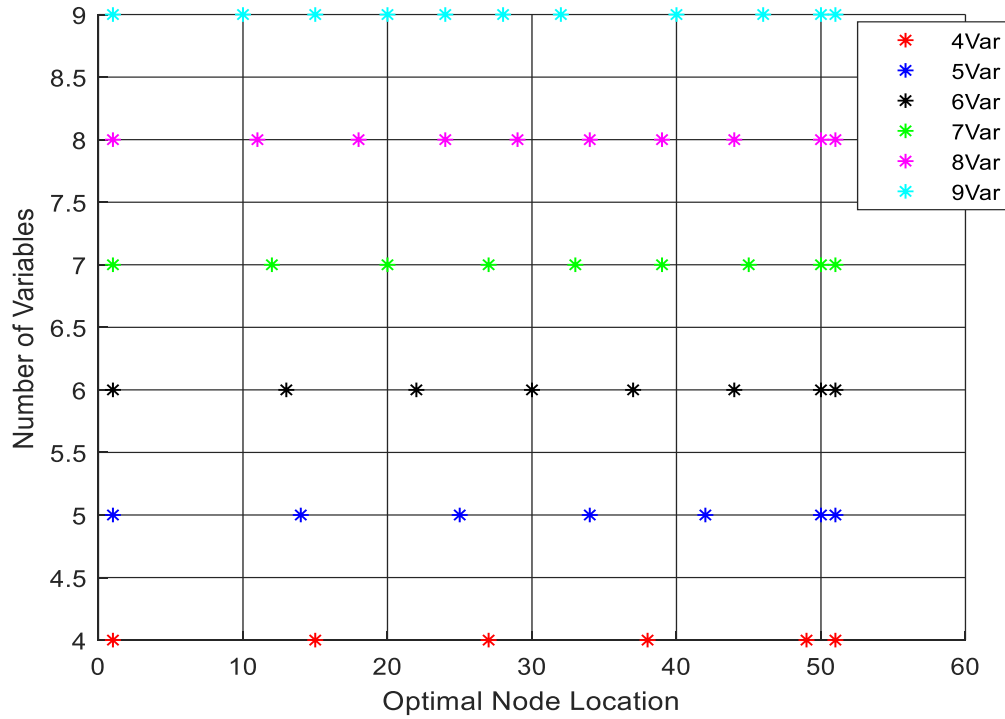
Figure 23: Optimal Solid-phase Discretization Steps selected based on (a) J_1 only (b) J_1 and J_2 Error Minimization for CC Operation

These two cases demonstrate that the higher the number of discretization nodes selected for the proposed model, the higher the accuracy of the model in voltage prediction achieved. It is noted that first and last nodes are not considered as a state variable through the analysis in this work.

5.1.2 Electrolyte Phase Optimization Results

The minimization problem for electrolyte phase as stated in Equation (78) is based on the prediction error of the first and last nodes electrolyte-phase concentration. As can be observed in Figure 25 at least two nodes from each of the three regions (separator, positive and negative electrode) of the cell are needed for electrolyte-phase concentration predictions. The PSO optimal solutions converged after 500 iteration counts as shown in Figure 24, this demonstrates the ability of the optimization scheme in solving the proposed minimization problem effectively.

71
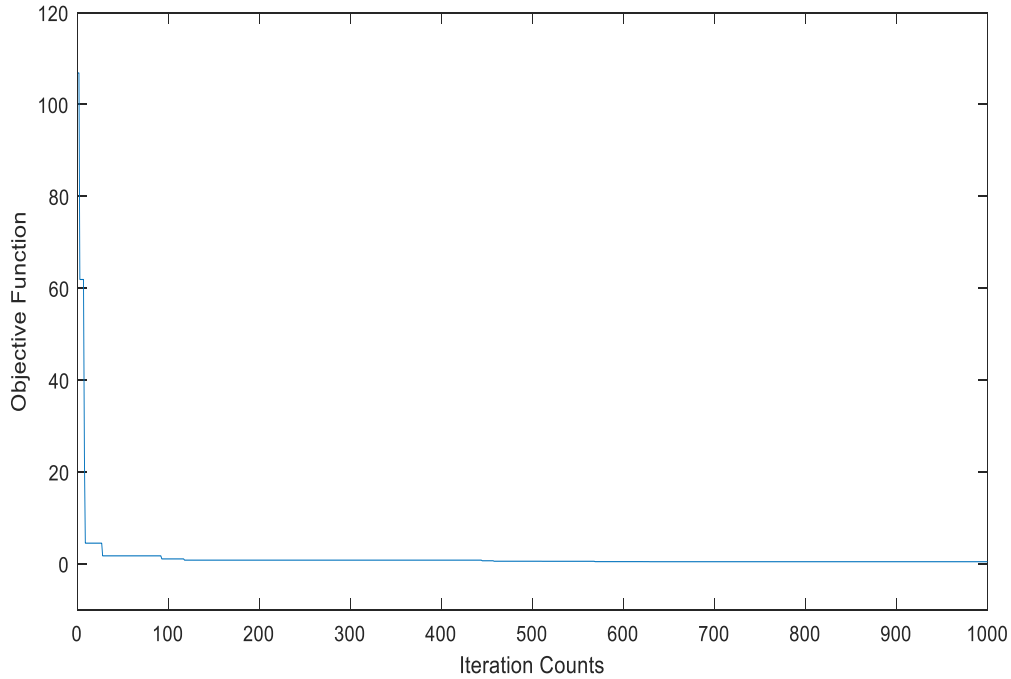
Figure 24: PSO Convergence Profile for Electrolyte-phase Optimization for CC Operation

The number of variables was increased from 6-11variables and PSO determines the optimal solution for each case from the three regions. The same two optimal nodes were selected in the separator and positive electrode, on the other hand at the negative electrode the number of optimal nodes increases as the number of variables increases, and they are spread across the length of this electrode as can be observed in Figure 25. The slow nature of the negative electrode diffusion dynamics makes the electrode prediction more influential on the overall electrolyte concentration predictions accuracy. As the number of variable increases from 6 variables to 11 variables, the magnitude of the error reduced, and the model prediction accuracy increases as can be observed in Table 2.

Table 2: Solid and Electrolyte-Phase Concentration Prediction Error

Number of Variables	Objective Function J_1 only	Objective Function $\alpha_1 J_1 + \alpha_2 J_2$	Number of Variables	Electrolyte-phase Objective Function
4	21.97	2892	6	5.52
5	27.32	2600	7	4.95
6	26.05	2397	8	4.64
7	18.57	2265	9	4.20
8	13.70	2183	10	4.20
9	10.54	2171	11	4.20
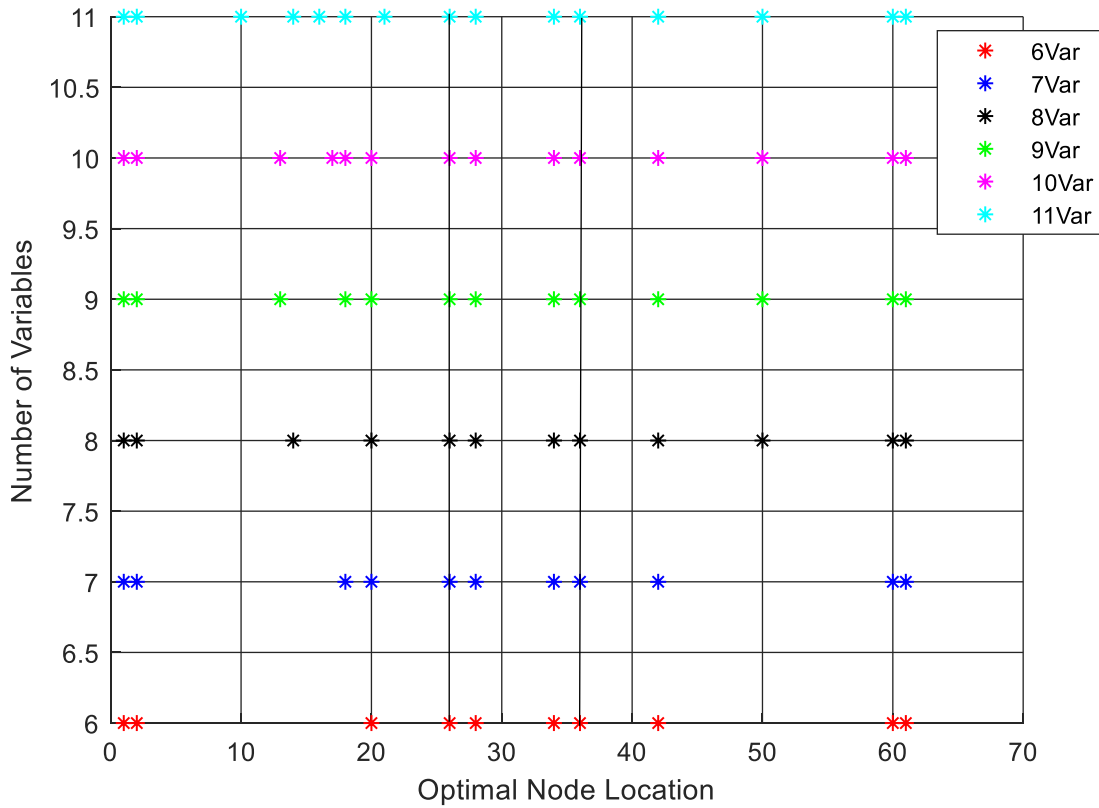
Figure 25: Optimal Electrolyte-phase Discretization Steps for CC Operation

5.1.3 Voltage and Concentration Simulation Results

Based on the optimal solutions for solid and electrolyte-phases minimization problems, the optimal nodes selected were applied to the proposed model algorithm for concentration and voltage simulations. The solid phase concentration predictions from the proposed model for different number of uneven discretized nodes were plotted against that of the reference model as shown in Figure 26. It is observed that the root mean square (rms) error between each cases and reference model decreases as the number of variables increases is as shown in Table 2.
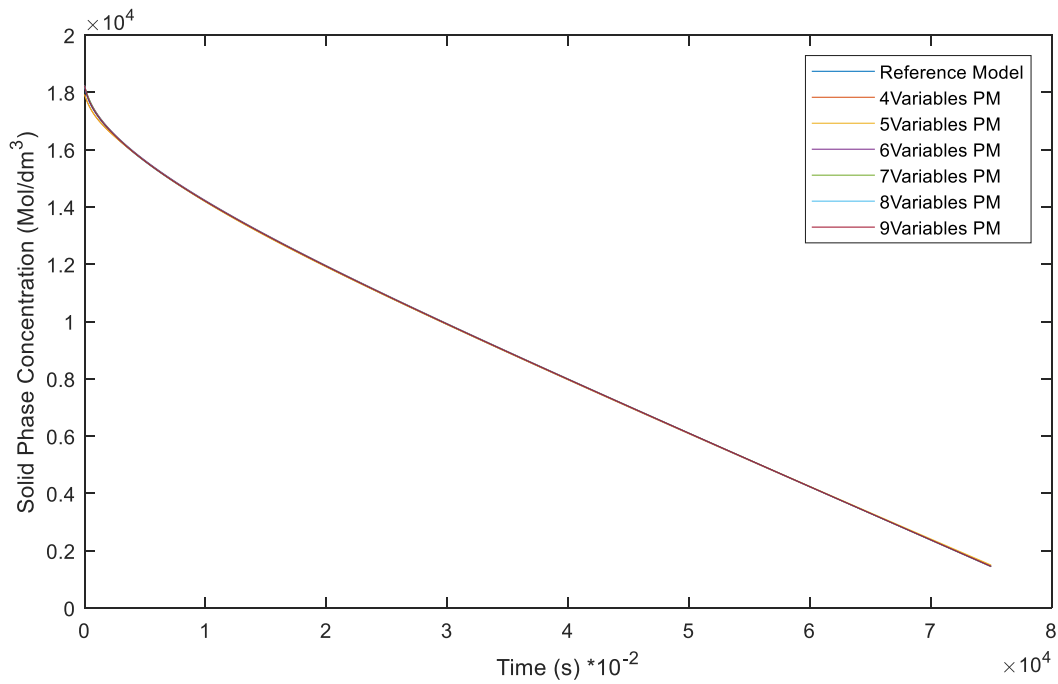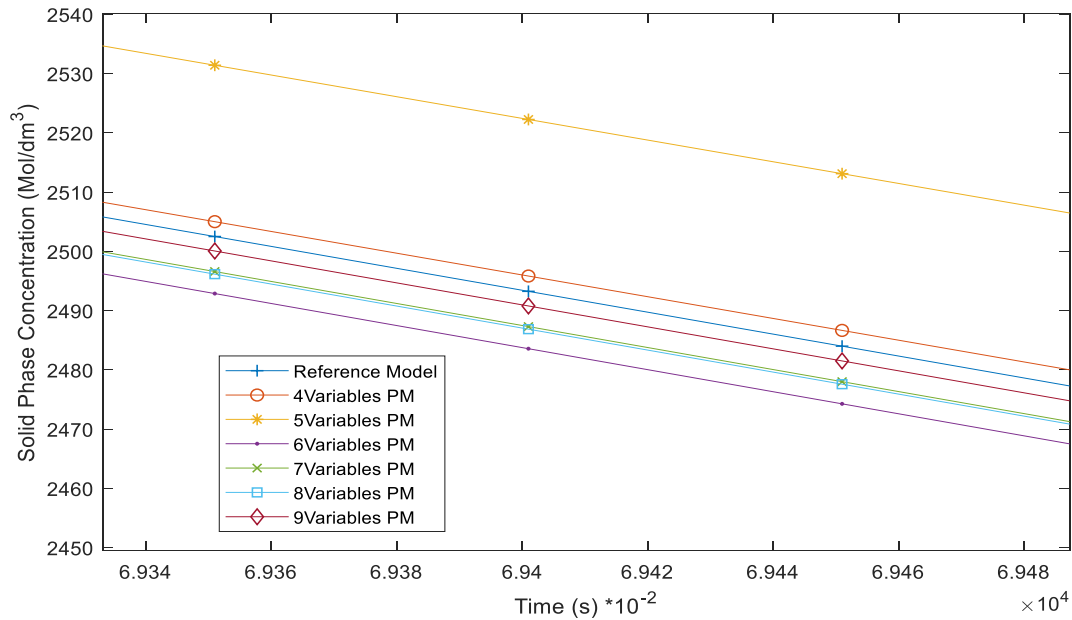
Figure 26: Solid Phase Surface Concentration for Different Discretization Nodes

The optimal number of uneven discretization nodes were determined from the predicted battery

voltage, solid and electrolyte-phases concentration as shown in Tables 2, 3 and 4. Tables 3 and 4

show the root mean square voltage error between the reference model voltage predictions and the

proposed model predictions for different numbers of solid and electrolyte phase optimal nodes. It

can be observed from the tables that as the number of optimal nodes increase in solid phase the

rms voltage error and maximum absolute error reduces gradually. But the rms voltage error and

maximum absolute error reduces exponentially as the number of optimal nodes increases for the

electrolyte phase predictions. The maximum rms and absolute voltage error for the model

predictions based on J_1 minimization only as shown in Table 3 is around 30mV and 40mV

respectively. The model prediction based on J_1 $and J_2$ minimization as shown in Table 4, are 4mV

and 12mV respectively. For both models as the number of variables increases, these two error

values reduce to approximately 0.5mv and 1.0mV for the first model and 0.8mV and 3.0mV for

the other model.

From this result it can be concluded that the model developed based solely on J_1 seems more accurate in terminal voltage prediction compare to the other model developed based on both J_1 and J_2. Since the state of charge of the proposed model was not investigate in this work, hence the first model is more efficient for voltage prediction and requires low computational effort compared to the second model.

Table 3: Voltage Prediction Error Based on J_1 Alone for CC Operation

Solid Phase Nodes	4		5		6		7		8		9	
Electrolyte Phase Nodes	Rms (mV)	Max (mV)	Rms (mV)	Max (mV)	Rms (mV)	Max (mV)	Rms (mV)	Max (mV)	Rms (mV)	Max (mV)	Rms (mV)	Max (mV)
6	3.4	4.4	3.3	4.4	3.2	4.1	3.2	3.8	3.1	3.7	3.1	3.6
7	2.4	3.2	2.3	3.2	2.2	3.0	2.1	2.7	2.1	2.6	2.1	2.5
8	1.4	2.6	1.3	2.6	1.2	2.0	1.2	1.7	1.1	1.6	1.1	1.5
9	1.1	2.6	1.1	2.6	0.92	1.8	0.87	1.4	0.83	1.3	0.84	0.12
10	1.0	2.6	0.96	2.6	0.85	1.7	0.79	1.3	0.75	1.2	0.75	0.11
11	0.76	2.6	0.71	2.6	0.63	1.8	0.53	1.3	0.48	1.1	0.48	0.96

Table 4: Voltage Prediction Error Based on J_1 and J_2 for CC Operation

Solid Phase Nodes	4		5		6		7		8		9	
Electrolyte Phase Nodes	Rms (mV)	Max (mV)	Rms (mV)	Max (mV)	Rms (mV)	Max (mV)	Rms (mV)	Max (mV)	Rms (mV)	Max (mV)	Rms (mV)	Max (mV)
6	3.6	12.3	3.8	7.4	3.5	4.5	3.4	3.9	3.4	3.9	3.4	3.9
7	2.8	8.4	2.8	7.3	2.5	4.4	2.4	3.3	2.3	3.3	2.3	3.1
8	2.7	7.0	1.9	7.0	1.5	4.2	1.4	2.9	1.4	2.9	1.4	2.9
9	3.5	9.6	1.7	7.0	1.3	4.2	1.1	2.9	1.1	2.9	1.1	2.9
10	3.6	9.8	1.6	7.0	1.1	4.2	0.96	3.0	0.96	3.0	0.95	2.9
11	3.8	9.9	1.4	7.0	1.0	4.2	0.82	3.0	0.79	3.0	0.82	2.9

From the prediction result, it is observed that from 7 or higher unevenly discretized nodes upward, the predicted terminal voltage and li-ion concentration profiles from the proposed model follows closely that of the reference model respectively. There are little, or no significant error as demonstrated in Tables 3 and 4 between the reference and proposed model predictions. Likewise, for electrolyte phase predictions, the magnitude of the rms and maximum absolute voltage error are approximately the same from 9 variables model upward. Conclusively, 7 and 9 unevenly

discretized nodes are sufficient for accurate prediction of solid and electrolyte phase concentration dynamics. Above this number of optimal nodes in both phases, there is no significant improvement in the accuracy of the proposed model. The proposed model achieved about 7 times complexity reduction in terms of the number of nodes compared to the evenly discretized model.

The prediction performance of the proposed model (SPMe) was compared with the voltage prediction of single particle model without electrolyte as shown in Figure 27 (a) and (b). It can be observed from Figure 27 (a) that the rms and maximum absolute error between the reference model (SPMe with even discretization) predictions and the SPM with even discretization prediction is 74mV and 77mV respectively. Likewise, the rms and maximum absolute error between the predictions of SP model with uneven discretization based on the optimal solution from PSO and the proposed model prediction is 74mV and 76mV respectively. The magnitude of these prediction errors highlights the importance of electrolyte dynamics inclusion to the conventional single particle model.
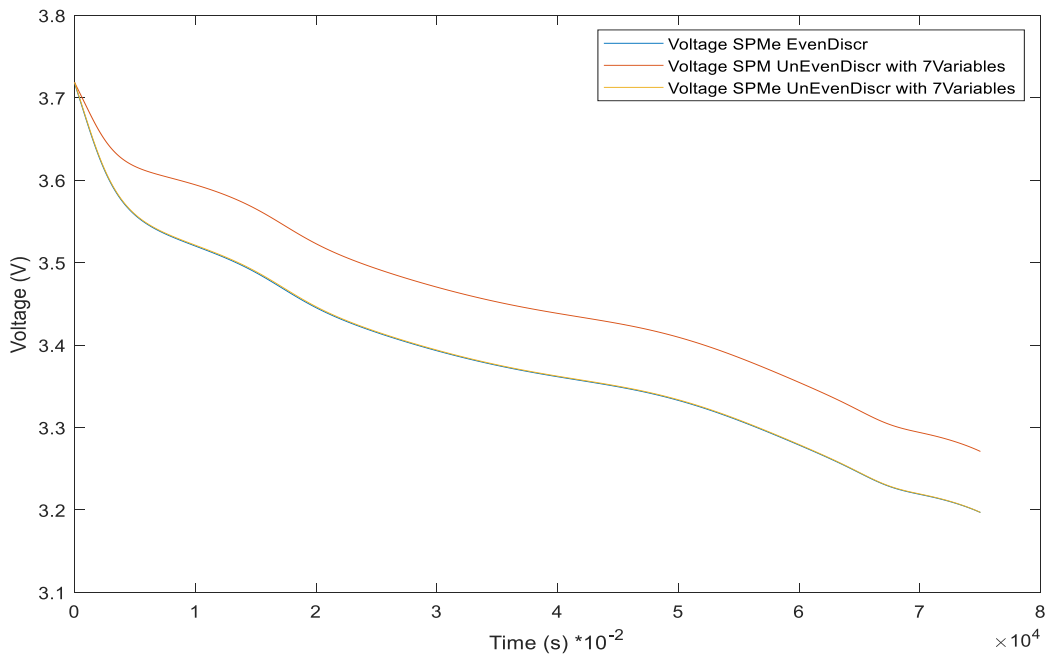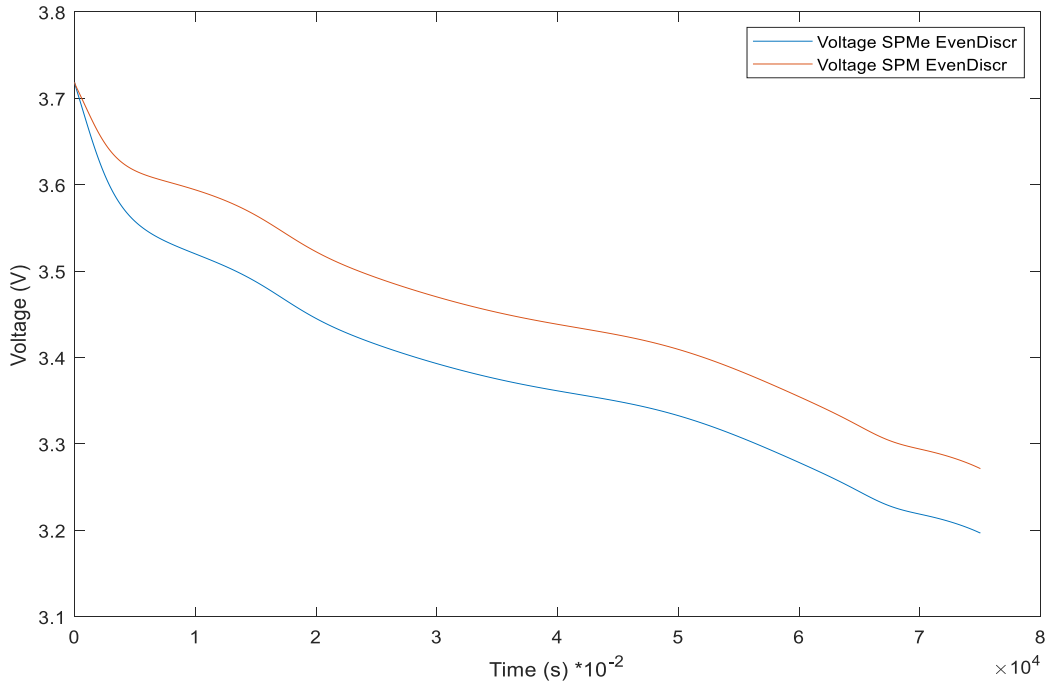
Figure 27: Voltage Predictions for Single particle model without/with electrolyte dynamics (SPM/SPMe) (a) for reference model (b) for proposed model and reference model.

The voltage predictions of the reference model and the proposed model based on J_1 objective function as shown in Figures 28 (a), (b) and (c) are presented as a case study. Different number of solid-phase optimal nodes were applied to the proposed model with 9 electrolyte-phase nodes. The prediction errors between the two models reduced from 2.6millivolts for 4 nodes to 0.12millivolt for 9 nodes. The trend of the voltage prediction by the proposed model shows that the prediction capacity of the proposed model from 7 nodes upwards are approximately the same. This demonstrate that 7 optimally selected nodes for solid phase concentration profile is sufficient to predict the battery terminal voltage accurately.
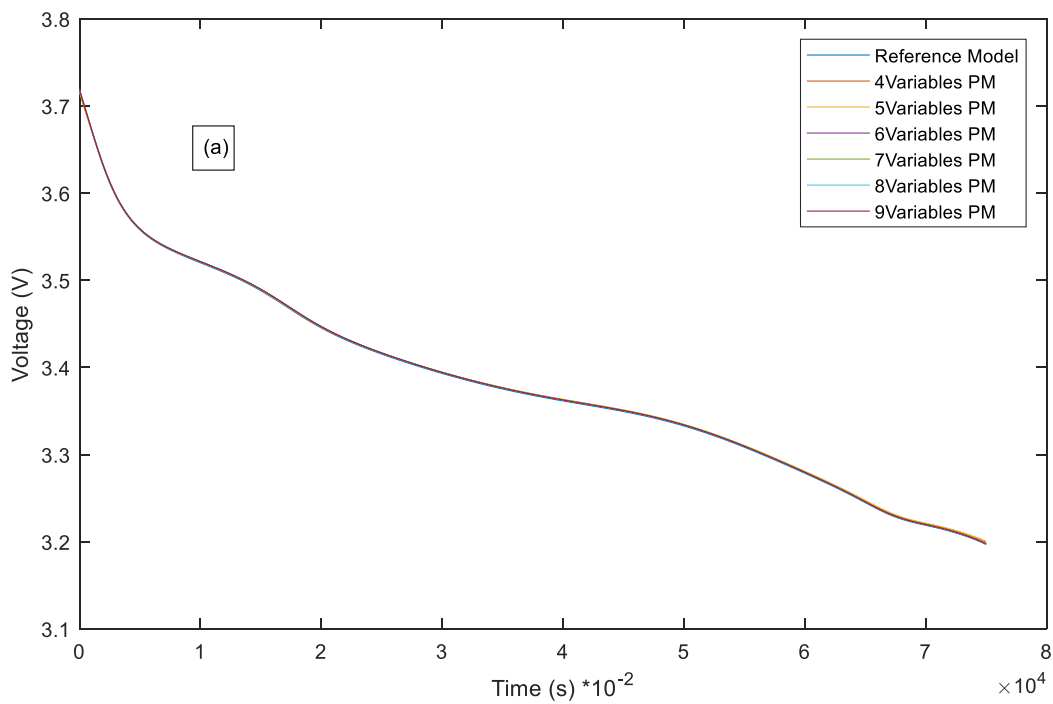
Figure 28: (a)Voltage prediction of the proposed model for different number of discretization steps in solid phase for J_1 only (b) Magnified voltage prediction results (c) Voltage prediction error for each number of variaboles model for CC Operation

Figure 29 shows the prediction results of the proposed model based on J_1 and J_2 objective function with respect to the reference model. The magnified figure of the predicted voltage, and the prediction error shows that 7 nodes model upward gives a predicted voltage close to the reference model prediction, and the maximum prediction error of 10millivolts from 4 optimal nodes model reduces to 2millivolts for 9 optimal nodes model.
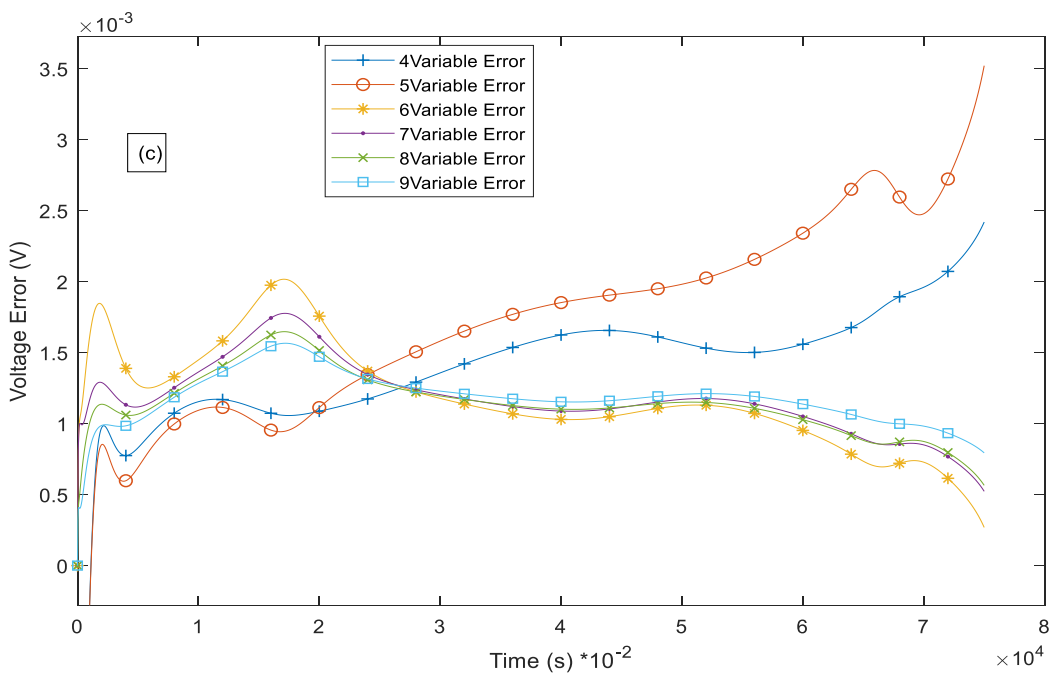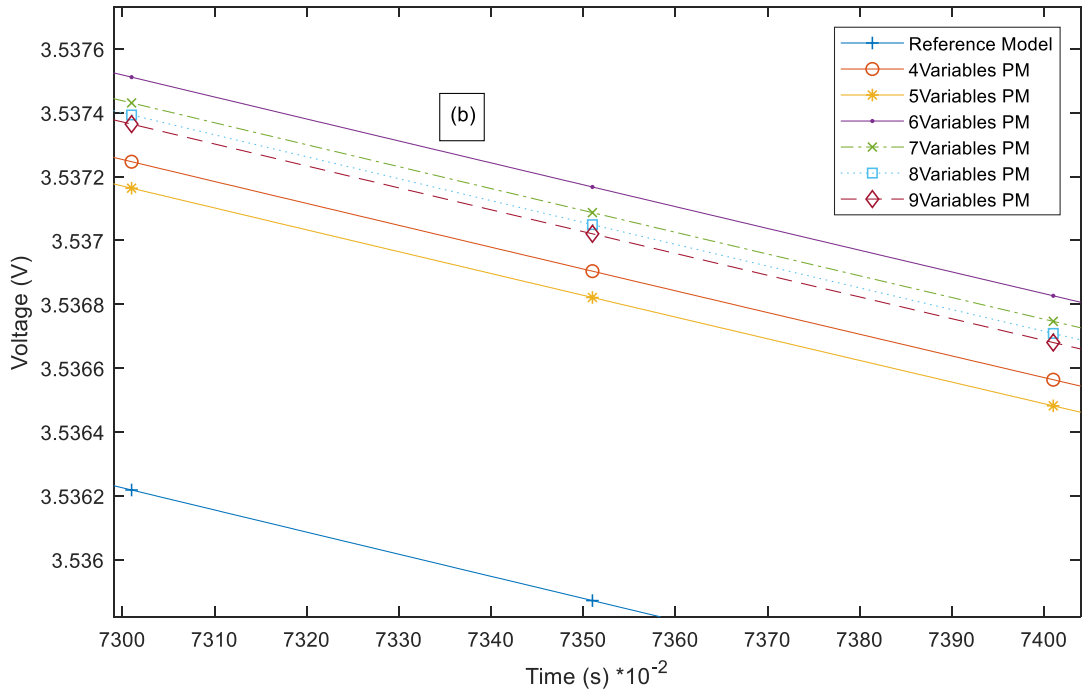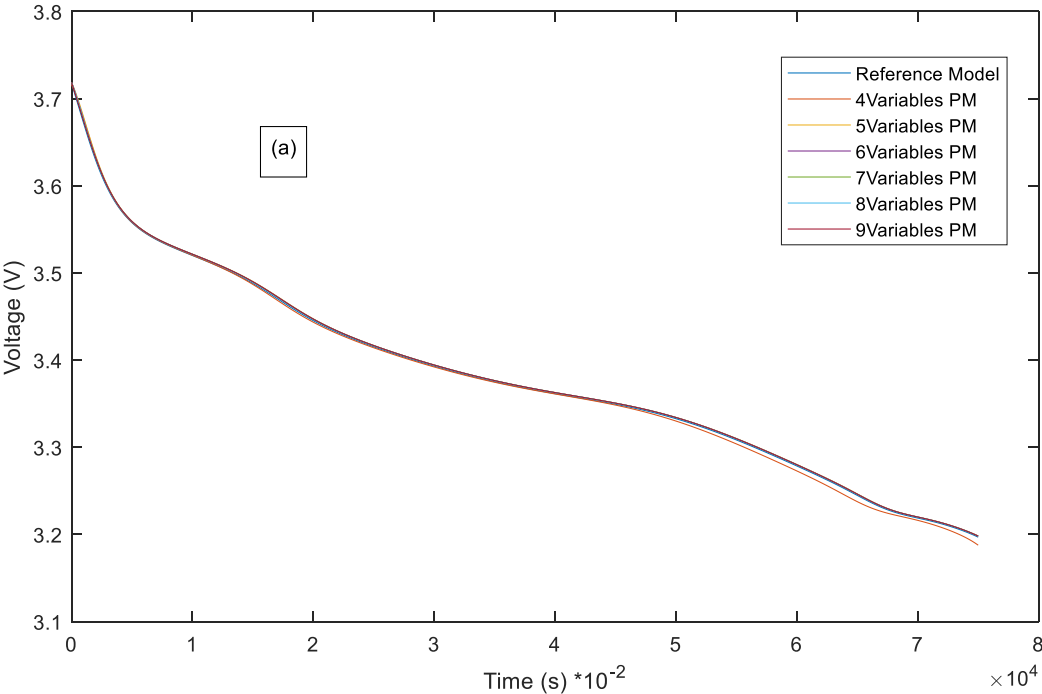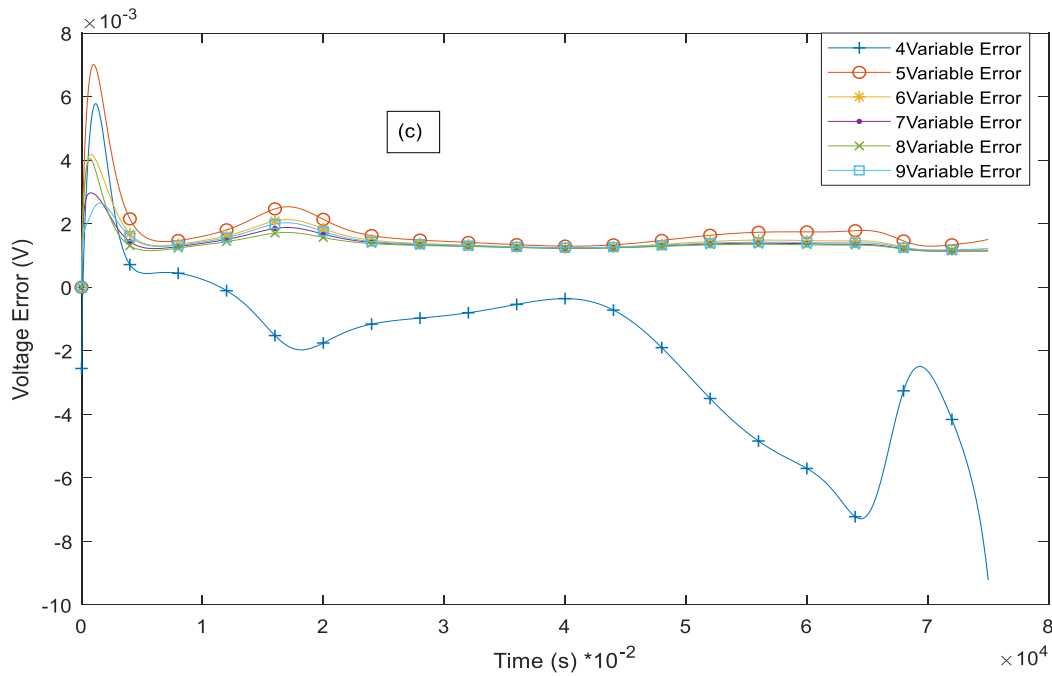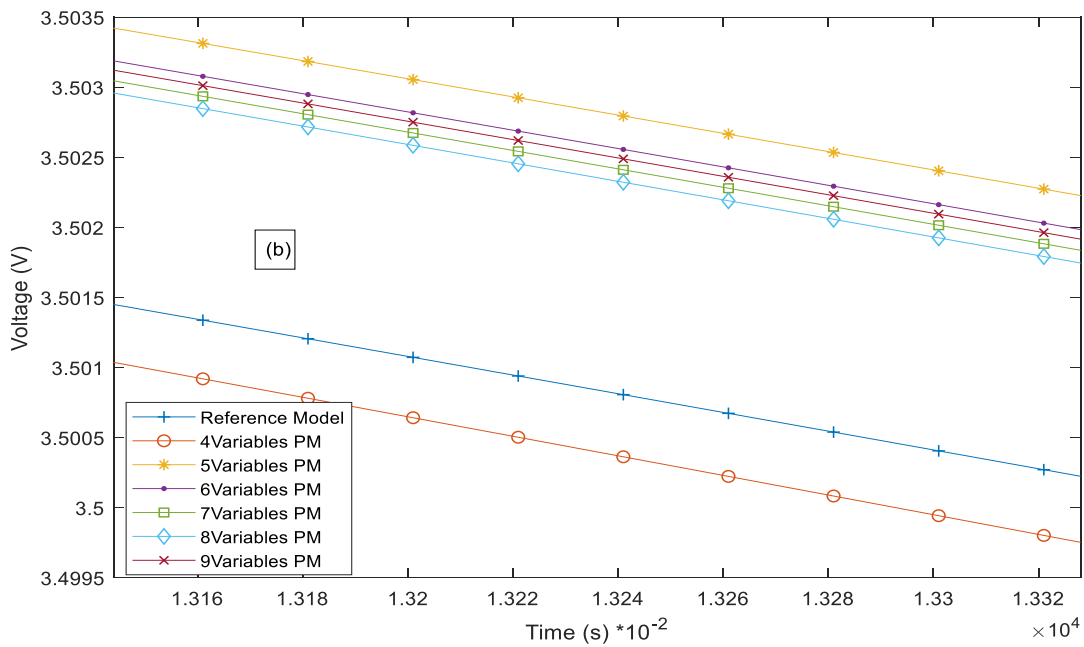
Figure 29: (a)Voltage prediction of the proposed model for different number of discretization steps in solid phase for J_1 and J_2 (b) Magnified voltage prediction results (c) Voltage prediction error for each number of variaboles model for CC Operation

5.2   Pulse Charge/Discharge Operation

A pulse charge and discharge operation as shown in Figure 30 was applied to the proposed model to investigate its capability and performance under different applied current profile.
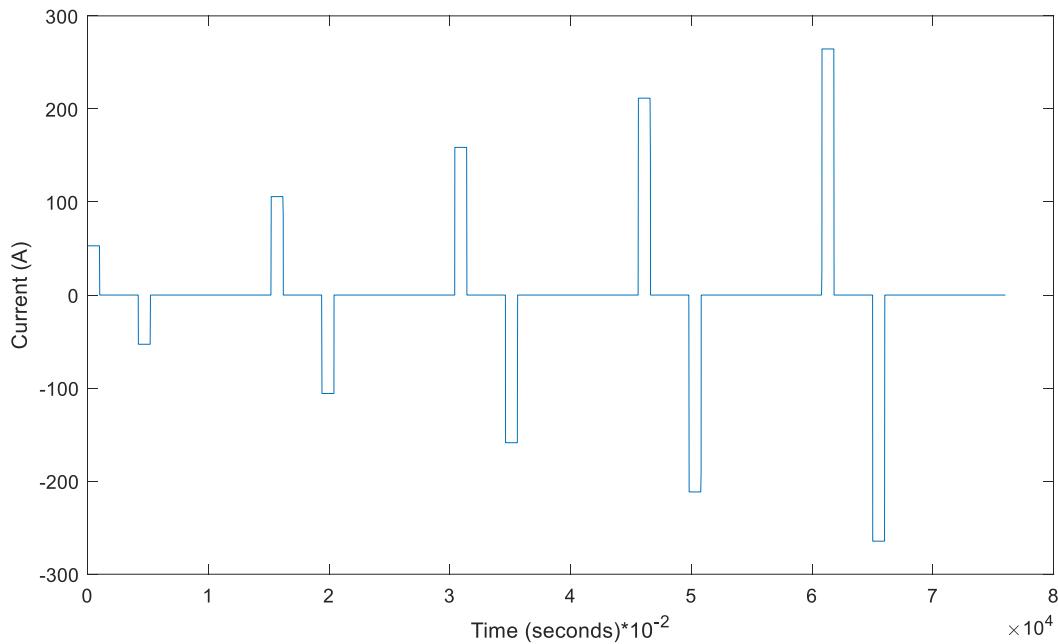
Figure 30: Pulse Charge/Discharge Current Operation

The structure of the proposed model and the optimization algorithm are the same as for the constant current operation. The PSO algorithm show a great convergence rate as shown in Figures 31 (a) and (b), the optimal solution converged after 300 and 400 iteration counts for the two solid phase objective functions respectively.
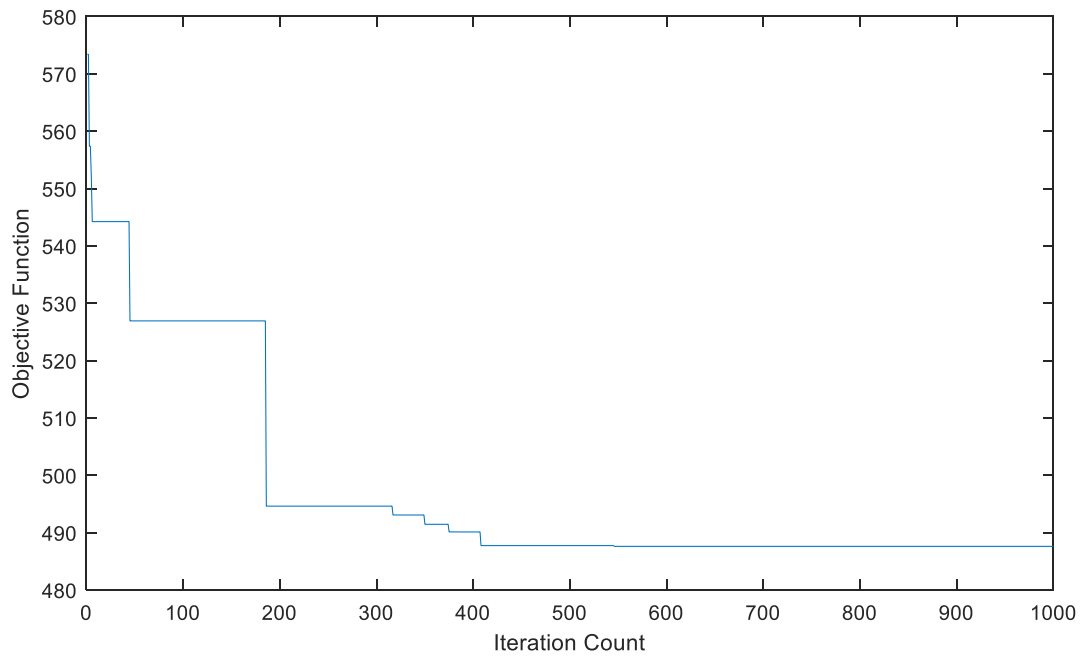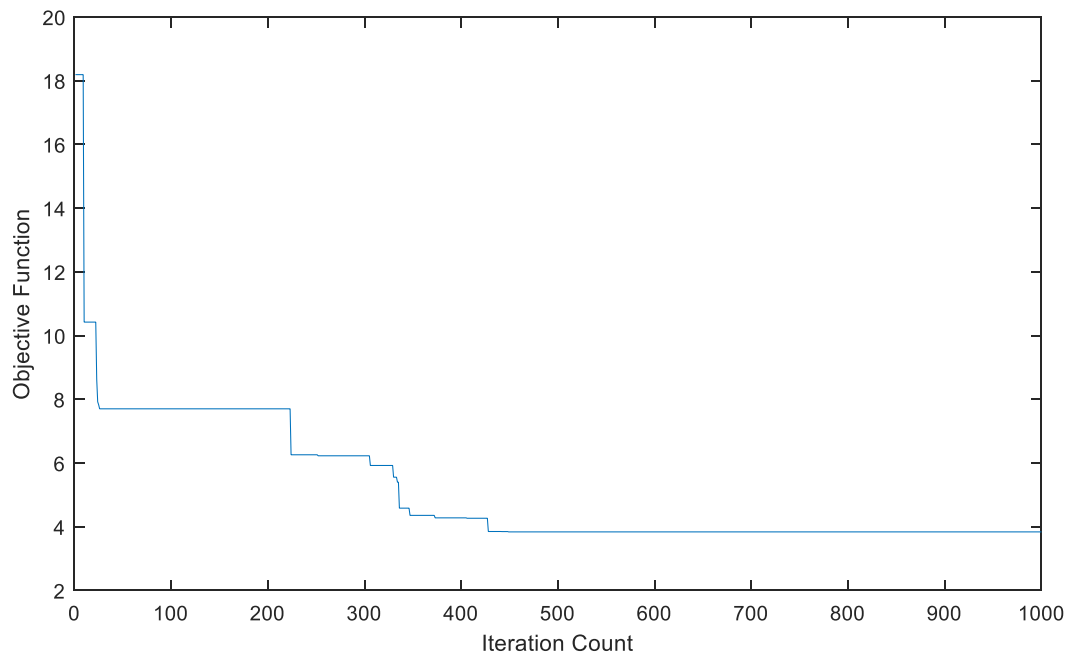
Figure 31: PSO Convergence Profile for Solid-phase Optimization for Pulse charge/Discharge Operation based on (a) J_1 only (b) J_1 and J_2.

5.2.1 Solid Phase Optimization Results

The solid phase PSO comprises of two objectives functions as developed for constant current operation: one based on surface concentration error (J_1) only and the other based on surface and bulk concentration (J_1 and J_2). The optimal nodes selected for both cases are as shown in Figure 32 (a) and (b). Figure 32a show the node selected based on J_1 alone, the selected optimal nodes are close to the surface of the particles because of the strong gradient at the surface resulting from the applied boundary conditions. The trend of the optimal nodes selected is similar to the one present in [16]. For the second objective function, Figure 32b show that the optimal selected nodes are disperse across the entire radius of the particles as the number of the nodes increases. This trend is attributed to the inclusion of bulk concentration in the structure of the objective function. As the number of uneven discretization nodes increases, the accuracy of the proposed model in concentration prediction increases with respect to the reference model, as can be observed in Table 5.
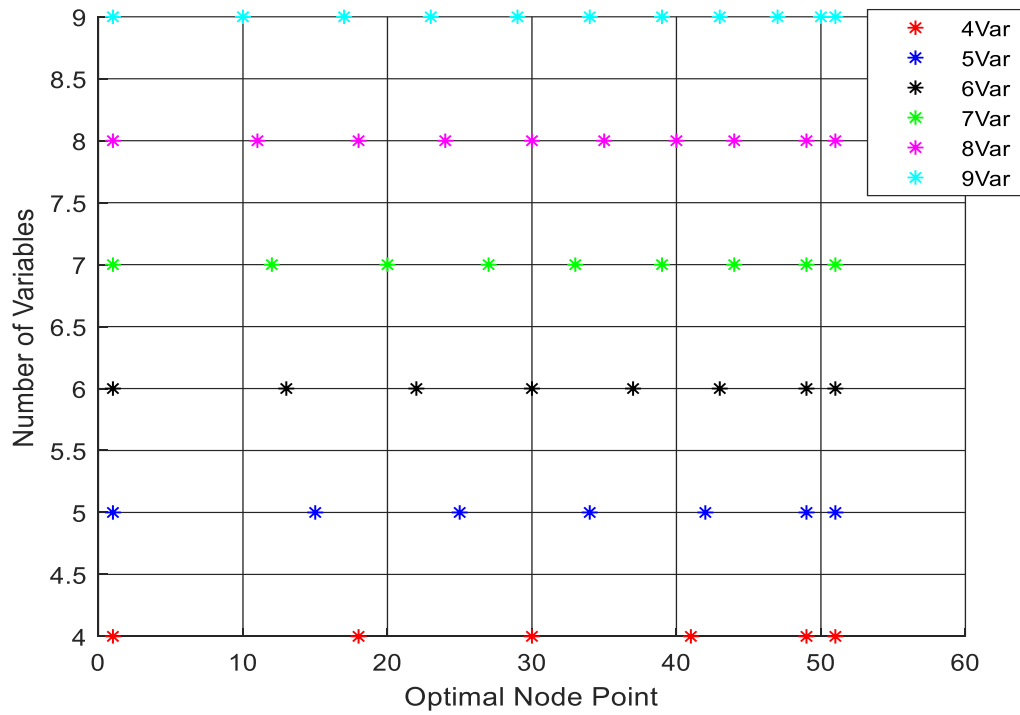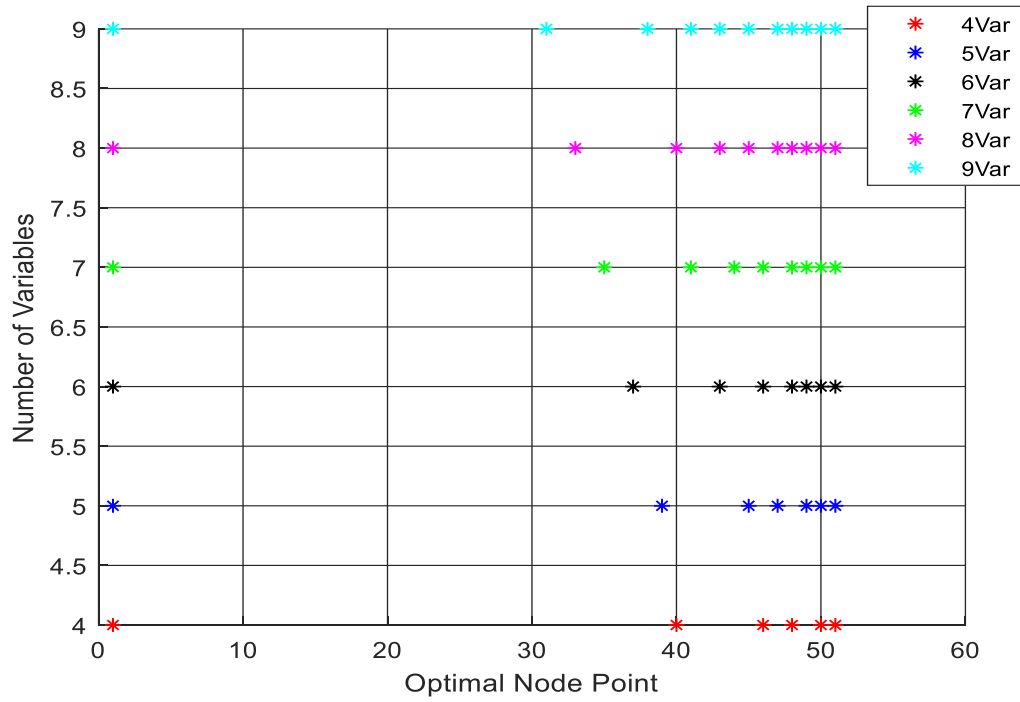
Figure 32: Optimal Solid-phase Discretization Steps selected based on (a) J_1 only (b) J_1 and J_2 Error Minimization for Pulse Operation

5.2.2 Electrolyte Phase Optimization Results

The structure of the electrolyte phase optimization algorithm under pulse operation is the same as that of constant current operation and the optimal nodes selected for the different number of cases is as shown in Figure 33. The same two nodes were selected in the positive electrode and separator for all the different number of states investigated, indicating the sensitivity of the proposed model to the concentration dynamics in the negative electrode. This correspond to the observations under the constant current operation. Negative electrode is the most contributive region due to its slow dynamic to the overall concentration dynamics prediction capability of this proposed model. It can be observed that as the number of optimal nodes increases, more nodes were selected in the negative electrode and they become denser towards surface of the particle.
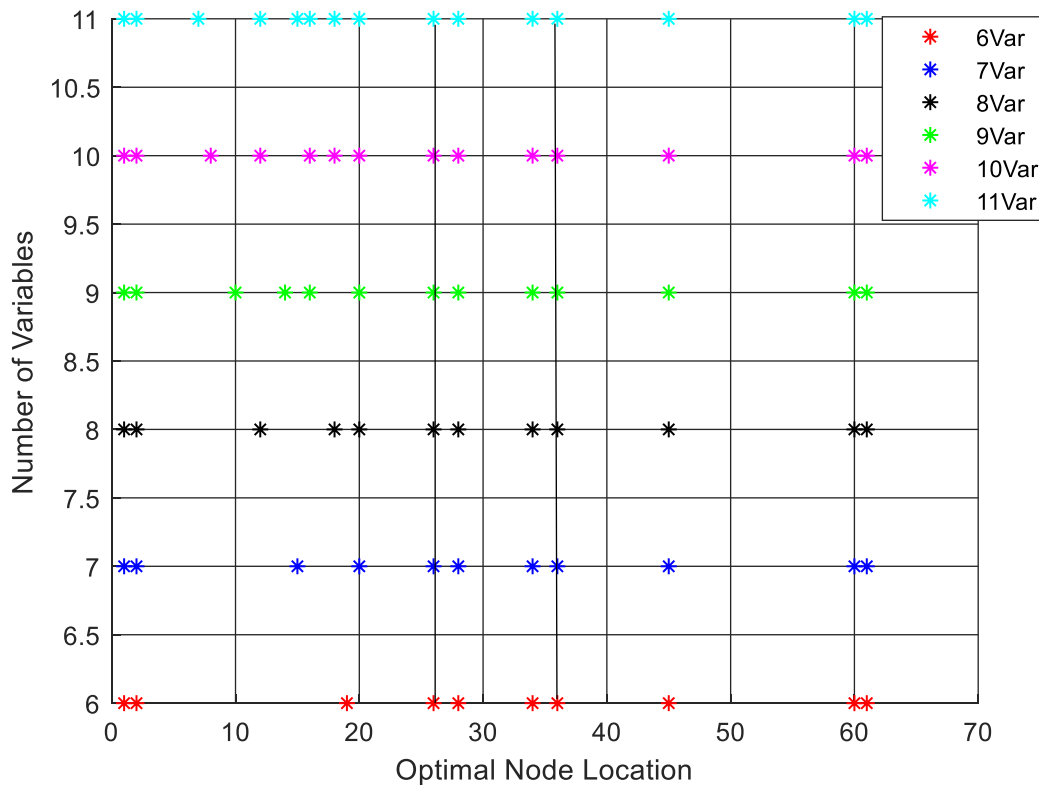
Figure 33: Optimal Electrolyte-phase Discretization Steps for Pulse Operation

The error between the proposed model and reference model, for electrolyte phase concentration predictions reduces as the number of discretization nodes increases as can be observed in Table 5. The inclusion of J_2 in the solid phase objective function cause a great increment in the error between the proposed model and reference model prediction. Also, as can be seen from Table 7, there is no improvement in the proposed model voltage predictions accuracy with the inclusion of J_2.

Table 5: Solid and Electrolyte-Phase Concentration Prediction Errors for Pulse Operation

Number of Variables	Objective Function J_1 only	Objective Function $\alpha_1 J_1 + \alpha_2 J_2$	Number of Variables	Electrolyte phase Objective function
4	18.93	1255.1	6	16.23
5	11.03	964.06	7	12.23
6	7.29	781.97	8	11.30
7	5.48	659.51	9	10.87
8	3.74	572.57	10	10.77
9	3.40	505.99	11	10.77

5.2.3 Voltage and Concentration Simulation Results

Tables 6 and 7 shows the rms and maximum absolute voltage prediction errors between the proposed model prediction and the reference model based on pulse charge/discharge operations. The concentration profiles for both solid and electrolyte phase were computed based on the optimal discretized nodes selected by the PSO and applied for terminal voltage predictions. Tables 6 depicts the prediction error based on J_1 alone and it can be observed that the maximum rms and absolute prediction error of 1.2mV and 5.8mV for 4 variables based proposed model reduced to 0.4mV and 4.3mV respectively as the number of states were increased. Tables 7 show the

prediction error based on J_1 and J_2 and it can be observed that the maximum rms and absolute prediction error of 2.1mV and 25.2mV reduced to 1.1mV and 7.0mV respectively as the number of states were increased. Comparing the prediction errors for the proposed model based on the two objective function shows that the inclusion of solid-phase bulk concentration in the objective function does not improve the model voltage prediction capability but it might be influential in the model capability for state of charge estimations. Therefore, only surface concentration error minimization is essential in the determination of the optimal nodes for the pulse operation. Furthermore, it can be observed that the proposed model accuracy become less sensitive to any increment in the number of nodes above 7 and 9 nodes for solid and electrolyte phase predictions respectively.

Table 6: Voltage Prediction Error Based on J_1 Alone for Pulse Operation

Solid phase Nodes (J_1)	4		5		6		7		8		9	
Electrolyte phase Nodes	Rms (mV)	Max (mV)	Rms (mV)	Max (mV)	Rms (mV)	Max (mV)	Rms (mV)	Max (mV)	Rms (mV)	Max (mV)	Rms (mV)	Max (mV)
6	1.2	5.8	0.95	5.3	0.68	5.2	0.56	5.1	0.57	5.1	0.56	5.1
7	1.1	5.5	0.89	5.0	0.61	4.5	0.49	4.3	0.49	4.2	0.49	4.3
8	1.1	5.5	0.88	5.0	0.60	4.5	0.46	4.3	0.46	4.2	0.45	4.2
9	1.1	5.5	088	5.0	0.59	4.5	0.44	4.3	0.43	4.3	0.42	4.3
10	1.1	5.6	0.88	5.0	0.59	4.6	0.44	4.3	0.43	4.3	0.42	4.3
11	1.1	5.6	0.88	5.1	0.59	4.6	0.44	4.4	0.43	4.3	0.42	4.3

Table 7: Voltage Prediction Error Based on J_1 and J_2 for Pulse Operation

Solid phase Nodes (J_1 J_2)	4		5		6		7		8		9	
Electrolyte phase Nodes	Rms (mV)	Max (mV)	Rms (mV)	Max (mV)	Rms (mV)	Max (mV)	Rms (mV)	Max (mV)	Rms (mV)	Max (mV)	Rms (mV)	Max (mV)
6	2.1	25.2	1.5	21.4	1.1	17.5	1.1	14.3	1.1	13.9	1.3	8.3
7	2.0	24.8	1.5	21.1	1.1	17.2	1.1	14.0	1.1	13.5	1.1	7.8
8	2.0	24.8	1.4	20.9	1.1	17.0	1.1	13.8	1.1	13.3	1.1	7.5
9	2.0	24.6	1.4	20.8	1.1	16.9	1.1	13.8	1.1	13.3	1.1	7.3
10	2.0	24.6	1.4	20.8	1.1	16.9	1.1	13.7	1.2	13.3	1.2	7.2
11	2.0	24.6	1.4	20.8	1.1	16.9	1.1	13.7	1.2	13.3	1.1	7.0

Based on the optimal nodes selected by the optimization algorithm for solid phase concentration prediction based on J_1, and 9 electrolyte phase optimal nodes, the cell terminal voltage was investigated as a case study. The maximum errors were determined as shown in Figure 34, and from the magnified voltage predictions plot, it is observed that as the number of nodes increase, the prediction error decrease and the predicted voltage from 7 optimal nodes model upward follows closely the reference model predicted voltage as established earlier in the error tables.
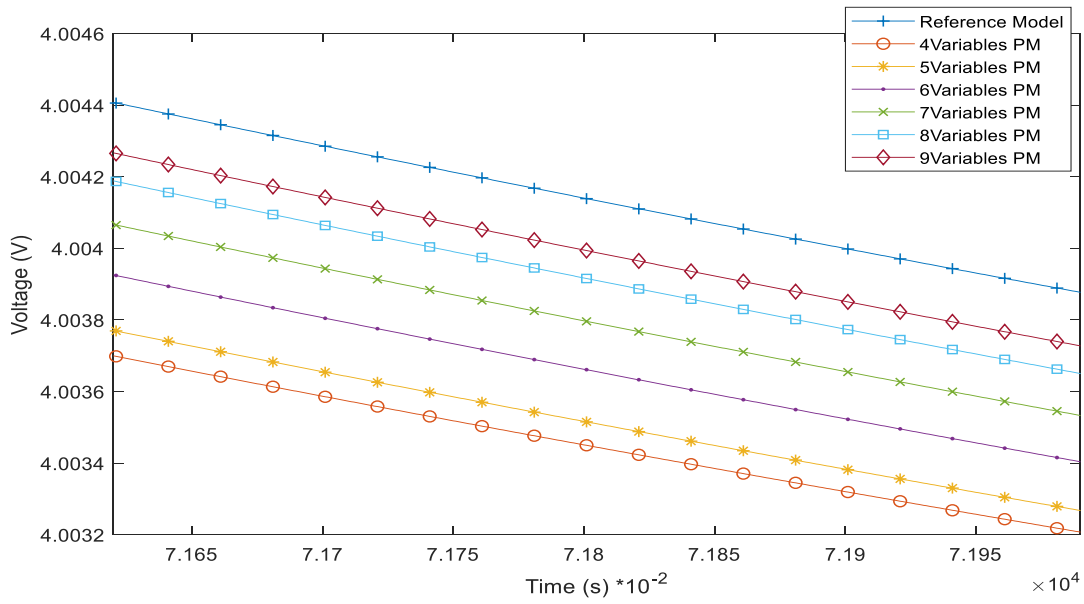
Figure 34: (a)Voltage prediction of the proposed model for different number of discretization steps in solid phase for J_1 only (b) Magnified voltage prediction results for pulse operation.

Figure 35 shows the voltage prediction of the proposed model with respect to the reference model for different number of solid phase state based on both J_1 and J_2. The predicted voltage by the proposed model follows closely with that of the reference model with an increase in maximum prediction error as the c-rate increases. The maximum prediction error of 25millivolts for a 4 optimal nodes model reduced to 7millivolts for 9 optimal nodes model.
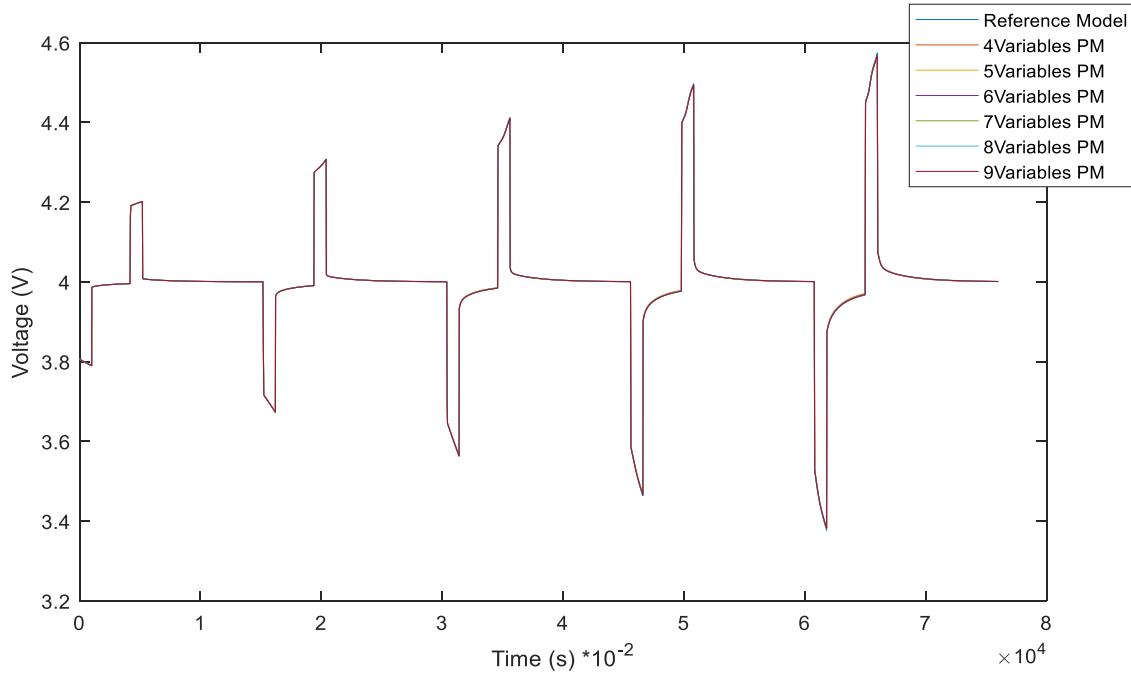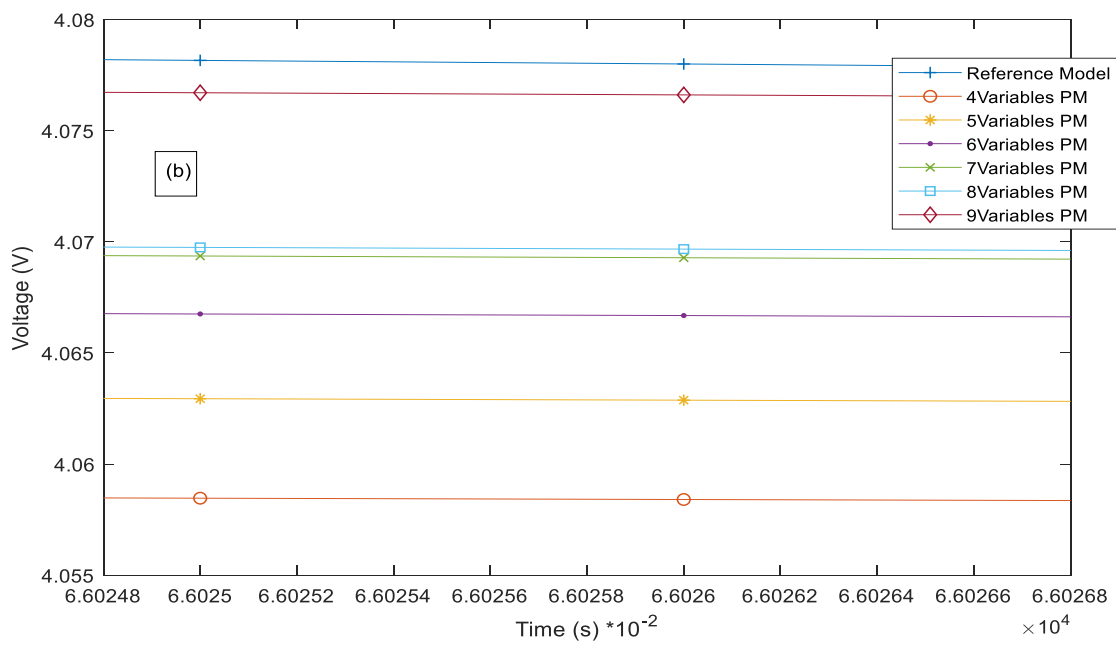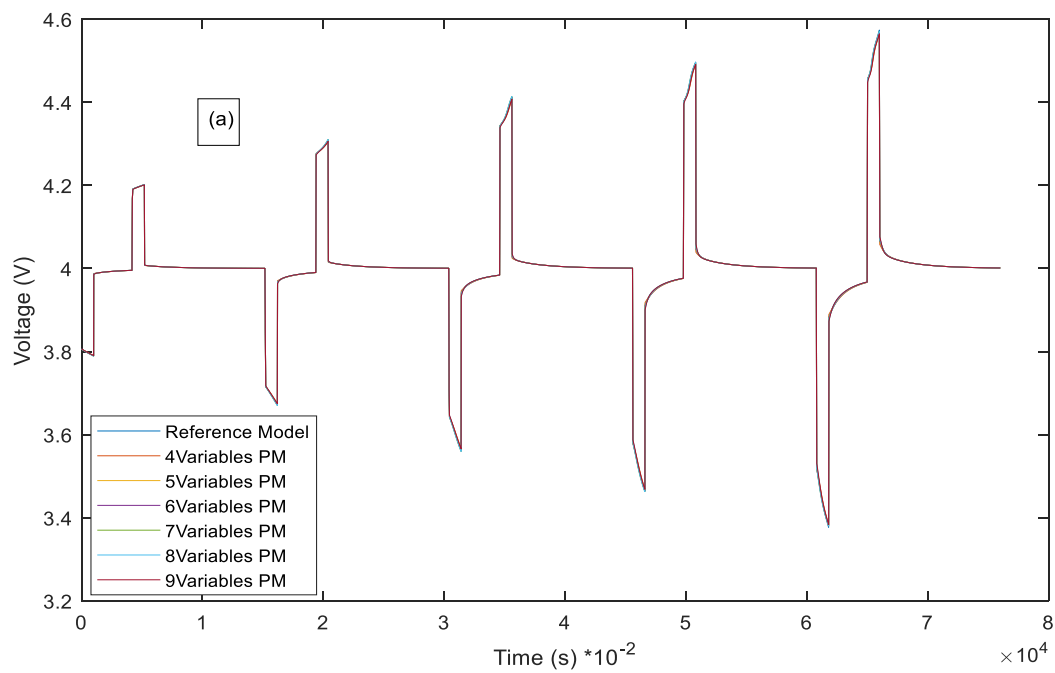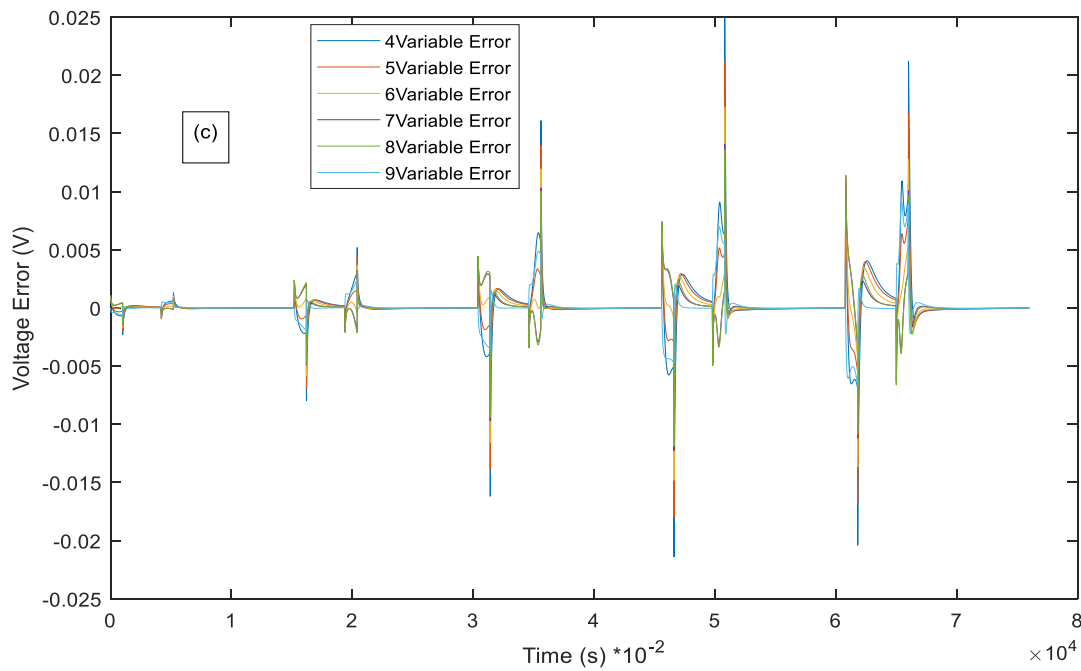
Figure 35: (a)Voltage prediction of the proposed model for different number of discretization steps in solid phase for J_1 and J_2 (b) Magnified voltage prediction results (c) Voltage prediction error for each number of variaboles model for Pulse Operation

5.3 Hybrid Pulse Power Characterization (HPPC) Operation

Electric vehicles operate with an HPPC current profile, the capability of the proposed model in predicting battery dynamics under HPPC operating condition is investigated in this section. The HPPC current profile applied to the proposed model is as shown in Figure 36 where the battery is discharge with a constant current 1C operation and experience 4C occasional charge and discharge current.
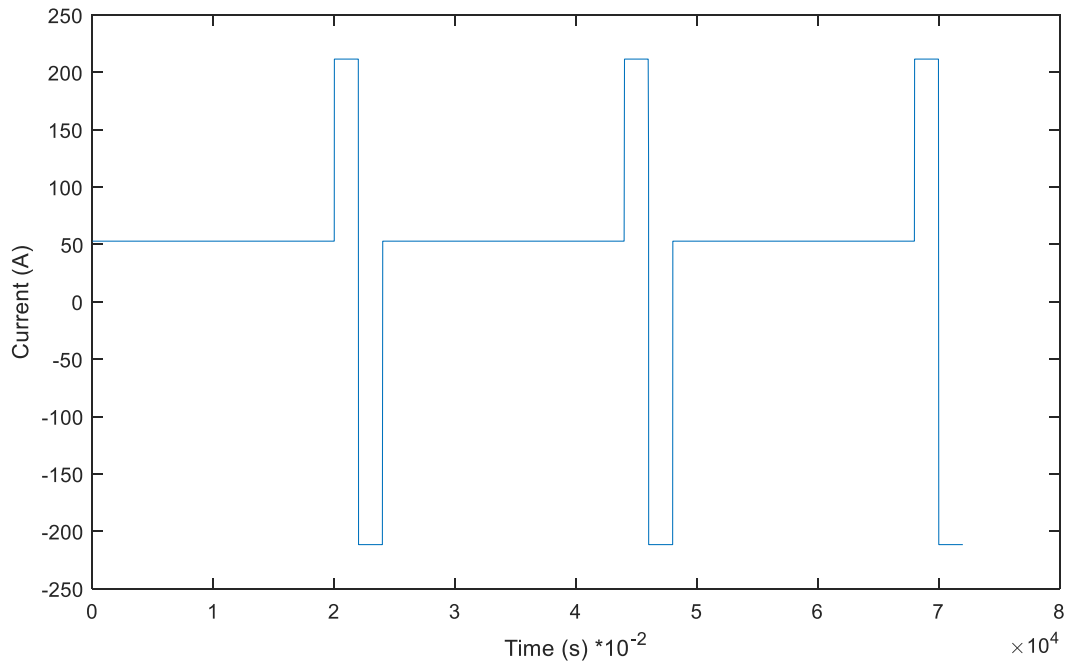
Figure 36: HPPC Current Operation

5.3.1 Solid Phase Optimization Results

The PSO for optimal nodes selection is as constructed for CC operation for solid phase nodes optimization. The PSO solution converges after 400 iteration counts for both constructed solid phase objective functions as shown in Figures 37a and 37b.
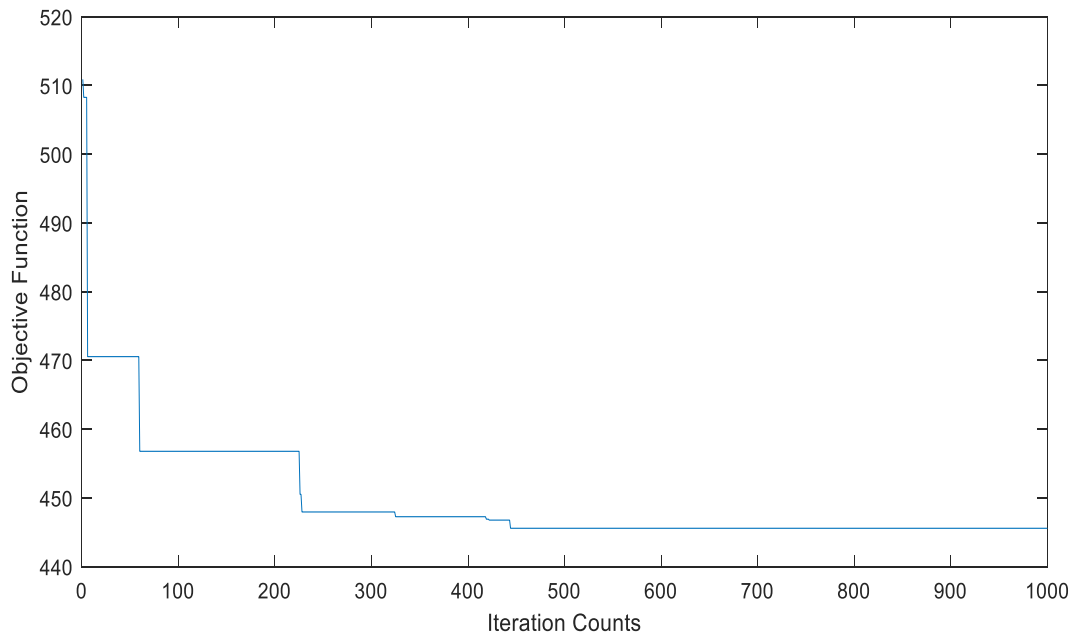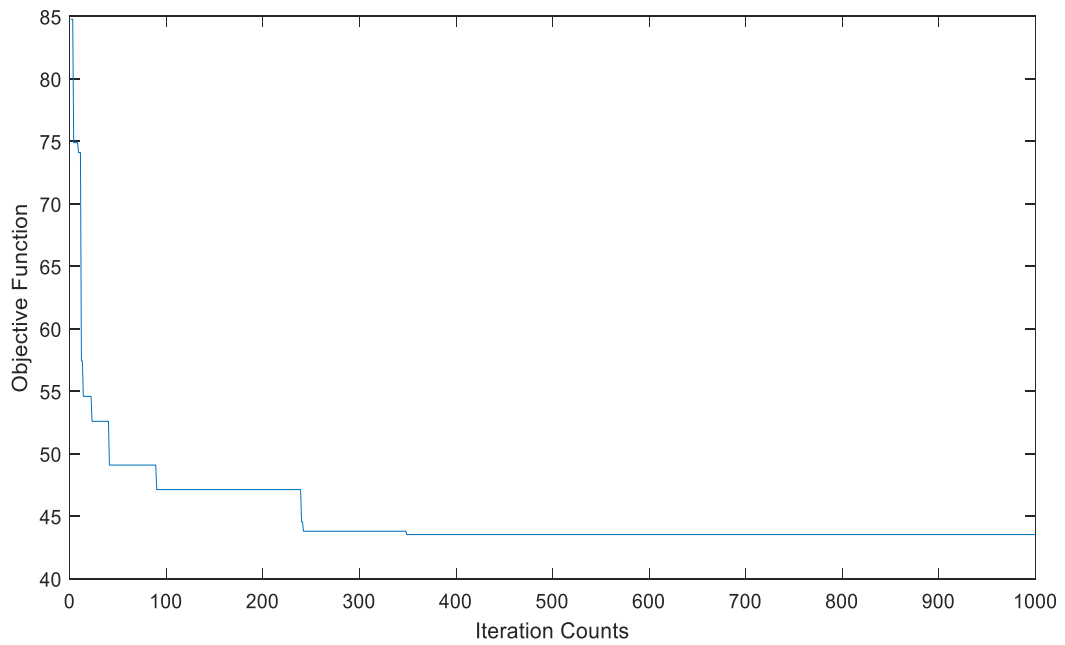
Figure 37: PSO Convergence Profile for Solid-phase Optimization for HPPC Operation based on (a) J_1 (b) $J_1 \ and \ J_2$

Figure 38a show the optimal nodes selected based on the model with J_1 objective function and the

nodes are closely packed towards the particles surface and more scattered towards the particles

core. This can be attributed to the contribution of both constant current and pulse current operations involvement in HHPC operations. The optimal nodes selected based on the model with J_1 and J_2 objective function is as shown in Figure 38b, the selected nodes are more dispersed across the particle's radius. As shown in Table 8, the cost of objective function reduces rapidly as the number of optimal nodes increase for both cases. The reduction in the prediction error as the number of nodes increases are insignificant compare to the improvement achieved under CC and pulse operation, and this serve as a motivation for performing sensitive analysis for the proposed model with respect to each current operation results.
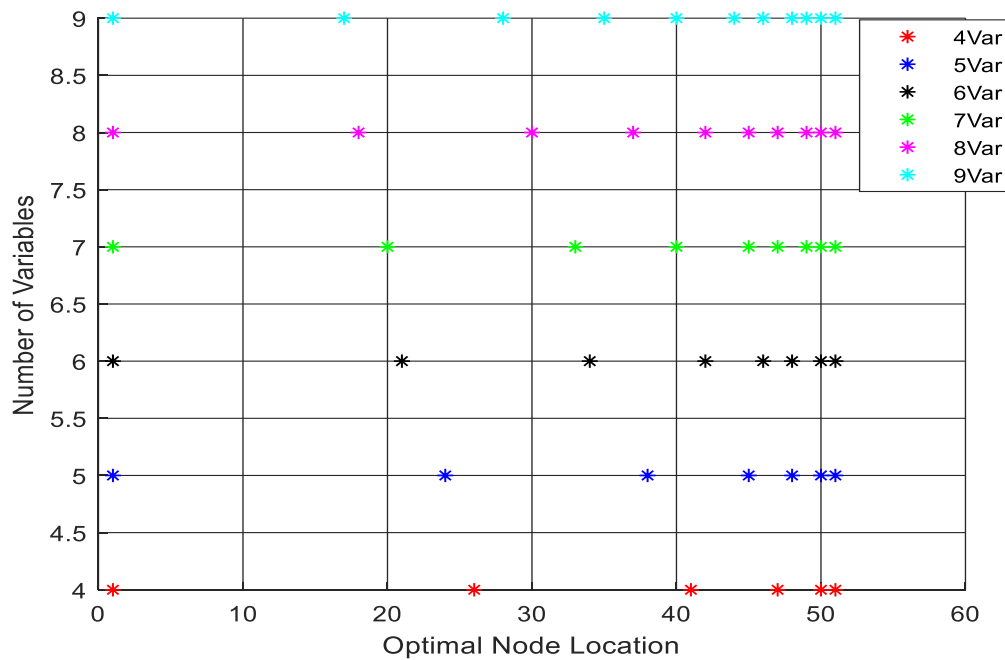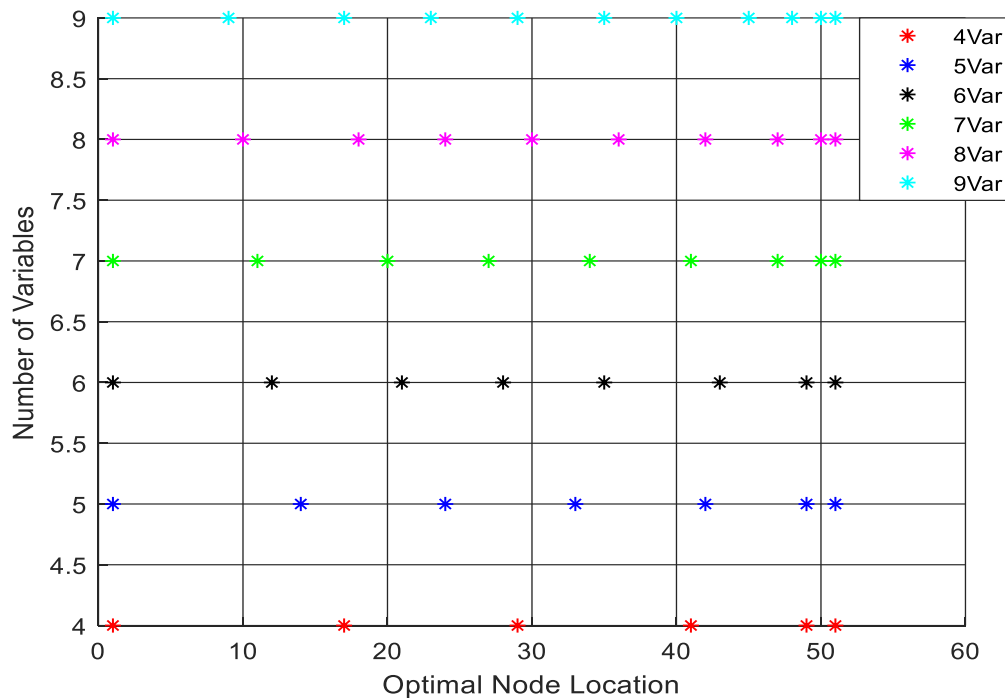
Figure 38: Optimal Solid-phase Discretization Steps selected based on (a) J_1 only (b) J_1 and J_2 Error Minimization for HPPC Operation

5.3.2 Electrolyte Phase Optimization Results

The electrolyte phase optimal nodes selected are as shown in Figure 39, the selected nodes are closely packed in the negative electrode due to its importance in the overall concentration dynamic predictions. The same sets of nodes were selected in the separator and positive electrode for all the number of cases considered. It can be observed from Table 8 that as the number of variables increase, the reduction in the prediction error are insignificant compared to the prediction improvement achieved under CC and pulse operations.
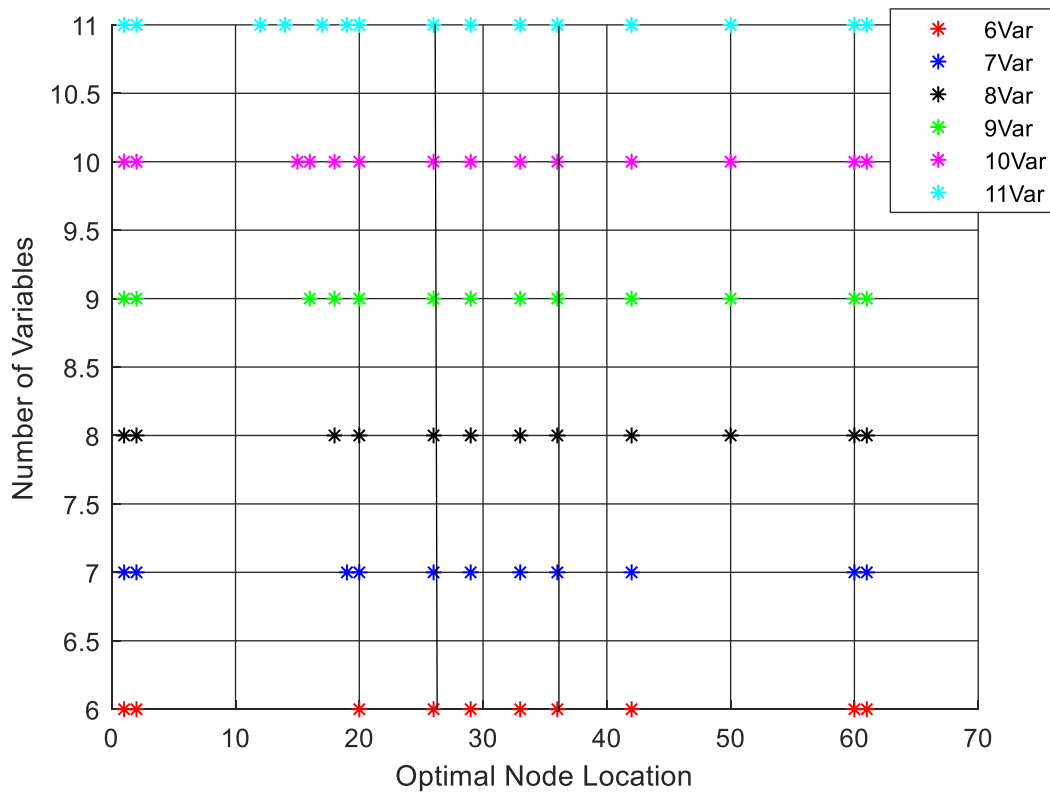
Figure 39: Optimal Solid-phase Discretization Nodes for HPPC Operation

Table 8: Solid and Electrolyte-Phase Concentration Prediction Error for HPPC Operation

Number of Variables	Objective Function J_1 only	Objective Function $\alpha_1 J_1 + \alpha_2 J_2$	Number of Variables	Electrolyte phase Objective function
4	265.54	2071.7	6	132.02
5	240.04	1772.4	7	132.00
6	230.67	1585.9	8	125.06
7	228.75	1537.2	9	122.06
8	225.50	1426.6	10	118.65
9	223.23	1354.1	11	118.65

5.3.3 Voltage and Concentration Simulation Results

Tables 9 and 10 shows the errors between voltage predictions of the reference model and the proposed model. Table 9 present the prediction errors for the proposed model based on objective function with only J_1, the maximum rms and absolute error reduced from 3.3mV and 20.0mV for 4 variables model to 0.79mV and 5.2mV for 9 variables model respectively. Likewise, the other model with a J_1 and J_2 solid phase objective function has the same predictions as the first model results, with little or no improvement in the prediction capacity with the inclusion of bulk concentration error minimization. Hence, for the proposed model there is no justification for including bulk concentration in the voltage computation for this operation. HPPC operation result also demonstrate that for solid and electrolyte phase concentration prediction, 7 and 9 unevenly discretized nodes are enough to accurately predict their respective concentration dynamics above which there is no model prediction improvement but higher computational cost which are in concordant with the two previous operations results.

Figure 40 and 41 shows the voltage profile of the proposed model with different number of optimal solid-phase nodes with respect to the reference model predictions.
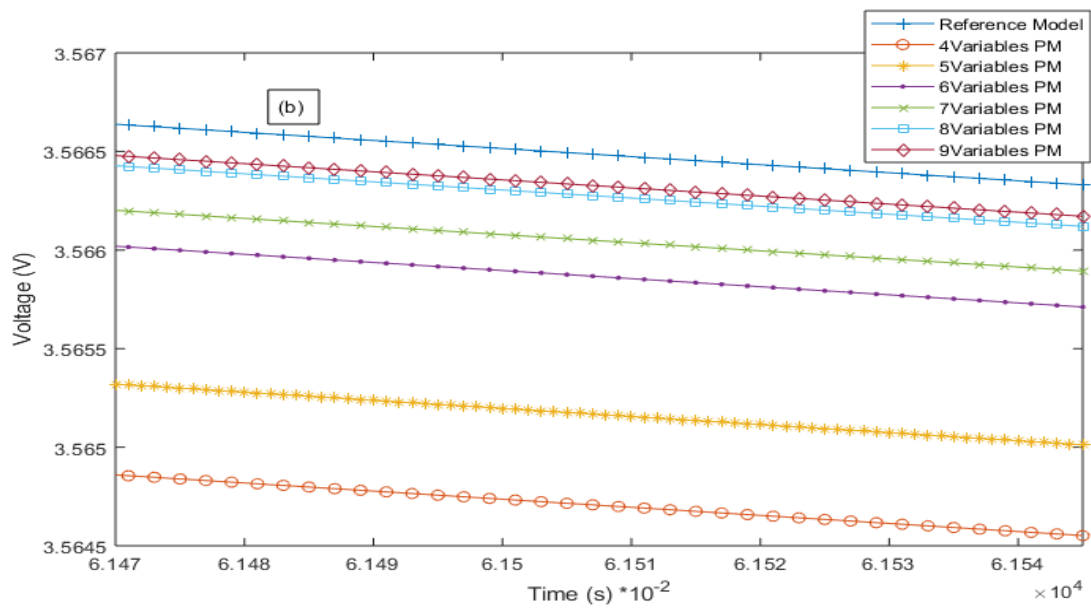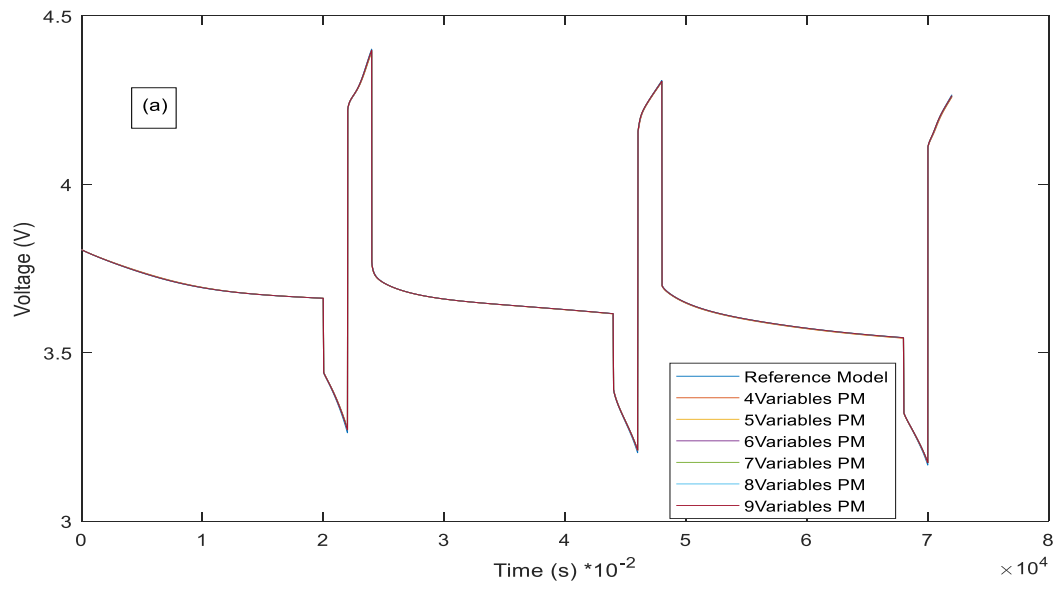
Figure 40: (a)Voltage prediction of the proposed model for different number of discretization steps in solid phase for J_1 (b) Magnified voltage prediction results (c) Voltage prediction error for each nuber of variaboles model for Pulse Operation

Table 9: Voltage Prediction Error Based on J_1 Alone for HPPC Operation

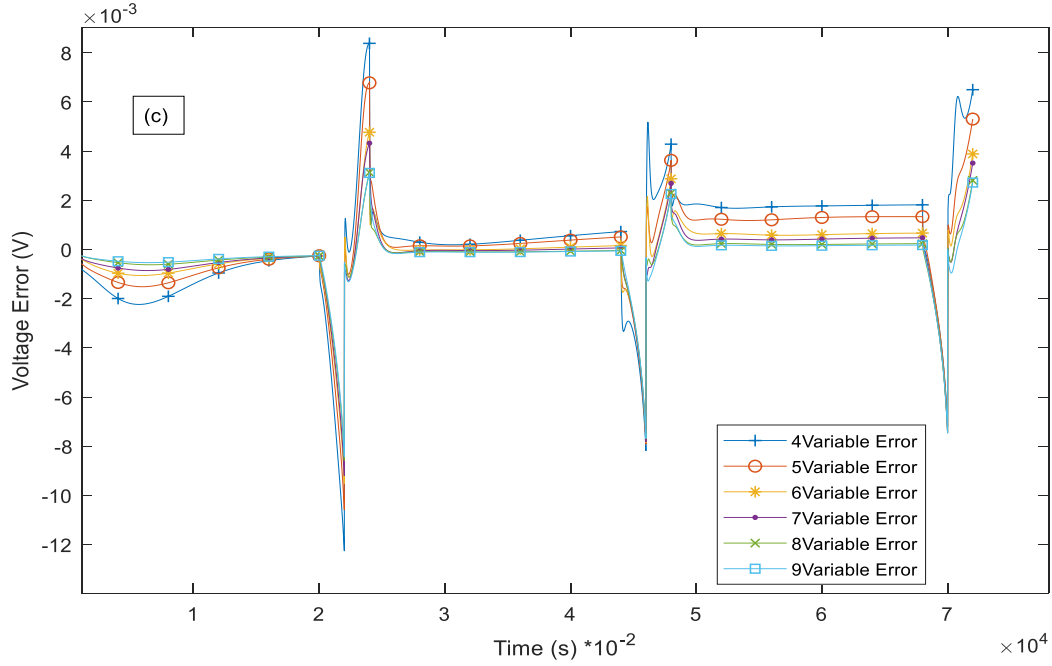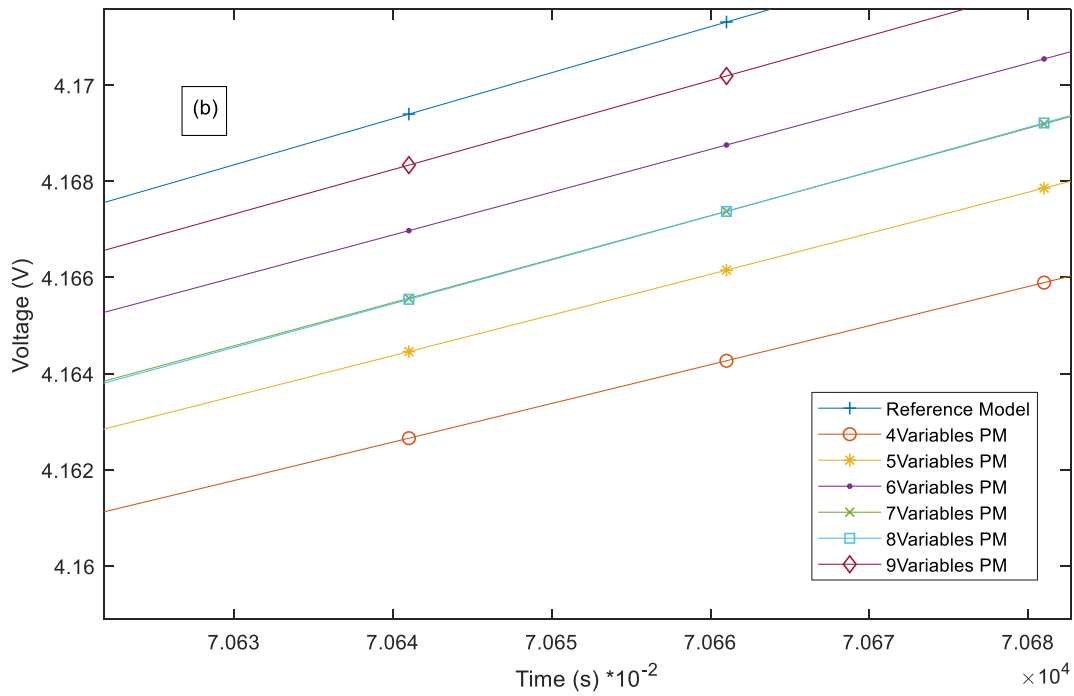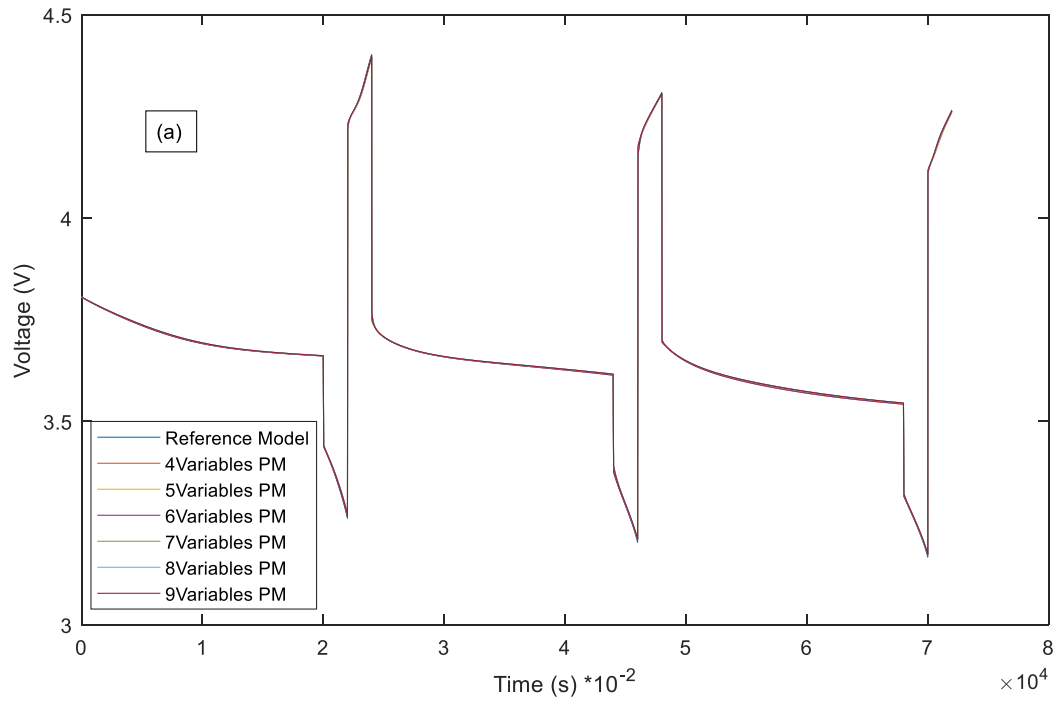| Solid phase Nodes (J_1)	4		5		6		7		8		9	
Electrolyte phase Nodes	Rms (mV)	Max (mV)	Rms (mV)	Max (mV)	Rms (mV)	Max (mV)	Rms (mV)	Max (mV)	Rms (mV)	Max (mV)	Rms (mV)	Max (mV)
6	3.3	20.0	2.8	18.5	2.5	17.5	2.5	17.5	2.4	16.5	2.3	16.4
7	3.0	18.6	2.5	16.9	2.3	15.9	2.2	15.9	2.1	14.9	2.1	14.8
8	2.4	13.4	1.9	11.7	1.6	10.6	1.5	10.6	1.3	9.7	1.3	9.6
9	2.2	11.3	1.7	9.7	1.3	8.6	1.3	8.6	1.1	7.6	1.1	7.5
10	2.1	9.9	1.5	8.3	1.1	7.2	1.1	7.2	0.90	6.2	0.89	6.1
11	2.0	9.1	1.5	7.4	1.0	6.3	1.1	6.3	0.80	5.4	0.79	5.2
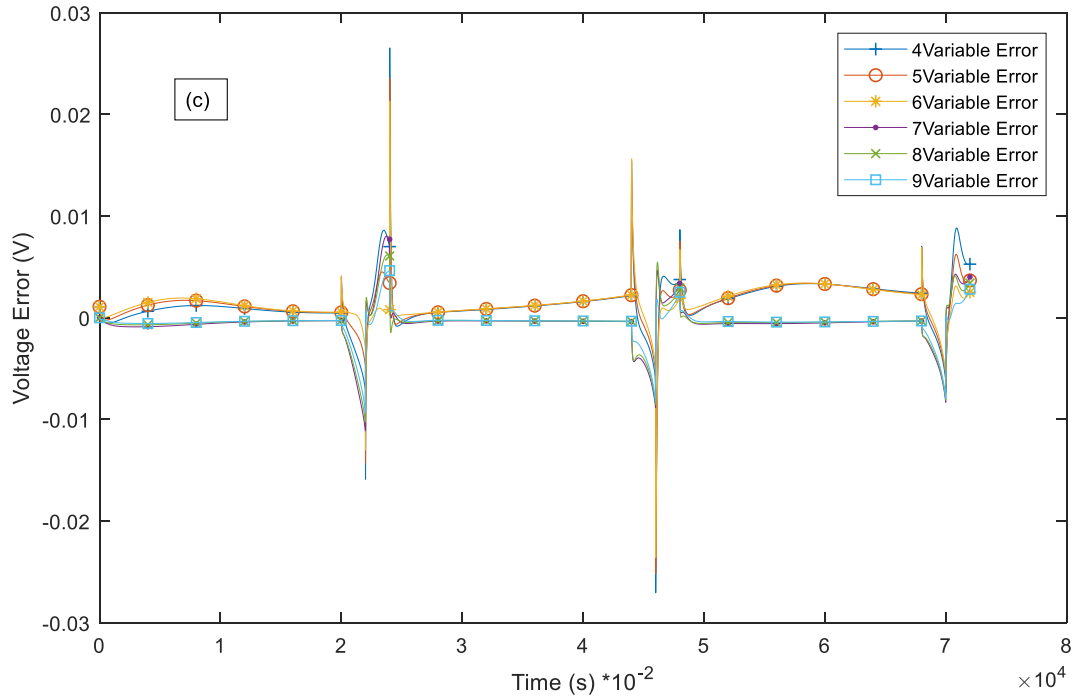
Figure 41: (a)Voltage prediction of the proposed model for different number of discretization steps in solid phase for J_1 and J_2 (b) Magnified voltage prediction results (c) Voltage prediction error for each number of variaboles model for HPPC Operation

Table 10: Voltage Prediction Error Based on J_1 and J_2 Alone for HPPC Operation

Solid phase Nodes ($J_1 J_2$)	4		5		6		7		8		9	
Electrolyte phase Nodes	Rms (mV)	Max (mV)	Rms (mV)	Max (mV)	Rms (mV)	Max (mV)	Rms (mV)	Max (mV)	Rms (mV)	Max (mV)	Rms (mV)	Max (mV)
6	3.3	20.2	2.8	18.5	2.5	17.5	2.5	17.5	2.4	16.5	2.3	16.4
7	3.0	18.6	2.5	16.9	2.3	15.8	2.2	15.9	2.1	14.9	2.1	14.8
8	2.4	13.4	1.9	11.7	1.6	10.6	1.5	10.7	1.3	9.7	1.3	9.6
9	2.2	11.3	1.7	9.7	1.3	8.6	1.3	8.6	1.1	7.6	1.1	7.5
10	2.1	10.6	1.6	8.9	1.2	7.8	0.97	6.9	0.97	6.9	0.95	6.7
11	2.0	8.6	1.4	6.9	1.0	5.8	1.0	5.9	0.75	4.9	0.74	4.7

5.4 Nodal Point Sensitivity Analysis

The sensitivity of the prediction capability of the proposed model was investigated under this section to investigate the impact of applying the constant current optimal nodes to pulse and hybrid operations model and vice versa. Table 11 shows the surface concentration prediction errors (J_1) of the proposed model with respect to reference model when CC optimal nodal results are applied

to the other two models. The prediction results for the proposed model under pulse charge/discharge operation based on the application of CC optimal nodes shows 20times error magnitude with respect to CC operation prediction error, and 5times error magnitude under HPPC operation. Under HPPC operation, as the number of nodes increases, the magnitude of error between this operation and that of CC operation reduces. From 7 optimal nodes upward the two-model prediction capability based on CC optimal nodal solution became close.

Table 11: Solid-phase Concentration Prediction Error Based on CC Optimal Result Applied to other Current Profile Models

Number of Variables	CC Optimal Solution		
	CC	Pulse	HPPC
4	21.97	385.79	83.32
5	27.32	349.25	57.72
6	26.05	285.87	36.69
7	18.57	233.07	29.12
8	13.70	187.28	18.94
9	10.54	149.87	15.46

Table 12 shows the result based on the application of pulse operation optimal nodes to the proposed model with CC and HPPC operations. The prediction results in the table shows that the discrepancies between the pulse prediction errors is approximately halve of HPPC prediction errors whereas the is a huge difference between the prediction error results of pulse operation in comparison to that of CC operation. Hence, the proposed model with pulse charge/discharge is highly sensitive to CC optimal solution and vice versa.

Table 12: Solid-phase Concentration Prediction Error Based on Pulse Optimal Result Applied to other Current Profile Models

Number of Variables	Pulse Optimal Solution		
	CC	Pulse	HPPC
4	116	18.93	45.69
5	115.93	11.03	22.70
6	45.09	7.29	17.89
7	44.52	5.48	11.20
8	22.38	3.74	9.00
9	18.74	3.40	6.02

The sensitivity of the proposed model using HPPC optimal nodal solutions, with the other two current operation as shown in Table 13 demonstrate that applying HPPC optimal nodal solution to the other model operations does not have any significant effect on the prediction capability of the proposed model.

Table 13: Solid-phase Concentration Prediction Error Based on HPPC Optimal Result Applied to other Current Profile Models

Number of Variables	HPPC Optimal Solution		
	CC	Pulse	HPPC
4	241.82	268.34	265.54
5	242.00	254.28	240.04
6	249.51	239.42	230.67
7	243.02	229.54	228.75
8	233.47	222.54	225.50
9	226.70	220.00	223.23

Conclusively, an HPPC operation-based model can be designed to use an optimal nodal solution of either constant current or pulse operation without any significant trade off with the model

accuracy making HPPC operation less sensitive to the other two operation optimal solutions. Likewise, for higher number of nodes, the optimal nodal solutions of both CC and pulse operations can be apply for HPPC operation prediction purpose without much reduction in model accuracy. In contrast, CC and pulse operations have high sensitivity towards each other solutions, hence neither can CC optimal nodal solutions be applied for pulse operation predictions without reduction in the model accuracy nor can pulse optimal nodal solution be applied for CC operation predictions. The proposed model with CC and pulse operations are sensitive to the optimal nodal solution applied, and for HPPC operation the proposed model is less sensitive to optimal nodal solution applied.

Chapter 6: Conclusion and Future Work

6.1 Conclusion

The objective of this work was to develop an optimal model reduction of LIB systems for control and system design purpose. The LIB systems partial differential equations which governs the battery operations and performance, were obtained from the conservation laws for both species and charge, coupled with the electrochemical kinetic Butler-Volmer's equation. These PDEs were converted into ordinary differential equations (ODE) through finite difference method and solved numerically. The objective of this work was met by using particle swarm optimization to determine the optimal uneven discretization nodes, necessary for accurately prediction of solid and electrolyte phase concentrations. Evenly discretized nodes model was used as a reference model in the development of the proposed reduced order model.

A minimization problem was formulated based on the surface and bulk concentrations errors at the solid-phase level, and at the two sides of the electrodes for electrolyte-phase concentration errors between the reference model and the proposed model. The PSO algorithm was employed to determining the global minimizer for the optimization problem. The solutions converged mostly after 500 iteration counts for the two phases.

Three current profiles were applied to the proposed model, and their simulation results were presented. The presented results demonstrate that, the proposed model can predict the electrochemical behavior of lithium-ion batteries for a wide range of applied current conditions. MATLAB

computer code was written for referenced model and the proposed model, the proposed model was validated by computing the rms and absolute maximum error with respect to the reference model.

The proposed model simulation results demonstrate a close prediction to that of the reference model. Based on the voltage rms error computed between the two models for the three current profiles analyzed, it was observed that inclusion of bulk concentration in the solid-phase objective formulation does not improve the accuracy of the proposed model, specifically under pulse and HPPC operations. Since the proposed model is developed mainly for battery terminal voltage prediction, then surface concentration error minimization will suffice for solid-phase objective formulation to ensure high concentration and voltage prediction accuracy.

The accuracy of the proposed model increases as the order of the model increase for both solid and electrolyte phase concentration predictions, until a saturation point of 7 variables for solid phase concentration predictions and 9 variables for electrolyte-phase predictions was reached. Above these saturation points there was no significant improvement in the accuracy of the proposed model. The proposed reduced order model was able to achieve a good prediction accuracy with respect to the reference model with 7 and 9 unevenly discretized steps for solid and electrolyte phase concentration prediction respectively.

The full order model has 100 nodes for solid phase discretization, and 60 nodes for electrolyte phase discretization, and these have been successfully reduced by the proposed model reduction scheme to 14 nodes for solid phase uneven discretization, and 9 nodes for electrolyte phase uneven discretization. Hence the proposed optimal model reduction scheme, reduced the order of the full model by 7 times, without loss of physical interpretation of the diffusion and migration dynamics in the solid particles and electrolyte across the entire cell. This reduction in the number of discretization will allows faster computation for the purpose of control and systems design.

The proposed model was simulated with a constant current operation based on the optimal number of nodes. The model prediction has a rms voltage error of 0.9mV, and a maximum absolute voltage error of 1mV. The pulse operation prediction has a rms voltage error of 0.4mV, and a maximum absolute voltage error of 4mV. The HPPC operation prediction has a rms voltage error of 1mV, and a maximum absolute voltage error of 9mV. Thus, the computational effort required to model and simulate the full order model have been reduced 7 seven times by the proposed optimal model reduction scheme. The proposed model embodies high precision, and fast simulation of battery performance for a range of working conditions.

In the future, further investigation on the impact of bulk concentration inclusion in the solid phase objective function formulation, on the accuracy of the proposed reduced order model in estimating the battery state of charge (SoC) will be carried out. In developing the proposed model reduction scheme, a constant electrolyte diffusivity coefficient was assumed for simplification purpose. The implementation of concentration dependent electrolyte diffusivity coefficient will be included in the proposed model in the future. Furthermore, the optimal model reduction scheme methodology will be applied in developing a reduced order model for solid state battery modeling and state estimations.

References

1. Whittingham, M. S., "History, Evolution, and Future Status of Energy Storage," 2012.

2. [Online]. Available: http://batteryuniversity.com/learn/article/battery_developments. [March 2019].

3. Bergveld, H. J., "Battery Management Systems Design by Modeling" Published 2001.

4. [Online] Article "Batteries – Types & working" Available: https://www.elprocus.com/batteries-types-working [February 2019].

5. [Online] Available: http://global.kawasaki.com/en/energy/solutions/battery_energy/questions/index.html [February 2019]

6. Linden, D. and Reddy, T. B., "Portable Sealed Nickel-Metal Hydride Batteries," in Handbook of Batteries, McGraw-Hill, 2001.

7. Domenico, D.D., Stefanopoulou, A., Fiengo, G., (2010), "Lithium-Ion Battery State of Charge and Critical Surface Charge Estimation Using an Electrochemical Model-Based Extended Kalman Filter". ASME 2010, 132 / 061302-1.

8. Doyle, M., Fuller, T. F., and Newman, J., (1993), "Modeling of Galvanostatic Charge and Discharge of the Lithium/Polymer/Insertion Cell," J. Electrochem. Soc., 140, pp. 1526–1533.

9. De Vidts, P., Delgado, J., and White, R. E., (1995), "Mathematical Modeling for the Discharge of a Metal Hydride Electrode," J. Electrochem. Soc., 142, pp. 4006–4013.

10. Smith, K., and Wang, C. Y., (2006), "Solid-State Diffusion Limitations on Pulse Operation of a Lithium-Ion Cell for Hybrid Electric Vehicles," J. Power Sources, 161, pp. 628–639.

11. Lee, T.K., Kim, Y., Stefanopoulou, A., and Filipi, Z., (2011), "Hybrid electric vehicle supervisory control design reflecting estimated lithium-ion battery electrochemical dynamics", ACC 2011, in print.

12. Sciarretta, A., Back, M., and Guzzella. L., (2004), "Optimal Control of Parallel Hybrid Electric Vehicles", IEEE Trans. Control Systems Technology, vol. 12, no. 3 pp. 352-363.

13. Sharer, P., Rousseau, A., Pagerit, S., and Nelson, P., (2007), "Midsize and SUV vehicle results for plug-in HEV component requirements", SAE Technical Paper 2007-01- 0295.

14. Patil, R., Adornato, B., and Filipi, Z., (2010), "Design Optimization of a Series Plug-in Hybrid Electric Vehicle for Real-World Driving Conditions", SAE Paper 2010-01-0840.

15. Patil, R., Adornato, B., and Filipi, Z., (2009), "Impact of Naturalistic Driving Patterns on PHEV Performance and System Design", SAE Paper 2009-01-2715.

16. Xiaa, L., Najafia, E., Lib, Z., Bergvelda, H.J., and Donkers, M.C.F., (2017). "A computationally efficient implementation of a full and reduced-order electrochemistry-based model for Li-ion batteries" Applied Energy 208:(2017):1285-1296.

17. Li, J., Lotfi, N., Landers, R. G., and Park, J., (2017) "A Single Particle Model for Lithium-Ion Batteries with Electrolyte and Stress-Enhanced Diffusion Physics" J Electrochemical Soc 164 (4) A874-A883.

18. Luo, W., Lyu, C., Wang, L., and Zhang, L., (2013). "An approximate solution for electrolyte concentration distribution in physics-based lithium-ion cell models". Microelectronics Reliability, 53, 797.

19. Rahimian, S. K., Rayman, S., and White, R. E., (2013). "Extension of Physics-Based single Particle Model for Higher Charge-Discharge Rates" Journal of Power Sources, 224, 180.

20. Baba, N., Yoshida, H., Nagaoka, M., Okuda, C., and Kawauchi, S., (2014). "Numerical simulation of thermal behavior of lithium-ion secondary batteries using the enhanced single particle model". Journal of Power Sources, 252, 214 (2014).

21. Smith, K.A., Rahn, C.D., Wang, C.Y., (2007). "Control oriented 1D electrochemical model of Lithium-ion battery". Energy Convers Manage 2007;48(9):2565–78.

22. Lee, T.K. and Filipi, Z.S., (2011). "Electrochemical Li-Ion Battery Modeling for Control Design with Optimal Uneven Discretization" ASME 2011 DSCC, in print.

23. Han, X., Ouyang, M., Lu, L., and Li, J., (2015). "Simplification of physics-based electrochemical model for lithium ion battery on electric vehicle. Part I: Diffusion simplification and single particle model," Journal of Power Sources, vol. 278, pp. 802 – 813, 2015.

24. Subramanian, V.R., Boovaragavan, V., Ramadesigan, V., Arabandi, M., (2009). "Mathematical model reformulation for lithium-ion battery simulations: galvanostatic boundary conditions". J Electrochem Soc 2009;156: A260–71.

25. Lia, J., Adewuyia, K., Lotfib, N., Landersa, R.G., Park, J., (2018). "A single particle model with chemical/mechanical degradation physics for lithium ion battery State of Health (SOH) estimation" Applied Energy 212:(2018):1178-1190.

26. Luo, W., Lyu, C., Wang, L.,0 Zhang, L., (2013). "A new extension of physics-based single particle model for higher Charge/discharge rates" J. Power Sources, 241, pp. 295–310.

27. Gu, W. B., Wang, C.Y., Weidner, J.W., Jungst, R.G., and Nagasubramanian, G., "Computational Fluid Dynamics Modeling of a Lithium/Thionyl Chloride Battery with Electrolyte Flow," Journal of The Electrochemical Society, vol. 147, 2000.

28. Ye, Y., Shi, Y., Cai, N., Lee, J., and He, X., (2012). "Electro-thermal modeling and experimental validation for lithium ion battery," Journal of Power Sources, vol. 199.

29. Perez, H., Shahmohammadhamedani, N., and Moura, S., (2015.) "Enhanced performance of li-ion batteries via modified reference governors and electrochemical models," IEEE/ASME Transactions on Mechatronics, vol. 20, no. 4, pp. 1511–1520.

30. Moura, S., (2016). "Single Particle Model with Electrolyte and Temperature: An electrochemical battery model". Available online: https://github.com/scott-moura/SPMeT.

31. Stetzel, K.D., Aldrich, L.L., Trimboli, M.S., Plett, G.L., (2015). "Electrochemical state and internal variables estimation using a reduced-order physics-based model of a lithium-ion cell and an extended Kalman filter" J. Power Sources, 278, pp. 490–505.

32. Perez, H. E., Dey, S., Hub, X., Moura, S., (2017). "Optimal Charging of Li-Ion Batteries via a Single Particle Model with Electrolyte and Thermal Dynamics" Journal of The Electrochemical Society, 164, A1679-A1687.

33. Tanim, T.R., Rahn, C.D., Wang, C., (2014). "A reduced order electrolyte enhanced single particle lithium ion cell model for hybrid vehicle applications" IEEE International Conference on, vol. 4, 2014, pp. 141–146.

34. Prada, E., Domenico, D.D., Creff, Y., Bernard, J., Sauvant-Moynot, V., Huet, F., (2013). "A Simplified Electrochemical and Thermal Aging Model of $LiFePO_4$-Graphite Li-ion Batteries: Power and Capacity Fade Simulations" Journal of The Electrochemical Society, 160, A616-A628.

35. Linden, D., and Reddy, T. B. (2001)."Portable Sealed Nickel-Metal Hydride Batteries," in Handbook of Batteries, McGraw-Hill.

36. Grossmann, C., Roos, H.G., Stynes, M., (2007). "Numerical Treatment of Partial Differential Equations. Springer Science & Business Media". p. 23. ISBN 978-3-540-71584-9.

37. Craft, T.J., "Finite Difference Schemes". School of Mechanical Aerospace and Civil Engineering, TPFE MSc CFD-1.

38. Dunn, B., Kamath, H., Tarascon, J.M., (2011). "Electrical energy storage for the grid: a battery of choices Science". 334 (6058) (2011) 928e935.

39. Kennedy, J., and Eberhart, R., (1995). "Particle swarm optimization, in Neural Networks". IEEE International Conference on, vol. 4, nov/dec 1995, pp. 1942–1948.

40. Hu X., "PSO Tutorial" available online, extracted January 2019 from, http://www.swarmintelligence.org/tutorials.php

41. Ebbesen S., Kiwitz P., Guzzella L. "A generic particle swarm optimization MATLAB function" American Control Conference, ACC.2012.6314697.

42. Duro J., and De-Oliveira, J., (2008). "Particle swarm optimization applied to the chess game," in Evolutionary Computation". CEC 2008. (IEEE World Congress on Computational Intelligence). IEEE Congress on, June 2008, pp. 3702 –3709.

43. Faria, P., Vale, Z., Soares, J., and Ferreira, J., (2011) "Particle swarm optimization applied to integrated demand response resources scheduling, in Computational Intelligence Applications in Smart Grid (CIASG)". 2011 IEEE Symposium on, April 2011, pp. 1 –8.

44. Lambert-Torres, G., Martins, H., Coutinho, M., Salomon, C., and Vieira, F., (2009) "Particle swarm optimization applied to system restoration," in Power Tech, 2009 IEEE Bucharest, 2009, pp. 1–6.

45. Hassan, R., Cohanim, B., Weck, O.D., Venter, G. "A Comparison of Particle Swarm Optimization and the Genetic Algorithm, An Introduction to Particle Swarm Optimization". Published 2004.

46. Blondin, J., "Particle Swarm Optimization: A Tutorial (2009)" extracted online January 2019.

47. [Online] Available: http://global.kawasaki.com/en/energy/solutions/battery_energy/questions/index.html [February 2019]

48. Borakhadikar, A.S. "One Dimensional Computer Modeling of a Lithium-Ion Battery". Master's Degree Thesis submitted to Wright state University, 2017.

49. Shamsi, M. H., "Analysis of an electric Equivalent Circuit Model of a Li-ion battery to develop algorithms for battery states estimation," 2016.

50. [Online]. Available: http://batteryuniversity.com/learn/article/battery_developments. [Accessed March 2019].

51. Joel, C. Forman, J.C., Bashash, S., Stein, J.L., Fathy, H.K. "Reduction of an Electrochemistry-Based Li-Ion Battery Model via Quasi-Linearization and Padé Approximation". Journal of The Electrochemical Society, 158, A93-A101 (2011)